

REPORT DOCUMENTATION PAGE

Public reporting burden for this collection of information is estimated to average 1 hour per response, including the time for reviewing data needed, and completing and reviewing this collection of information. Send comments regarding this burden estimate or any other aspect of this burden to Department of Defense, Washington Headquarters Services, Directorate for Information Operations and Reports (4302). Respondents should be aware that notwithstanding any other provision of law, no person shall be subject to any penalty for failing to comply with a collection of information if it does not have a valid OMB control number. PLEASE DO NOT RETURN YOUR FORM TO THE ABOVE ADDRESS.

AFRL-SR-BL-TR-01-

maintaining the
or reducing
22200-
a currently

0170

1. REPORT DATE (DD-MM-YYYY) 01-09-2000		2. REPORT TYPE Final Report		3. DATES COVERED (From - To) 10-01-1997 31-09-2000	
4. TITLE AND SUBTITLE Experimental Investigation of High-Speed Boundary Layers With Wall Roughness				5a. CONTRACT NUMBER F49620-98-1-0038	
				5b. GRANT NUMBER	
				5c. PROGRAM ELEMENT NUMBER	
6. AUTHOR(S) Rodney D. W. Bowersox, Dr.				5d. PROJECT NUMBER	
				5e. TASK NUMBER	
				5f. WORK UNIT NUMBER	
7. PERFORMING ORGANIZATION NAME(S) AND ADDRESS(ES) The University of Alabama Aerospace Engr. & Mechanics Box 870280 Tuscaloosa, AL 35487				8. PERFORMING ORGANIZATION REPORT NUMBER UA-AEM-APL-2001-001	
9. SPONSORING / MONITORING AGENCY NAME(S) AND ADDRESS(ES) AFOSR/NA 801 N. Randolph St., Rm. 732 Arlington, VA 22203-1977				10. SPONSOR/MONITOR'S ACRONYM(S)	
				11. SPONSOR/MONITOR'S REPORT NUMBER(S)	
12. DISTRIBUTION / AVAILABILITY STATEMENT Approved for Public Release; Distribution Unlimited					
13. SUPPLEMENTARY NOTES					
14. ABSTRACT A comprehensive investigation of the influence of surface roughness on the mean and turbulent flow properties of a high-speed turbulent boundary layer flow was performed. Six wall topologies, including a smooth and five rough surfaces consisting of three random sand-grain plates and two uniformly machined plates ($k = 0 - 1.7$ mm), were tested at three high Reynolds number ($Re/m = 2 \times 10^7$) Mach numbers (0.22, 0.65 and 2.75). Mean flow measurements included surveys of the velocity and density. Turbulence quantities included measurements of the kinematic velocity turbulence intensities, mass flux turbulence intensities, kinematic Reynolds shear stress, compressible Reynolds shear stress, density-transverse-velocity fluctuation correlation, velocity spectra, auto-correlations, micro- and integral-scales and turbulent structure angles. Numerical simulations included evaluating three algebraic turbulence models with a boundary layer program. A three-year program was performed.					
15. SUBJECT TERMS Turbulence, Rough Walls, Boundary Layers, Supersonic, Compressible, Incompressible					
16. SECURITY CLASSIFICATION OF:			17. LIMITATION OF ABSTRACT	18. NUMBER OF PAGES	19a. NAME OF RESPONSIBLE PERSON Rodney Bowersox
a. REPORT Unclassified	b. ABSTRACT Unclassified	c. THIS PAGE Unclassified			19b. TELEPHONE NUMBER (include area code) (205) 348-1905

AIR FORCE OFFICE OF SCIENTIFIC RESEARCH (AFOSR)
NOTICE OF TRANSMITTAL DTIC. THIS TECHNICAL REPORT
HAS BEEN REVIEWED AND IS APPROVED FOR PUBLIC RELEASE
LAW AFR 100-12. DISTRIBUTION IS UNLIMITED.

EXPERIMENTAL INVESTIGATION OF HIGH-SPEED BOUNDARY LAYERS WITH WALL ROUGHNESS

FINAL REPORT

Principal Investigator:

Dr. Rodney D. W. Bowersox
The University of Alabama, Tuscaloosa, AL

Graduate Research Assistants

Maj. Robert M. Latin, PhD
U.S. Air Force Office of Scientific Research, Arlington VA

Mr. V. Gene Pritchett, (MS)
NASA Marshall Space Flight Center, Huntsville AL

Mr. Huaiguo Fan (MS)
The University of Alabama, Tuscaloosa AL

Approved for Public Release; Distribution Unlimited

20010320 071

Executive Summary

This document summarizes the research project funded under F49620-98-1-0038. The principal objective of this research program was to experimentally investigate the combined influence of compressibility and surface roughness on the mean and turbulent flow characteristics of high-speed high Reynolds number turbulent boundary layer flow to further understanding and predictability.

A comprehensive experimental program that used both traditional and laser diagnostic techniques was performed. To provide information that will be useful to a broad range of applications and to quantify compressibility effects, three high Reynolds number flow conditions was tested: incompressible ($M = 0.22$), compressible subsonic ($M = 0.65$), and supersonic ($M = 2.8$). To better isolate compressibility effects, for each flow condition, the Reynolds number was nominally matched ($Re/m = 20-25 \times 10^6$) and the same six flow models (described in the next paragraph) were tested.

Five rough wall models and a smooth wall case, for comparison purposes, were tested to examine roughness height and blockage effects. The roughened wall models consisted of three random sand-grain and two uniformly distributed roughness topologies. The 2-D distributed roughness model had rectangular elements ($0.56 \times 0.56\text{-mm}^2$) that spanned the width of the test section with a wavelength of 2.18-mm. The 3-D distributed plate had cubic pillars ($0.56 \times 0.56 \times 0.56\text{-mm}^3$) also with a wavelength of 2.18-mm. The surface topology of each model was accurately (to within 4.0%) documented with a confocal laser scan microscope.

The experimental techniques employed to provide a complete flow field characterization included laser Doppler velocimetry, multiple overheat cross/hot-film anemometry, particle image velocimetry, conventional Pitot pressure, floating element skin friction gages and color schlieren photography. Mean flow measurements included surveys of the velocity and density. Turbulence quantities included measurements of the kinematic velocity turbulence intensities, mass flux

turbulence intensities, kinematic Reynolds shear stress, compressible Reynolds shear stress, density-transverse-velocity fluctuation correlation, velocity spectra, auto-correlations, micro- and integral-scales and turbulent structure angles.

Along with the detailed experimental studies, a companion numerical investigation was performed primarily to quantify the strengths and weaknesses of current turbulence models. In-house boundary layer and parabolized Navier-Stokes solvers with a variety of popular algebraic models were used. These models were compared to the experimental data acquired in this study.

This ambitious project was very successful. The majority of the research (90%) was completed on time, and work is currently underway to complete the last outstanding item (turbulence measurements at $M = 0.65$). Very detailed descriptions of the flow fields were acquired including direct measurements of the density-velocity fluctuation correlation across the boundary layers, which before this project were unavailable. These new data have provided improved flow field understanding and a basis for model development. Detailed numerical simulations have been performed with simple turbulence models, and a new algorithm for estimating the wall friction was employed that improved the accuracy of the predictions.

A recommendation beyond the scope of this work is to extend the test matrix to include wall curvature effects. This effort should be directed at providing flow field insight suitable for second order turbulent transport modeling. This recommendation is based on (1) the numerous practical Air Force applications (e.g., thermal protection for access to space, turbomachinery, inlets and nozzles, and scramjet combustors), (2) the PI's experience with wall curvature and the associated complicated impact on the turbulent shear stress distributions, (3) the inability of current algebraic and two-equation models to provide accurate predictions for this class of flows, and (4) large-eddy simulation of wall bounded flows is more prohibitive than originally believed.

List of Symbols

A_B	= Roughness Frontal Blockage Area
C	= Constant in the logarithmic law of wall region
C_f	= Skin friction coefficient
c_p	= Specific heat at constant pressure
D	= Constant in the rough-wall logarithmic law
f	= Frequency
k	= Roughness height
k_s	= Equivalent sand grain roughness height
k^+	= Roughness Reynolds number ($= \rho_w u^* k / \mu_w$)
k_s^+	= Roughness Reynolds number ($= \rho_w u^* k_s / \mu_w$)
k_l	= Wave number ($= 2\pi f / u$)
C_f	= Skin friction Coefficient
L	= Length scale
M	= Mach number
p	= Pressure
Pr	= Prandtl number
R^+	= Constant in van Driest model
Re	= Reynolds number ($= \rho_e u_e L / \mu_e$)
T	= Temperature
t	= Time
u, U	= Mean Favre axial velocity
u, v, w	= Velocity components

u^* = Friction velocity

V = Voltage

w = Parallel-film sensor separation

x, y, z = Cartesian coordinates

y^+ = $\rho_w u^* y / \mu_w$

u^+ = u / u^*

Δ = $()_{rough} - ()_{smooth}$

Δx = Length from nozzle exit to the measurement location

Δx_o = Effective starting length due to finite thickness of the boundary layer at $x = 0$.

δ = Boundary-layer thickness ($u/u_e = 0.99$)

δ^* = Displacement thickness

δ^+ = $\rho_w u^* \delta / \mu_w$

δ_M = Boundary-layer thickness ($M/M_e = 0.99$)

κ = von Karman constant

θ = Momentum thickness, structure angle, ratio of grid size

λ = Roughness wavelength

ρ = Density

τ = Shear stress

μ = Dynamic viscosity

μ_t = Eddy viscosity

ν = Kinematic viscosity

$\Delta x, \Delta y$ = Grid size in the x and y directions

Δu = Velocity shift

Subscripts

e	= Boundary-layer edge condition
i,j	= Grid node in x and y direction, Einstein index
i	= leading edge of plate ($x = 0$)
k	= Kinematic
t	= Total condition
s	= Equivalent sand-grain roughness
w	= Wall
0	= Smooth Plate

Superscripts

T	= Turbulent
'	= Reynolds fluctuation
—	= Reynolds mean component
=	= Favre mean component
"	= Favre fluctuation

List of Tables

Table 1a	Supersonic Measurement Flow Conditions	74
Table 1b	Subsonic Measurement Flow Conditions	74
Table 2a	Supersonic Surface Conditions	75
Table 2b	$M = 0.22$ Surface Conditions	75
Table 2c	$M = 0.65$ Surface Conditions	75
Table 3	Measurement Uncertainty	76
Table 4a	Supersonic Reference Values ($x = 54$ cm)	77
Table 4b	Subsonic Reference Values	77
Table 5	Friction Velocity	78
Table 6	Summary of Numerical Roughness Data	79

List of Figures

Fig. 1	Effect of Roughness and Freestream Turbulence (7%) on mean heat transfer coefficients in a high pressure turbine stage, $Re = 1.2 \times 10^6$, and 0, 1, 4 and 9 correspond to smooth and distributed particle sizes of 54, 105, and 250 μm , respectively [Turner et al. (1985) as shown in Lakshminarayana (1996)].	80
Fig. 2	Wind Tunnel Facilities and Models (a) Schematic of Supersonic Wind Tunnel, (b) Photograph of Subsonic Wind Tunnel, (c) Machined Roughness Patterns, (d) Skin Friction Gage Concept, (e) Example Skin Friction Gage Calibration	81-82
Fig. 3	Color Schlieren Photograph (Supersonic Test Condition)	83-84
Fig. 4	Mean Flow Data Profile (Supersonic) (a) Mean Velocity Profiles (LDA and Pitot Data), (b) Effective Velocity Defect (Pitot Data), (c) Effective Law of the Wall Plot (Pitot Data), (d) Density (Modified Crocco and Combined LDA and Cross-Film)	85-88
Fig. 5	u- and v-Turbulence Intensity Profiles (a) Outer Variable Scaling, (b) Inner Variable Scaling, (c) Mixed Variable Scaling	89-91
Fig. 6	ρu -Turbulence Intensity Profiles (a) Outer Variable Scaling, (b) Inner Variable Scaling, (c) Mixed Variable Scaling	92-94
Fig. 7	ρv -Turbulence Intensity Profiles (Outer Variable Scaling)	95
Fig. 8	ρw -Turbulence Intensity Profiles (Outer Variable Scaling)	96
Fig. 9	Mass Flux Turbulence Intensities Versus k_s^+ (Outer Variable	97

Scaling)

- Fig. 10 Kinematic Turbulent Shear Stress Profiles (a) Outer Variable Scaling, (b) Inner Variable Scaling, (c) Mixed Variable Scaling 98-100
- Fig. 11 X-Y Component Compressible Reynolds Shear Stress (a) Outer Variable Scaling, (b) Inner Variable Scaling, (c) Mixed Variable Scaling 101-103
- Fig. 12 X-Z Component Compressible Reynolds Shear Stress (Outer Variable Scaling) 104
- Fig. 13 Peak Difference in the Compressible Reynolds Shear Stress (Outer Scaling) Versus k_s^+ 105
- Fig. 14 Second Order Density-Velocity Correlation Results (a) Outer Variable Scaling, (b) Inner Variable Scaling, (c) Mixed Variable Scaling 106-107
- Fig. 15 Dimensional Power Spectra (a) $y/\delta_M = 0.25$, (b) $y/\delta_M = 0.5$, (c) $y/\delta_M = 0.75$ 108-110
- Fig. 16 Power Spectra Difference versus Roughness Reynolds Number (a) $y/\delta_M = 0.25$, (b) $y/\delta_M = 0.5$, (c) $y/\delta_M = 0.75$ 111-113
- Fig. 17 Energy Spectra Results with Inner and Outer Scaling of the Frequency (a) Inner Scaling, (b) Outer Scaling, (c) Outer Scaling with the Strong Reynolds Analogy 114-116
- Fig. 18 Energy Spectra Results with Inner Scaling (a) $y/\delta_M = 0.25$, (b) $y/\delta_M = 0.5$, (c) $y/\delta_M = 0.75$ 117-119
- Fig. 19 Autocorrelation Functions (a) $y/\delta_M = 0.25$, (b) $y/\delta_M = 0.5$, (c) $y/\delta_M = 0.75$ 120-122

Fig. 20	Time-Scales (a) Micro-Scales, (b) Integral-Scales	123
Fig. 21	Parallel-Wire Cross-Correlation Traces (a) $y/\delta_M = 0.25$, (b) $y/\delta_M = 0.5$, (c) $y/\delta_M = 0.75$	124-126
Fig. 22	Structure Angle	127
Fig. 23	Velocity Profiles (a) $M = 0.65$ (Pitot Probe), (b) $M = 0.22$ (Hot-Wire)	128-129
Fig. 24	Example Skin Friction Gage Traces (20 Grit Plate, $M = 0.22$, 4 Runs)	130
Fig. 25	Defect Law Plots (a) $M = 0.22$, (b) $M = 0.65$	131-132
Fig. 26	Law of the Wall Plots (a) $M = 0.22$, (b) $M = 0.65$	133-134
Fig. 27	Turbulence Intensity Results ($M = 0.22$), (a) Outer Variable Scaling (Normal-Film Probe), (b) Outer Variable Scaling (Cross-Film Probe), (c) Inner Variable Scaling (Normal-Film Probe), (d) Inner Variable Scaling (Cross-Film Probe), (e) Mixed Variable Scaling (Normal-Film Probe), (f) Mixed Variable Scaling (Cross-Film Probe)	135-140
Fig. 28	Reynolds Shear Stress Profiles ($M = 0.22$, Cross-Film Probe) (a) Outer Variable Scaling, (b) Inner Variable Scaling, (c) Mixed Variable Scaling	141-143
Fig. 29	Representative Skin Friction Versus Local Reynolds Number Based on x-Location (a) Smooth Plate, (b) 80 Grit Plate, (c) 20 Grit Plate	144-145
Fig. 30	Representative Velocity Profiles with Comparison to Experimental Data (a) Smooth Plate, (b) 80 Grit Plate, (c) 20 Grit Plate	146-147

Fig. 31	Defect Law Plot with Comparison to Experimental Data	148
Fig. 32	Representative Law of the Wall Plots with Comparison to Experimental Data (a) Smooth Plate, (b) 80 Grit Plate, (c) 20 Grit Plate	149-150
Fig. 33	Representative Density Plots with Comparison to Experimental Data (a) Smooth Plate, (b) 80 Grit Plate, (c) 20 Grit Plate	151-152
Fig. 34	Representative Turbulence Shear Stress with Comparison to Experimental Data (a) Smooth Plate, (b) 80 Grit Plate, (c) 20 Grit Plate	153-154

Table of Contents

Executive Summary	ii
List of Symbols	iii
List of Tables	iv
List of Figures	vii
Table of Contents	viii
1. Introduction	1
1.1 Air Force Relevance and Technological Requirements	1
1.2 Research Objectives and Approach	3
1.3 Research Personnel	4
1.4 Research Publications	4
2. Background Review	6
3. Experimental and Numerical Methods	11
3.1 Wind Tunnels and Models	11
3.1.1 Supersonic Wind Tunnel	11
3.1.2 Subsonic Wind Tunnel	12
3.1.3 Wind Tunnel Models	13
3.2 Instrumentation and Data Reduction	14
3.2.1 Supersonic Experiments	14
3.2.2 Subsonic Experiments	20
3.3 Measurement Uncertainties	23
3.3.1 Supersonic Measurements	24

3.3.2 Subsonic Measurements	24
3.4 Numerical Methods	24
3.4.1 Model Formulations	24
3.4.2 Solution Accuracy and Stability	29
3.4.3 Initial and Boundary Conditions	30
4. Results and Discussion	32
4.1 Supersonic Experimental Results	32
4.1.1 Flow Visualization	32
4.1.2 Mean Flow Measurements	33
4.1.3 Turbulence Measurements	37
4.1.4 Spectral and Correlation Results	46
4.2 Subsonic Experimental Results	55
4.2.1 Mean Flow Measurements	55
4.2.2 Turbulence Measurements	57
4.3 Supersonic Numerical Results	58
5. Conclusions and Recommendations	62
5.1 Conclusions	62
5.1.1 Supersonic Experimental Study	63
5.1.2 Subsonic Experimental Study	65
5.1.3 Numerical Study	66
5.2 Recommendations	67
References	69
Tables	74
Figures	80

Chapter 1

Introduction

1.1 Air Force Relevance and Technology Requirement

The US Air Force (1995), in the *New World Vistas* document, identified viscous drag reduction and increased aircraft engine performance as key enabling technologies for the advancement of future war fighting technologies. Internal and external flowfields associated with modern weapons systems experience very complicated flowfields. The complications include compressibility, curved surfaces, high Reynolds numbers, elevated turbulence levels, surface roughness, and in some cases combustion. To quantify the importance of surface roughness on turbine engine performance, example mean turbine heat transfer data [Turner et al. (1985) as shown in Lakshminarayana (1996)], with varying roughness heights and freestream turbulence, are shown in Fig. 1.1. As indicated, roughness (and freestream turbulence) dramatically increased the heat transfer [Lakshminarayana (1996)]. Improved physical understanding and improved prediction methods for the rough-wall flow have direct relevance to two ongoing Air Force Research Laboratory programs: (1) the Integrated High Performance Turbine Engine Technology (IHPTET) program and (2) the Hypersonic Technologies (HyTech) program.

The increasing cost of ground testing and the increasing power of computing capabilities have coupled to drive designers and engineers to rely heavily on numerical

predictions in the design and optimization of aircraft engine and airframe components. Current numerical simulations of high Reynolds number flows are confined, because of computational limitations, to solutions of approximate averaged or filtered forms of the Navier-Stokes equations [Pope (1999)]. The power of modern computational hardware has resulted in routine large-eddy simulations of wall free turbulent flow. However, the demanding grid requirements and sensitive nature of the solutions to subgrid modeling are significant obstacles for large-eddy simulation of wall-bounded flows. Hence, simulations of wall bounded flows must rely on turbulence models in the classical Reynolds averaged approach. The development of accurate models depends heavily on empirical information for both flow field insight and model validation. The weaknesses in the current state of modeling was clearly stated by Hefner (1999):

"Much of the turbulence modeling research has focused on modeling the effect of turbulence on mean flows rather than modeling the turbulence physics; therefore, much of the turbulence modeling effort has focused on tweaking or adding constants and terms in the models to predict the available experimental data, which too often is mean flow data and not turbulence data. Although much has been said over the years regarding the need for definitive turbulence modeling experiments, there remains a paucity of high quality dynamic turbulence data useful for modeling and validation for flows about complex geometries."

Hence, an important technological challenge that has numerous Air Force aerospace propulsion and aerodynamic system applications is improved flow field understanding

and turbulence modeling of the effects of surface roughness on compressible turbulent boundary layer flow. Addressing this topic was the specific goal of this research program.

1.2 Research Objectives and Approach

The principal objective of this research program was to experimentally investigate the combined influence of compressibility and surface roughness on the mean and turbulent flow characteristics of high-speed high Reynolds number turbulent boundary layer flow to further understanding and predictability.

A comprehensive experimental program that uses both traditional and laser diagnostic techniques was performed. To provide information that will be useful to a broad range of applications and to quantify compressibility effects, three high Reynolds number flow conditions were tested: incompressible ($M = 0.22$), compressible subsonic ($M = 0.65$), and supersonic ($M = 2.8$). To better isolate compressibility effects, for each flow condition, the Reynolds number was nominally matched ($Re/m = 20\text{-}25 \times 10^6$) and the same six flow models (described in the next paragraph) were tested.

Five rough wall models and a smooth wall case, for comparison purposes, were tested to examine roughness height and blockage effects. The roughened wall models consisted of three random sand-grain and two uniformly distributed roughness topologies. The 2-D distributed roughness model had rectangular elements ($0.56 \times 0.56\text{-mm}^2$) that spanned the width of the test section with a wavelength of 2.18-mm. The 3-D distributed plate had cubic pillars ($0.56 \times 0.56 \times 0.56\text{-mm}^3$) also with a wavelength of 2.18-mm. The surface

topology of each model was accurately (to within 4.0%) documented with a confocal laser scan microscope.

Along with the detailed experimental studies, a companion numerical investigation was performed primarily to quantify the strengths and weaknesses of current turbulence models. In-house boundary layer and parabolized Navier-Stokes solvers with a variety of popular algebraic models were used. These models were compared to the experimental data acquired in this study.

1.3 Research Personnel

This PI for this project was Dr. R. Bowersox (Associate Professor, Aerospace Engineering and Mechanics, The University of Alabama). Graduate support was provided by Maj. R. Latin (PhD), Mr. H. Fan (MS, Best Thesis in both the College of Engineering and the Aerospace Engineering and Mechanics department) Mr. V. Pritchett (MS).

1.4 Research Publications

1. Latin, R. and Bowersox, R., "Flow Properties of a Supersonic Boundary Layer with Wall Roughness," *AIAA Journal*, Vol. 38, No. 10, 2000, pp. 1804-1821.
2. Latin, R. and Bowersox, R., "Influence of Surface Roughness on Supersonic Boundary Layer Turbulent Flow Structure," *14th International Symposium on Airbreathing Engines (XIV ISABE)*, Florence, Italy, Sept. 5-10, 1999. Also submitted to the *AIAA Journal* (Feb. 2001).

3. Pritchett, V. and Bowersox, "Flow Properties of Compressible and Incompressible Subsonic Turbulent Boundary Layers with Surface Roughness." 39th AIAA Aerospace Sciences Meeting, Reno NV, Jan 2001.
4. Fan, H. and Bowersox, "Numerical Analysis of High-Speed Flow over Rough Surfaces," AIAA-99-2381, 35th AIAA/ASME/SAE/ASEE Joint Propulsion Conference, Los Angeles CA, June 1999.

Chapter 2

Background Review

Boundary layers are responsible for skin friction drag and convection heat transfer over aircraft, missiles, re-entry vehicles, and propulsion systems. Surface roughness increases these engineering quantities and enhances transition from laminar to turbulent flow. Since all manufactured components of these systems have some inherent surface roughness or becomes rough through operation, it is important to quantify how surface roughness affects supersonic boundary layers in both a qualitative and quantitative manner to enable better understanding and prediction methods.

Direct numerical simulation of high Reynolds number turbulent flow is currently impractical. Hence, engineers and scientists must rely on an approximate averaged form of the governing Navier-Stokes equations. For Large-Eddy Simulation (LES) methods, a temporal filter is applied, and the large-scale structures are simulated, and the influences of the small-scale structure are modeled. For the Reynolds Averaged Navier-Stokes (RANS) approach, all of the turbulent temporal content is modeled. Due to the non-linearity of the Navier-Stokes equations, both filtering and averaging introduces additional second-order correlation unknowns into the problem. Modeling these

additional unknowns has proven to be a major challenge and a limiting factor in the accuracy of high-Reynolds number numerical simulations. Empirical information is a key element in understanding the essential dynamics, and has thus provided the basis for current turbulence models for both low- and high-speed flows.¹⁻³

For low-speed rough wall flow, the influence of surface roughness on the mean and turbulent flow properties is well documented,^{1,4-8} and the associated flow scaling¹ has provided the foundation for turbulence models suitable for low-speed zero pressure gradient rough wall flow.² From the experimental descriptions, surface roughness has been shown to have a direct influence on the inner region of the law of the wall and is typically described by a single parameter; namely the roughness Reynolds number k^+ . Nikuradse⁴ demonstrated that sand-grain generated roughness increased the velocity defect and skin friction and shifted the logarithmic region of the law of the wall downward. The amount of downward shift was shown to be a function of k^+ . Schlichting¹ introduced the concept of equivalent sand-grain roughness k_s^+ to correlate any surface roughness to the equivalent Nikuradse sand-grain roughness for comparison. Because the equivalent sand-grain roughness does not include roughness geometry or spacing, investigations of the influence of the roughness geometry have also been performed.⁵⁻⁶

Perry et al.⁷ provided a detailed investigation of the turbulent flow structure for smooth and rough wall flat plate boundary layers. The *turbulent wall region* was defined as $\nu/u^* \ll y \ll \delta$ for the smooth wall, and $k \ll y \ll \delta$ for the rough wall. The *fully turbulent region* was defined as $100\nu/u^* < y < \delta$ and $2k < y < \delta$. Power density spectra *inner variable scaling* was such that the power normalized by the friction velocity was

plotted versus the wave number normalized by multiplying by y [i.e., $u'(k_1 y)/u^{\star 2}$]. and *outer variable scaling* was defined such that the normalized power was plotted versus the wave number nondimensionalized by multiplying by δ [i.e., $u'(k_1 \delta)/u^{\star 2}$]. Perry et al. demonstrated that when plotted with inner variable scaling, the near wall ($y/\delta < 0.1$) smooth and rough wall data both exhibited two overlap regions. *Overlap Region I* was defined as the inner variable scaled wave number range where both inner and outer flow variable scaling hold. In this region, the power spectra plotted on log-log axes has a slope of -1 . *Overlap Region II* was defined as the region where both inner and Kolmogorov^{1,2} scaling hold. In this region, the power spectra slope is $-5/3$. In the fully turbulent region, the smooth and rough wall data, with inner variable scaling, the Overlap II region was clearly present for both smooth and rough walls ($k_1 y$ greater than ~ 1). Beyond this region, dissipation becomes important and the energy drops at a faster rate.

The available rough wall database for high-speed flow is not as complete as that for low-speed. For example, rough-wall studies that included turbulence were not included in recent compilations of available mean and turbulent flowfield information.^{3,9} However, the mean flowfield properties have been thoroughly documented.¹⁰⁻¹² Goddard¹⁰ presents a detailed investigation of the influence of Mach number ($M = 0.7 - 4.54$) on the mean velocity and skin friction for sand-grain surface roughness ($k_s^+ \approx 10 - 1500$) boundary layer flow over a body of revolution. The Reynolds number range, depending on Mach number, was nominally $Re_x \approx 2 \times 10^6 - 1 \times 10^7$. Goddard found that the shift in the law of the wall velocity profile was a function of k_s^+ and followed the same law as the incompressible case when the Van Driest Π ¹³ compressibility transformation was used. Berg¹¹ extended the Mach number range to 6.0.

Liepmann and Goddard¹⁴ conjectured that for fully rough flow, the wall shear force is primarily the result of the drag on the roughness elements. Based on this argument, they showed that the ratio of compressible to incompressible skin friction is equal to the wall-to-freestream density ratio. The force balance data of Goddard¹⁰ confirmed the Liepmann and Goddard skin friction correlation over a Mach number range of 0.7 to 5.4. The available skin friction data¹⁰⁻¹² are well correlated (nominal variance of $\pm 15\%$) for $k_S^+ \in [10, 1500]$, $M \in [0.7, 6.0]$ as

$$\frac{C_f}{C_{f0}} = 0.39 \ln(k_S^+) + 0.103 \quad (1)$$

As first observed by Morkovin,¹⁵ it appears that many of the differences in the turbulent statistical properties across supersonic and subsonic smooth plate boundary layers can be explained, or at least correlated, by the thermodynamic property variations across the layer. This observation, termed Morkovin's hypothesis, has provided the rationale for using incompressible turbulence models for flows up to Mach 5. Scaling for compressibility has been found to correlate the mean velocity with the low-speed database across smooth and rough boundary layers.^{10,13} More recently, detailed compilations and analyses of available high-speed turbulence smooth wall data^{3,9,16-18} have been performed. In summary, the studies indicated that the database was insufficient to confirm turbulent property scaling and the realm of applicability of Morkovin's hypothesis might be more restrictive than originally believed.^{3,9,16-18}

Supersonic flows often possess features that do not have incompressible counterparts. For example, supersonic flow over rough surfaces can generate shock and expansion

waves that interact with boundary layer turbulence. This is especially true at higher Mach numbers where most of the boundary layer is supersonic. For a flat plate at Mach 3.0, approximately 99% of the boundary layer is supersonic. Hence, the presence of relatively small roughness elements could generate significant compressibility effects. The overarching objective of this work was to quantify the effect of compressibility on the mean and turbulent flow properties for zero-pressure-gradient rough wall boundary layers.

Chapter 3

Experimental and Numerical Methods

3.1 Wind Tunnels and Models

3.1.1 Supersonic Wind Tunnel

Data were collected in a supersonic wind tunnel located at the Air Force Institute of Technology at Wright-Patterson Air Force Base. The tunnel was a combination draw-down/blow-down facility. A 27.46-cm long (measured from the throat), finite radius, half nozzle was used to produce a freestream Mach number at the nozzle exit of 2.88 with a $\pm 1.3\%$ variation across the test section.¹⁹⁻²² The contoured side of the nozzle was located along the tunnel ceiling. The average axial velocity freestream turbulence intensity at the nozzle exit measured with a cross-film probe was nominally 0.8%.¹⁹⁻²² The stagnation flow conditions for each measurement technique are listed in Table 1. The boundary layer heights δ , δ_M and θ at the nozzle exit were calculated from the velocity profile measured with the Pitot probe (described below) as 4.7, 5.3 and 0.2 mm, respectively. The cross-sectional shape of the test section was square, with each side 6.35 cm in length. For the present study, the test section length, beginning at the nozzle exit, was 66.0 cm, with the measurement location at 54.0 cm downstream of the nozzle exit (see Fig. 1a). The coordinate system was defined such that x was positive in the

freestream flow direction, measured from the nozzle exit; y was positive vertically up relative to the tunnel floor; z completed the right-hand-system, and $z = 0$ was along the tunnel span centerline.

Detailed two-dimensionality studies quantifying the mean and turbulent flow statistics at off center z -locations have been performed for the present facility.¹⁹⁻²² In summary, the mean flow properties were independent of z -location to within the measurement uncertainty over the center 40% of the test section (total area mapped).¹⁹ The turbulent shears stresses at off centerline locations also agreed to within the measurement uncertainty²⁰ (total area mapped was about 20% of the test section). The effects of the longitudinal pressure gradient due to boundary layer growth has also been investigated,^{21,22} and the results demonstrated that the mean and turbulent flow properties measured at x -locations (in the present coordinate system with the origin at the test section exit) of 16.5 cm, 44.0 cm and 54.0 cm (present location) collapsed onto a single curve representative of a zero pressure gradient equilibrium boundary layer with outer scaling.

3.1.2 Subsonic Wind Tunnel

The subsonic measurements took place in a compressible flow blow-down wind tunnel constructed specifically for this project. The wind tunnel is located at The University of Alabama. The test section described in the previous section was used for the subsonic measurements. The measurement location was 50 cm downstream of the nozzle exit. The Mach number was controlled by a converging-diverging diffuser located downstream of the test section. The diffuser was designed for $M = 1.0$ at the throat and M

= 0.1 at the exit, and the area of the throat was varied to achieve a desired Mach number. The test section Mach numbers of $M = 0.25$ and $M = 0.65$ are set by the area ratios of the diffuser throat and test section. The entire wind tunnel facility can be seen in Figure 1b. The mean flow conditions are listed in Table 1b.

3.1.3 Wind Tunnel Models

Six different floor sections were tested, each section having a different surface roughness. The floor sections were, as was the case for the Goddard¹⁰ study, aligned so the tops of the roughness elements were level with the tunnel floor at the nozzle exit (see Figs. 1a and b).

Three sand-grain roughened plates were constructed by adhering Varathane brand 80, 36, and 20 Grit flooring sandpaper to the top surface of three aluminum flat plates (66.0 x 6.35 x 1.91 cm³). The heights of the sand-grains were not measured prior to being glued to the sandpaper surface. For this reason, the roughness heights of the sandpaper were not expected to correspond directly to Nikuradse sand-grain roughness. Instead, direct measurements of the roughness topography using a Carl Zeiss LSM 320 Confocal Laser Scan Microscope (LSM) were acquired. The LSM was used to provide samples of the roughness topology from which the mean, maximum and standard deviation of the surface roughness were computed. The roughness topologies were resolved with the LSM to within 4.0% of the mean roughness height. The statistical properties from this analysis are listed in Table 2. The 20 Grit plate was more sparsely populated with larger elements than the 36 Grit paper. Hence, the average roughness height was smaller for the 20 Grit plate. However, the maximum height and the standard deviation were largest for

the 20 Grit plate. These three rough surfaces were selected because they provided a relatively broad (200 percent) variation in the maximum heights, and all were in the fully rough regime.

Two uniformly machined plates were designed to provide insight into the effects of topology. The geometry was arbitrarily chosen to provide a large variation in the frontal blockage (opposing the flow) and the surface area occupied by roughness elements. The machined, two-dimensional, roughness element model had rectangular lateral grooves that spanned the width of the test section, and the three-dimensional model consisted of cubical pillars (see Fig. 1c) aligned in straight rows in both the x and z directions. The wavelength of the roughness elements was 2.18 mm. The roughness height was chosen as 0.56 mm for both the 2-D and 3-D plates so that both were fully rough. The frontal blockage area for the 2-D plate was the roughness height times the width of the test section, which was 290% larger than that of the 3-D plate. The roughness blockage area for each plate is summarized in Table 2. The surface area occupied by the 2-D plate (25.7%) was 290% larger than that for the 3-D plate (6.6%). The milling machine accuracy was rated at $\pm 22\mu\text{m}$ ($\pm 4.0\%$ of the roughness element height).

3.2 Instrumentation and Data Reduction

3.2.1 Supersonic Experiments

The color schlieren flow visualization equipment consisted of a mercury light source, two 15.24 cm parabolic mirrors (focal length of 1.97 m), a color slide (red-green-blue), and a Kodak Digital 460C CCD camera. Time averaged (0.125-sec) color schlieren

photographs were acquired at the nozzle exit and test location (54.0-cm downstream of the nozzle exit).¹⁹

A Pitot pressure probe was used to measure pressures across the boundary layers for the six models. The Pitot probe was constructed from 1.59 mm diameter stainless steel tubing. The end of the probe was crimped such that the inner cross-section had a height of 0.8 mm and a width of 1.2 mm. Data were sampled at a rate of 800 Hz, and averages were computed over 200 samples. The Rayleigh-Pitot formula was used to compute the Mach number from the measured Pitot pressure. The usual compressible flow relations for thermally and calorically perfect air, with the assumption of an adiabatic flow in the mean, were used to calculate the velocity.

A DANTEC brand 57N Enhanced laser Doppler velocimetry system was used. The use of this laser Doppler velocimetry system in the present facility is documented in Bowersox.²³ A TSI brand six-jet atomizer was used to produce olive oil seed particles. The mean particle size was 0.6 μm . Thus, the mean 3-dB frequency response was 200 kHz and the associated Stokes number was 0.06. Each data point in a given laser Doppler velocimetry profile represents a separate tunnel run. During a given run, data were collected for a period of 12 seconds after the tunnel had reached steady state. Average data rates varied across the boundary layer, but were generally in the range of 0.5 - 2.5 kHz.

A DANTEC brand StreamLine Constant Temperature Anemometry System was used for the cross-film anemometry measurements. TSI Model 1243/AN-20 cross-film probes were used to measure mean and turbulent information in the x-y and x-z planes. The probe sensors were cylindrical with a diameter of 50.8 μm and a length of 1.02 mm. The

sensor separation was 1.09 mm. The frequency response of the cross-film probes was nominally 150 kHz; the data were sampled at a rate of 30 kHz, and statistical averages were computed over blocks of 3000 samples. The present cross-film results were found to be in excellent agreement with hot-wire measurements of Smith and Smits²⁴ (discussed below in the Results Chapter). The probes were calibrated at angles very close to those found in the wind tunnel, thus heat conduction effects to the probe supports was implicitly included in the calibration. Since the boundary layer flows here were essentially adiabatic in the mean,¹⁹ single-overheat cross-film anemometry was used,²³ where the resistance ratio was set to 2.0 to minimize the total temperature sensitivity. Limited multiple overheat data were acquired for the 2-D machined plate, and the measured total temperature fluctuation turbulence intensity levels were less than 3.3%.¹⁹

The combined laser Doppler velocimetry and cross-film anemometry data reduction procedures described in Bowersox²³ (attached as Appendix A) were used in the present study. The compressible Reynolds shear stress for thin layer flow (i.e., $\bar{v}/\bar{u} \ll 1$) is related to the cross-film output, to second order, by the following relation²³

$$\frac{\tau_{xy}^R}{\bar{\rho} \bar{u}^2} \cong -\frac{\overline{u'v'}}{\bar{u}^2} - \frac{\overline{\rho'v'}}{\bar{\rho} \bar{u}} \cong -\frac{\overline{(\rho u)'(\rho v)'}}{(\bar{\rho u})^2} \quad (2)$$

The first two terms on the right-hand-side represents the full compressible Reynolds shear stress and the last term was directly measured with the cross-film. The Favre averaged shear stress is equivalent to the kinematic shear stress [first term on the right-hand-side of Eq. (2)] to fourth order;²³ hence, the Favre averaged shear stress was directly measured with laser Doppler velocimetry.

Two hot-film probe types, normal and parallel, were used to collect high-frequency information in the boundary layer. The normal-film probe measured energy spectra and autocorrelation information and the parallel-film probe measured boundary flow structure angles using the cross-correlation between the two film sensors. The normal-film probe was a TSI Model 1218-20 probe with Platinum sensors mounted to a TSI Model 1150 Single Sensor Probe Support. The parallel-film probe was a TSI Model 1246AD-20 probe consisting of two hot-film sensors positioned normal to the x-y plane, parallel to each other and spaced 1.085 mm apart in the y-axis direction. The parallel-film probe was mounted to a TSI Model 1155 Dual Sensor Probe support. Both of the probes were TSI "-20" hot-film probes with sensor diameters of 50.8 μm , sensor lengths of 1.02 mm, distance between supports of 1.65 mm, and temperature coefficients of 0.0024 1/°C. The present films were chosen over wires because of wire attrition in the supersonic environment. The present measurements were limited to the fully turbulent region of the boundary layer to avoid the uncertainties associated with the spatial resolution of the sensors.

As discussed above, the present sensors were sufficient to resolve the turbulent statistical flow properties. Furthermore, as is discussed in the Results Chapter, the present sensors resolved the spectra into Overlap Region II. A Nicolet Multipro 12-bit data acquisition system was used to collect hot-film voltage data. The Nicolet Multipro system consisted of a chassis unit with four A/D acquisition boards, each with four input channels. The Multipro system acquired each channel at a 1.0MHz rate (non-interlaced) with a maximum of 256K samples per board. The uncertainties for the spectral measurements, which are the focus of this paper, were estimated as described in Bendat

and Piersol.³⁸ The normalized power spectra and auto/cross correlation uncertainties were estimated at 11%.

The high-frequency data collected by the DANTEC Streamline and Nicolet systems were reduced using both discrete Fourier transform and correlation analysis. For the energy spectra analysis, the Nicolet system collected 250,000 samples at a frequency of 1.0 MHz for 0.25 seconds. The data was broken into 23 blocks and reduced using the discrete Fourier transform (DFT) given by

$$V(f) = \frac{1}{N} \sum_N V(t) e^{-\frac{2\pi i f t}{N}}$$

where N is the number of samples, which for the present study was 10,869. The results of the DFT process for each of the 23 blocks was averaged.

The normal-film Eulerian autocorrelation coefficient, $R_E(\tau)$ ³⁹ was computed for each block as

$$R_E(\tau) = \left[\frac{(\rho u)'(t)(\rho u)'(t + \tau)}{(\rho u)^{\prime 2}} \right]^2$$

where again, the results for each of the 23 blocks was averaged. The micro-scale (λ) and integral scale (Λ) were found using the normalized auto-correlated normal-film data. The micro-scale was found by fitting the first few points of the autocorrelation function with an “osculating” parabola and locating the parabola’s positive y-intercept as described in

Cebeci and Smith.³⁹ The integral scale was found by integrating the area under the autocorrelation function from τ equal to zero to infinity.

The parallel-film probe was also used to collect high-frequency boundary layer information. The Nicolet data system was used to collect 128K samples from each of the two, parallel, hot-film sensors at a 1.0MHz rate. The cross-correlation coefficient between the two sensors on the probe was computed using

$$R_E(\tau) = \left[\frac{\left[(\rho u)'(t) \right] \left[(\rho u)'(t + \tau) \right]}{(\rho u)^2} \right]^2$$

The structure angle associated with a large-scale motion can be determined from the time delay between signals (τ), the mean streamwise velocity (u), and the wire separation distance (w) using the following equation¹⁸

$$\theta = \tan^{-1} \left(\frac{w}{\bar{u} \tau} \right)$$

with θ being the structure angle.

The smooth plate skin friction was measured with the floating element skin friction sensor. A detailed description of the gauge and the operating procedure is given in Hazelton et al.²⁵

3.2.2 Subsonic Experiments

The upstream total pressure, total temperature, and static pressure were measured and recorded during all experiments. The upstream total pressure was measured using an Omega model PX202-200 pressure transducer with a range of 0 – 200 psig and an Omega model DP25-S-A signal conditioner with analog output. The static pressure was measured using an Omega model PX202-100 pressure transducer with a range of 0 – 100 psig and a second Omega model DP25-S-A signal conditioner with analog output. The total temperature was recorded using a Type J thermocouple in combination with an Omega model DP25-TC thermocouple meter with analog output capabilities of 0 to 10 volts and a temperature range of 0 – 150° C. The pressure differential between the total and static pressures were also measured during all experiments in order to calculate a freestream velocity and Mach number. This was done with a custom differential pressure transducer manufactured by SensoTec. The transducer had a range of 0 – 15 psid and an output range of 0 – 5 volts.

The Pitot pressure probe used to collect the mean flow data was constructed using a 0.79 mm outer diameter copper tube mounted to a brass support. The tip of the probe was crimped such that the height of the inner portion of the probe was 0.2 mm and the width was 0.41 mm. The Mach number across the boundary layer was found using the pressure ratios of the total and static pressures measured, assuming the static pressure remained constant across the boundary layer. The velocity was calculated using the usual perfect gas assumptions for air.

The Pitot pressure probe measurement was taken using an Endevco model 8510C pressure transducer and an Endevco model 4428A signal conditioner. This combination

has a range of 0 –100 psig with analog output capabilities of ± 5 to 5 volts. The Pitot pressure probe was also used in combination with the aforementioned differential pressure transducer and the static pressure measurement in order to calculate the velocity and Mach number across the boundary layer. The Pitot probe height was recorded using a Linear Voltage Displacement Transducer (LVDT) in combination with the linear traverse. The LVDT used was an Omega Model LD100 transducer with an SP200A signal processor. The analog output capabilities were set to 0 to 5 volts at a range of 0 to 6.35 cm.

The hot-wire anemometry data was taken using an IFA 300 Constant Temperature Anemometer System manufactured by TSI Incorporated. The system consisted of an IFA 300 anemometer cabinet with two channels and a 16 channel A/D board. The IFA 300 cabinet has an analog output range of ± 5 to 5 volts. Hot-film probes were used instead of the more common and fragile hot-wire probes.

The hot-film probe data was collected using the data acquisition system described below at a sampling rate of 50 kHz per channel. The probes used with the anemometry system were TSI models 1243 - 20 and 1218 - 20 hot-film probes. The two probe types used included a single film probe (1218) and a cross film x-y plane probe (1243). The sensors were cylindrical with a diameter of 50.8 μm and a length of 1.02mm. In order to record the height of the hot- film probes in the boundary layer, the LVDT and linear traverse combination described above was used.

The skin friction gages used in the current research were designed and constructed at The University of Alabama. The design was based on the typical floating element skin friction gage. The typical floating element skin friction gage consists of a cantilever beam

attached to a solid base and surrounded by a housing filled with oil. The oil serves two purposes. The first is to provide a thermal insulation around the strain gages. The second is to damp out any dynamic effects. The gages are mounted to the floor models and fitted into the test section. The floor roughness elements are also added to the floating heads of the gages in order to match the roughness patterns of the test floors. A calibration curve was created for each of the six skin friction gages by applying a known force in the direction of the flow. The gage design and a typical calibration can be seen in Figs. 1d and e.

Two semiconductor strain gages were placed at the base of each cantilever beam in order to measure the deflection of the beam. Semiconductor strain gages were used in place of ordinary metal strain gages because they were more sensitive and can therefore measure small deflections very accurately.³ The strain gages were used in combination with an Omega model DP25-S-A strain gage meter capable of analog output in order to record the deflection of the beam and calculate the skin friction force.

All measured data was recorded using an Analog to Digital (A/D) conversion card, a Gateway Pentium PC, and the TestPoint Software package provided by Keithley Instruments. The A/D board used was a model ADCWIN-16 board provided by TSI Incorporated and consisted of 16 channels with a maximum sampling rate of 500 kHz. A program was written using the TestPoint software package to record the different raw data measurements. The Pitot probe data and skin friction gage data was recorded at a sampling rate of 1.2 kHz per channel. The Hot-Wire Anemometry data was recorded at a rate of 50 kHz per channel using the data acquisition system in combination with the aforementioned IFA 300 system and the acquisition software provided by TSI Inc.

3.3 Measurement Uncertainties

3.3.1 Supersonic Measurements

A standard uncertainty analysis,²⁶ accounting for probe location, transducer calibration, and repeatability was performed for the conventional pressure and temperature probe data. The uncertainties in the tunnel stagnation conditions are listed in Table 1a. The position uncertainty was taken as 25% of the smallest division on the measurement standard. The smooth plate floating element skin friction errors have been previously documented.²⁵ The rough wall skin friction was evaluated with an integral method based on the velocity profile (described in Section 4.1.1), and the uncertainty was evaluated by perturbing the inputs (θ , θ and Δx) by the uncertainties listed in Table 3; the uncertainty result is also listed in Table 3. The uncertainty analysis of the laser Doppler velocimetry data accounted for probe volume location, record length, velocity gradient broadening,^{27,28} laser beam angular alignment, seed bias,²⁸ density bias, coincidence filtering and repeatability. The uncertainty estimate procedures are outlined in Luker *et al.*²² The primary sources of uncertainty accounted for in the cross-film data were linearization, calibration, probe position, probe volume and repeatability. The uncertainties in the profile data varied across the boundary layers. Hence, the values at three boundary layer locations are listed in Table 3.

3.3.2 Subsonic Measurements

The uncertainties of the tunnel stagnation conditions and mean flow data are listed in Table 1b. The Pitot and hot-film uncertainties are listed in Table 3. Note, for hot-film results are generalized to include both the subsonic and supersonic test conditions. The uncertainty of the measurements associated with the skin friction gages has been previously documented at 6%.²⁵ However, it was found here that alignment for the skin friction gages proved to be a critical factor and increased the estimated uncertainty to approximately 15%. The skin friction was also evaluated with from the velocity profile using (1) the integral method as described in Section 4.1.2 and (2) the velocity gradient method as described in Section 4.2.1. The friction velocity uncertainties for all three methods are listed in Table 5.

3.4 Numerical Methods

3.4.1 Model Formulations

The Favre averaged differential form of the conservation of mass, momentum and energy equations, where the boundary layer approximations have been invoked, for a thermally and calorically perfect gas are given by

$$\begin{aligned}
\frac{\partial(\bar{\rho}u)}{\partial x} + \frac{\partial(\bar{\rho}v)}{\partial y} &= 0 \\
\bar{\rho}u \frac{\partial \bar{u}}{\partial x} + \bar{\rho}v \frac{\partial \bar{u}}{\partial y} &= -\frac{\partial \bar{p}_e}{\partial x} + \frac{\partial}{\partial y} \left[\mu \frac{\partial \bar{u}}{\partial y} - \overline{\rho u'' v''} \right] \\
\bar{\rho} u c_p \frac{\partial \bar{T}}{\partial x} + \bar{\rho} v c_p \frac{\partial \bar{T}}{\partial y} &= u \frac{\partial \bar{p}_e}{\partial x} + \frac{\partial}{\partial y} \left[k \frac{\partial \bar{T}}{\partial y} - \overline{\rho v'' h''} \right] + \\
&\quad \frac{\partial \bar{u}}{\partial y} \left[\mu \frac{\partial \bar{u}}{\partial y} - \overline{\rho u'' v''} \right]
\end{aligned} \tag{3}$$

The Favre averaged turbulent shear stress was expressed invoking the Boussinesq assumption as

$$\tau_t = -\overline{\rho u'' v''} = \bar{\rho} \mu_t \frac{\partial \bar{u}}{\partial y} \tag{4}$$

where μ_t is the eddy viscosity.

To obtain a generally applicable formula, Prandtl proposed the mixing-length theorem,^{1,30,39} where $\mu_t = \bar{\rho} l_m^2 \left| \frac{\partial \bar{u}}{\partial y} \right|$. In the inner region of the boundary layer

$l_m = \kappa y [1 - \exp(-y^+ / A^+)]$, where $\kappa = 0.4$ and $A^+ = 26^{1,30,33,39,45}$. For the outer region,

$l_m = 0.09 \delta$. However, Clauser's outer region viscosity model, $\mu_t = 0.018 \bar{\rho} u_e \delta^*$, is more commonly used.^{1,30,39}

Van Driest¹³ proposed a vortex generation idea to account for roughness where, when complete roughness is reached, the viscous effect of the wall is eliminated. From a mathematical view, he presented his formula by adding a vortex generation term. The

vortex generation term grows with size of roughness in the form of $\exp(-R^+ y^+ / A^+ k^+)$ such that when $y^+ = k^+ = 60$. Thus, the van Driest model is given by

$$l_m = ky \left[1 - \exp(-y^+ / 26) + \exp(-y^+ R^+ / 26 k^+) \right] \quad (5)$$

where $R^+ = 60$.

Kragstad⁴⁴ presented a modified damping function similar to that of Van Driest, where in the damping function the term (R^+ / k^+) was taken to 3/2 power, and $R^+ = 70$. For higher values of k^+ , a square root term was added to increase the mixing. Thus, the Kragstad formula for the mixing length is

$$l_m = 0.085 \delta \tanh\left(\frac{Kv}{0.085 \delta}\right) \left\{ 1 - \exp(-y / A^+) + \exp\left[-y^+ / A^+ (R^+ / k^+)^{3/2}\right] \sqrt{1 + \exp(-R^+ / k^+)} \right\} \quad (6)$$

The model used by Cebeci-Chang⁴³ is somewhat different than the two described above, where a displacement Δy related to the averaged roughness height is defined, and the velocity profile is obtained by a shift of the smooth wall profile. To generate the analogous smooth plate profile, the reference plane was shifted in the opposite direction to main flow. Based on the law of wall and the mixing length formulation, a displacement formula relative to roughness was obtained. Thus, the mixing length was modified by a displacement to account for the roughness effect as follows

$$\begin{aligned}
l_m^+ &= \kappa(y^+ + \Delta y^+) \{1 - \exp[-(y^+ + \Delta y^+) / A^+]\} \\
\Delta y^+ &= 0.9[\sqrt{k_S^+} - k_S^+ \exp(-k_S^+ / 6)] \\
4.535 &< k_S^+ < 2000.
\end{aligned}$$

(7)

In the formulae for the mixing length [Eq. (5-7)], the friction velocity is required; i.e., the wall shear stress needs to be calculated. For a smooth plate, $\tau_w = \mu \hat{c}u / \hat{c}y|_{y=0}$. However, this equation is not sufficient by itself for the rough-walls because the shear stress at wall consists of two parts, viscous shear and form drag due to roughness elements. Because of this, the wall shear stress was found from the integral momentum equation for a flat plate; i.e., $C_f / 2 = d\theta / dx$. For the present simulations, the momentum gradient along x-direction was calculated with a first-order finite-difference approximation.

The finite difference formulations used here for variable spacing in y-direction were derived from Taylor series expansions.⁴⁵ Since the system of governing equations for boundary layer flow is parabolic in the x-direction, the solution was obtained by forward-step-marching in the x-direction. The x-location of a grid point within the domain is denoted with the subscript i , where the superscript j indicates the y-location. The implicit linear, second-order finite-difference equations are described in Ref. [1,30,39]. Explicit schemes were used for the first order derivatives, with the coefficients lagged to the previous station.

Defining the following variables for convenience

$$\alpha_1 = \frac{2\mu_i^j \Delta x \theta_j}{\rho_i^j u_i^j \Delta y_j^2 (1 + \theta_j)}, \quad \alpha_2 = \frac{2\mu_{t,i}^j \Delta x \theta_j}{\rho_i^j u_i^j \Delta y_j^2 (1 + \theta_j)},$$

$$\alpha = \alpha_1 + \alpha_2, \quad \beta = \frac{v_i^j \Delta x}{(1 + \theta_j) u_i^j \Delta y_j},$$

$$\varsigma_1 = \frac{\mu_i^{j+1} - (1 - \theta_j^2) \mu_i^j - \theta_j^2 \mu_i^{j-1}}{(1 + \theta_j)^2 \Delta y_j^2 \rho_i^j u_i^j} \Delta x,$$

$$\varsigma_2 = \frac{\mu_{t,i}^{j+1} - (1 - \theta_j^2) \mu_{t,i}^j - \theta_j^2 \mu_{t,i}^{j-1}}{(1 + \theta_j)^2 \Delta y_j^2 \rho_i^j u_i^j} \Delta x$$

$$\varsigma = \varsigma_1 + \varsigma_2$$

The final form of the finite-difference equations for the conservation of x-momentum, energy and mass, respectively, are written as

$$\begin{aligned} & -\theta_j \alpha u_{i+1}^{j-1} + [1 + (1 + \theta_j) \alpha] u_{i+1}^j - \alpha u_{i+1}^{j+1} = \\ & [1 + (1 - \theta_j^2) \beta + \varsigma (\theta_j^2 - 1)] u_i^j + [\theta_j^2 \beta - \varsigma \theta_j^2] u_i^{j-1} \\ & + (\varsigma - \beta) u_i^{j+1} + \frac{\rho_e (u_{e,i+1}^2 - u_{e,i}^2)}{2(\rho u)_i^j} \end{aligned} \quad (8a)$$

$$\begin{aligned} & -\theta_j \left(\frac{\alpha_1}{Pr} + \frac{\alpha_2}{Pr_t} \right) T_{i+1}^{j-1} + [1 + (1 + \theta_j) \left(\frac{\alpha_1}{Pr} + \frac{\alpha_2}{Pr_t} \right)] T_{i+1}^j \\ & - \left(\frac{\alpha_1}{Pr} + \frac{\alpha_2}{Pr_t} \right) T_{i+1}^{j+1} = \left[1 + (1 - \theta_j^2) \beta + (\theta_j^2 - 1) \left(\frac{\varsigma_1}{Pr} + \frac{\varsigma_2}{Pr_t} \right) \right] T_i^j \\ & + \theta_j^2 \left[\beta - \left(\frac{\varsigma_1}{Pr} + \frac{\varsigma_2}{Pr_t} \right) \right] T_i^{j-1} + \frac{\alpha (u_{i+1}^{j+1} - (1 - \theta_j^2) u_{i+1}^j - \theta_j^2 u_{i+1}^{j-1})^2}{c_p \cdot 2\theta_j (1 + \theta_j)} \end{aligned} \quad (8b)$$

$$\begin{aligned} v_{i+1}^j &= \frac{(\rho v)_{i+1}^{j-1}}{\rho_{i+1}^j} - \frac{\Delta y_j}{2\rho_{i+1}^j \Delta x} \\ & [(\rho u)_{i+1}^j - (\rho u)_i^j + (\rho u)_{i+1}^{j-1} - (\rho u)_i^{j-1}] \end{aligned}$$

(8c)

where $\theta_j = \Delta y_j / \Delta y_{j-1}$.

Equations (8a) and (8b) represent two tridiagonal linear systems of equations with diagonal dominance, and were thus solved by the Thomas algorithm for u and T . Since the pressure was constant across the flow, the density at each node was calculated as $\rho_{i+1}^j = T_e \rho_e / T_{i+1}^j$. The vertical velocity v was explicitly calculated with Eq. (8c).

3.4.2 Solution Accuracy and Stability

The momentum and energy difference equations truncation error was found to be $O[(\Delta x, (1-\theta)\Delta y)]$. The variable grid spacing seemed to degrade the formal truncation error though Blottner, as described in Anderson et al.⁴⁵, indicated the treatment of derivatives with a constant θ in the Crank-Nicolson scheme was locally second order accurate. It was found in this study, though a series of numerical experiments, that the variable spacing had negligible effect on the solutions.

A von Neumann stability analysis indicated that the implicit scheme was unconditionally stable. For the nonlinear flow problems, however, numerical instability may occur if convective transport dominate diffusive transport due to some choice of grid spacing.⁴⁵ The momentum and energy difference equations satisfied the stability requirements because these schemes were both implicit and diagonally dominant.

A grid convergence study was performed for the smooth plate and the 36-grit sand-grain plate using the van Driest model. A 500X350 mesh produced a grid-converged solution. Refining the grid to 600X400 changed the skin friction coefficient, boundary layer thickness, and velocity profile by less than 0.5%. Also, the effects of the initial grid

spacing (Δy_l) were examined, and the difference in C_f for Δy_l between 1×10^{-6} and 2×10^{-6} m was 1.5%. The effect of the variable spacing ratio parameter θ was also studied. The predicted results were virtually identical for $\theta \in [1.02, 1.06]$; e.g., C_f varied by less than 0.5%. Hence, the grid for all six plates consisted of 350 vertical nodes ($\theta = 1.02$, $\Delta y_l = 1.0 \times 10^{-6}$) and 500 evenly spaced axial nodes ($\Delta x = 1.67 \times 10^{-3}$).

3.4.3 Initial and Boundary Conditions

To obtain a unique solution of the parabolic initial and boundary-value problem, the inflow, freestream and wall boundary conditions were needed. The freestream flow conditions were based on the experimental Pitot pressure measurements for the six flow models (described in the next section). Two types of inflow boundary conditions were tested. The first consisted of a uniform flow starting at a x -location that was equivalent to the wind tunnel nozzle throat. The second condition started the simulation at the x -location where the roughness began. The inflow velocity and temperature profiles were constructed by calculation over a flat plate until the boundary layer thickness matched that of experimental data ($\delta = 5.0$ mm). The two inflow boundary conditions were shown to have consistent results, where the differences in boundary layer heights and skin friction coefficients were within 6% and 2%, respectively. Hence, the uniform inflow boundary condition was used for the results presented below. Along with the usual no-slip boundary condition, the Dirichlet type condition for temperature was used, where the temperature was fixed at the experimental values (described in the next section). A Neumann adiabatic wall boundary condition was also tested and the results were virtually

identical to those obtained with the fixed wall temperature (e.g., C_f varied by less than 1.0%).

Chapter 4

Results and Discussion

4.1 Supersonic Experimental Results

4.1.1 Flow Visualization

Color schlieren photograph centered on $x = 4.3$ cm (near the beginning of the roughened floor) are presented in Fig 3. The rough surface was along the lower wall and the flow was from the right. At this location, shock and expansion waves were generated by the individual roughness elements protruding into the supersonic portion of the boundary layer for all but the 2-D machined plate (the 2-D machined plate is discussed in the next paragraph). The location of the sonic line at the nozzle exit was estimated from the theoretical velocity profile (with Van Driest II scaling) as 0.07 mm. Thus at the nozzle exit, all of the roughness elements protruded deep into the supersonic region (see Table 2 for maximum roughness heights) of the boundary layer. The strength and intensity of the waves increased as the roughness height increased. These roughness generated waves distorted the boundary layer edge and were clearly visible in the freestream.

The 2-D plate had a λ/k ratio of 3.9 which is referred to as a “d-type” roughness.^{7,8} Perry et. al.⁷ remarked that, for a “d-type” rough-wall, “the outer flow rides relatively

undisturbed over the crests of the elements." Hence, the lack of waves was not surprising.

At the measurement location ($x = 54.0$ cm), roughness generated waves were not visible. The Mach number measurements at $y/\delta \approx 0.03$ (relative to the tops of the roughness elements) were ≤ 1.0 for all but the 80 Grit plate, which was 1.2. Hence for all but the 80 Grit plate, the roughness elements did not extend into the supersonic portion of the boundary layer at measurement location; it is also unlikely that the 80 Grit elements protruded significantly into the supersonic flow.

Noticeable in Fig. 3 is a nozzle exit and test section seam interface wave and a wave emanating from the nozzle exit upper surface. The angles of the waves were measured as approximately 21.0° , which is close to the Mach angle (20.3°); thus, these waves were very weak and the disturbances were undetectable with the present laser Doppler velocimetry instrumentation.

4.1.2 Mean Flow Measurements

The velocity profiles for each of the six models measured with the laser Doppler velocimetry system and estimated from the Pitot pressure profiles at the test location are shown in Fig 4a. All velocity profiles are presented with the local velocity and boundary layer height nondimensionalized by the model specific freestream velocity (u_e) and boundary layer thickness (δ), respectively. Measured reference values at the test location are summarized in Table 4. The freestream velocities measured using the two methods were in excellent agreement (average difference of 0.3%). The data from Goddard¹⁰ and Fiore²⁹ (as shown in Goddard¹⁰) agreed reasonably well with the present experiments, the

slight differences were attributed to Reynolds number differences and errors in reading data from Goddard's figures. The 80 Grit Pitot data indicated a slightly smaller defect than the other rough plates, which indicated that the 80 Grit plate for the Pitot data ($k_s^- = 100$) was in the transitional roughness regime. The remaining fully rough velocity profiles in Fig. 4a all collapsed reasonable well onto a single curve.

The integral boundary layer heights³⁰ were estimated from the velocity profile, where the density profile was estimated from the *Modified Crocco Integral*³⁰ (discussed below). The integral boundary layer heights along with Re_θ are listed in Table 4. $Re_{\theta_2} \equiv (\rho_e u_e \theta / \mu_w)^{9,18}$ has been defined as the proper Reynolds number to characterize the state of the boundary layer. For the present study, $Re_\theta / Re_{\theta_2} \approx 2.2$. Hence, the present is in the medium Reynolds number category.¹⁸

The skin friction coefficient, C_{f0} , for the smooth plate was measured with a floating element skin friction gauge. In addition, C_{f0} was estimated using the Van Driest II skin friction relationship⁸ assuming that the flow could be modeled as a flat plate with the origin at the nozzle throat. The direct measurement and the Van Driest estimate agreed to within 1.0%. This excellent agreement was unexpected since the skin friction measurement uncertainty was estimated as nominally 6.0%,²⁵ and the accuracy of the Van Driest correlation is generally accepted to be 10%.³¹

The rough plate skin friction values were calculated using the fully rough law of the wall evaluated at the boundary layer edge,³⁰ specifically, $\sqrt{2/C_f} = 1/\kappa \ln(\delta/k) + B$, where k is the roughness height, $\kappa = 0.41$, and B is a constant. Rewriting the above equation using the momentum thickness, and assuming that θ/δ was constant

gave $\sqrt{2/C_f} = 1/\kappa \ln(\theta/k) + B'$. Combining the above equation with the zero pressure gradient momentum integral equation given by $C_f/2 = d\theta/dx$ and integrating gave

$$\left\{ \frac{1}{\kappa^2} \frac{\theta}{k} \left[\ln^2 \frac{\theta}{k} - 2 \left(\ln \frac{\theta}{k} - 1 \right) \right] + \frac{2B'}{\kappa} \frac{\theta}{k} \left(\ln \frac{\theta}{k} - 1 \right) + B'^2 \frac{\theta}{k} \right\} \bigg|_{\theta_i/k}^{\theta_f/k} = \frac{\Delta x}{k} \quad (9)$$

With known values θ_i , θ_f , k , and Δx , the constant B' was calculated with Eq. (9) for each plate, and the corresponding skin friction coefficient was found from the law of the wall formula listed above. The values for θ_f (θ at $x = 54.0$ cm) for each plate are summarized in Table 4; $\Delta x = 54$ cm, and k are mean values summarized in the first column of Table 1. θ_i was the momentum thickness at the nozzle exit (listed in Chapter 3). The skin friction values, along with B' , from this analysis are listed in Table 4. The present skin friction estimates agreed with Eq. (1) to within 3.0%.

Because the turbulent boundary layer was of finite thickness at the beginning of the rough surface, an effective length (Δx_o) of the rough surface was calculated using Eq. (9) by integrating from $\theta = 0$ to θ_i . The resulting effective starting lengths are listed in Table 4. For the smooth plate, the length of the wind tunnel nozzle was assumed. The resulting Reynolds numbers based on x ($x = \Delta x_o + \Delta x$) are also listed in Table 4; the variances account for the stagnation condition variations listed in Table 2.

The defect law, with the Van Driest II compressibility transformation, for all six plates, is shown in Fig. 4b. By scaling the velocity defect with the friction velocity, all of the models collapse onto a single curve. Also included on Fig. 4b is the correlation^{30,32,33}

$$\frac{u_{eff} - u_{e,eff}}{u^*} = -\frac{1}{\kappa} \ln\left(\frac{y}{\delta}\right) + \frac{2\Pi}{\kappa} \left[1 - \sin^2\left(\frac{\pi}{2} \frac{y}{\delta}\right)\right] \quad (10)$$

where Π was estimated following White³² as $0.8(\beta+0.5)^{3/4} \approx 0.475$ and $\kappa = 0.41$. The agreement between the incompressible theory [Eq. (10)] and the data was considered excellent. The main differences between the theory and the data are attributed to the determination of the boundary layer thickness. Based on the previously reported success of the Van Driest II scaling¹³ and the collapsing of low-speed smooth and rough wall defect law data,³⁰ the observed collapsing of the present data with Van Driest II scaling was the expected result.

The law of the wall plot with Van Driest II scaling is shown in Fig. 4c. The law of the wall,^{30,32,33} given by

$$u_{eff}^+ = \begin{cases} y^+, & y^+ < 10 \\ \frac{1}{\kappa} \ln y^+ + 5.5 + \frac{2\Pi}{\kappa} \sin^2\left(\frac{\pi}{2} \frac{y}{\delta}\right), & y^+ \geq 10 \end{cases} \quad (11)$$

is also shown, where again $\Pi \approx 0.475$. As expected, the smooth plate data with Van Driest scaling⁸ are in excellent agreement with the accepted theory. The equivalent sand-grain roughness heights (k_s) were calculated from the velocity profiles and the skin friction data as outlined in Schlichting¹ and Antonia and Wood.⁶ The resulting k_s and k_s^+ values are listed in Table 1.

The density profile measurements for each of the six models, acquired with cross-film and laser Doppler velocimetry systems (i.e., $\bar{\rho} \cong \overline{\rho u} / \bar{u}$), are compared to the *Modified Crocco Integral*³⁰ estimate, obtained from the mean velocity measured with the Pitot probe, in Fig. 4d. The agreement (10%) between the two methods for the smooth plate was considered good. The differences for the rough wall plates were larger, but were within the measurement uncertainty listed in Table 3.

4.1.3 Turbulence Measurements

The velocity turbulence intensities measured using the laser Doppler velocimetry system for all six models are shown in Fig. 5. Focusing first on the outer scaling plot (Fig. 5a), it was found that the rough plate u - and v -component turbulence intensity profiles collapsed when scaled by the local u -component of the mean velocity and boundary layer height. The rough plate turbulence intensities (both components) were approximately twice the smooth plate values, with the largest, rough wall, u -component velocity turbulence intensity at 18.0% versus 9.0% for the smooth plate case. For the v -component turbulence intensity, the largest rough plate value was approximately 9.0% versus 4.0% for the smooth plate case. The incompressible rough wall results from Corrsin and Kistler⁸ are shown for comparison purposes. As indicated, their data agrees very well with the present measurements considering the large differences in flow conditions. Compressibility scaling¹⁵ was omitted so that only directly measured data are presented in Fig. 5a.

The present turbulence data were mostly in the outer region, however plotting with inner variable scaling did produce discernable trends in the rough wall data. Shown in

Fig. 5b are the turbulence intensity results normalized by the friction velocity plotted versus y^+ . The smooth plate levels shown in Fig. 5b are consistent with the incompressible data of Klebanoff³⁴ and the Mach 2.3 data of Elena and Lacharme,³⁵ as shown in Dussuage et al.¹⁰ The rough wall axial data merged with the smooth wall data as the wall was approached when scaled for compressibility (as shown). Conversely, the transverse rough wall fluctuations merged with the smooth wall data as the wall was approached when plotted without the compressibility transformation (as shown).

Both the u - and v -component turbulence intensity profiles with mixed scaling (i.e., inner variable scaled turbulence intensity versus y/δ) is shown in Fig. 5c. The curves collapsed very well for $y/\delta < 0.6$. The only exception was the axial results for the 2-D machined plate (discussed in the next paragraph). Further out into the boundary layer, the curves diverged and a discernible trend with roughness Reynolds number was observed. For both components, increasing the roughness shifted the curves vertically down on Fig. 5c.

The 2-D machined plate turbulence intensities (as shown in Fig. 5a-c) did not collapse as well near wall ($y/\delta < 0.4$). As discussed above, the 2-D plate was also the only plate that did not produce shock and expansion waves. Hence, the 2-D plate turbulence production mechanisms in the inner region, which were most likely driven by cavity flow dynamics,^{7,34} were fundamentally different than that for the other plates, where the roughness elements were all three-dimensional.

The ρu -component turbulence intensity profiles measured with the cross-film probes are shown in Fig. 6. The profiles with outer variable scaling are given in Fig. 6a. Smooth wall normal-wire Mach 2.9 boundary layer data from Smith and Smits²⁴ are

included in Fig. 6a for comparison purposes. Smith and Smits based their boundary layer thickness (δ) on a total pressure ratio criterion of 98%, which was approximately equal to δ_M in the present study. Hence, the Smith and Smits y/δ values of included in Fig. 6a were re-scaled to the present definition (99% of u_e) by multiplying by δ_M/δ . Since normal-wire probes respond to the magnitude of the mass flux vector, the magnitude of the present cross-film results $\sqrt{(\rho u)'^2 + (\rho v)'^2}$ is plotted for comparison. In the boundary layer, the present cross-film results (open triangles) are in very good agreement (to within the measurement uncertainties listed in Table 3) with the normal-wire data (open circles). In the free stream, the present results are higher than those of Smith and Smits;²⁴ these discrepancies were attributed to both facility differences and sensor resolution.

From an examination of the rough wall data plotted in Fig. 6a, it was apparent that the mass flux turbulence intensity did not scale by the local mean flow as was the case for the u - and v -component turbulence intensities measured by laser Doppler velocimetry (Fig. 5a). Instead, a systematic increase with increasing roughness Reynolds number was observed. The mass flux turbulence intensities for each of the six models reached a maximum for y/δ in the range of 0.6-0.8. The relative increase with roughness is discussed below. The cross-film freestream ρu turbulence intensity levels were 3 - 4%, with the value increasing slightly with increasing equivalent roughness height. It was expected that the shock and expansion waves that were generated by the roughness elements (Fig. 3) created slight increases in the freestream density fluctuations.

The ρu -component turbulence intensities scaled by the wall density and the friction velocity as a function of y^+ are shown in Fig. 6b. Presented in Fig. 6c are the ρu -

component turbulence intensities scaled by the wall density and the friction velocity as a function of y/δ . In the region $y^+ \approx 500$ to 1300 in Fig. 6b for the smooth plate, the mass flux turbulence intensity increased to a distinct peak at $y^+ \approx 1600$. From Fig. 6c, the corresponding region was bounded by $y/\delta \approx 0.25$ to 0.6, and the peak was located at $y/\delta \approx 0.75$. Following the peak, the turbulence levels dropped off to the freestream values. The rough wall data (Figs. 6b and 6c) followed a similar trend as the smooth wall data. In Fig. 6b curves were shifted toward higher values of y^+ . In the region bounded by $y^+ \approx 1000$ to 3500 (Fig. 6b) or $y/\delta \approx 0.3$ -0.8 (Fig. 6c), the rough plate data were seen to collapse (the 80 Grit plate in Fig. 6b is the exception and is discussed in the next paragraph) onto single almost linear curve. The rate of increase of the rough-wall curves in region closest to the wall was significantly lower than that for the smooth plate in Fig. 6b, where the level of reduction of the slope, depended on the scaling, was approximately 30% (Fig. 6b) and 70% (Fig. 6c). The peak turbulence intensity level and the location of the peak in terms of y^+ (Fig. 6b) increased with increasing roughness Reynolds number. In Fig. 6c, the peak values for the rough walls were nearly collocated at $y/\delta = 0.8$; the largest roughness element plate peak was slightly further out into the boundary layer ($y/\delta = 0.84$). The smooth plate peak was clearly the largest, which coupled the increasing peak value with roughness Reynolds number, indicated that the wall shear stress increased more than the turbulence levels for the smaller roughness heights, and as the roughness height increased, the relative production of turbulence by the roughness increased.

In Fig. 6b, the 80 Grit data did not collapse onto the rough wall curve for $y^+ \approx 1000$ to 3500. Recall the velocity profile obtained with the Pitot probe indicated that the 80 Grit

plate data were in the transitional regime, and the cross-film data appear to have confirmed that conclusion. Hence, it is expected that a family of transitionally rough curves span the space between the smooth and fully rough plate limits. Interestingly, the kinematic velocity and turbulence data did not indicate that the 80 Grit plate was transitional. Two possible explanations for this apparent discrepancy are given. First, the 10% higher Reynolds number for the laser Doppler Velocimetry data, as compared to the Pitot and cross-film tests, might have been sufficient to shift the curve. Second, the inherent thermodynamic sensitivity of the cross-film and Pitot probes could imply that the boundaries of the roughness regimes depend on compressibility.

The ρv and ρw turbulence intensity profiles did not collapse when scaled with outer or inner variables. The effects of roughness on the turbulence levels are apparent in the results (outer scaling) plotted in Figs. 7 and 8. The maximums for both ρv - and ρw -components were located at the lowest point in the profile.

The peak ρu -, ρv -, and ρw -component turbulence intensity differences relative to the smooth plate peak, $\Delta(\rho^*)$, from Figs. 6a, 7 and 8 are plotted versus roughness Reynolds number in Fig. 9. The sand-grain roughness mass flux turbulence intensity difference data points were reasonably well fit with a line indicating that increasing the roughness height, increased the mass flux turbulence intensity almost linearly. The ρw -turbulence intensity difference had the largest rate of increase (slope of the linear fit was 1.1×10^{-4}). The ρu -turbulence intensity difference had the second largest rate of increase (slope = 7.3×10^{-5}), and the ρv -component was the smallest (slope = 5.6×10^{-5}). If the fluctuation magnitude is assumed to correspond to the eddy size, then the sand-grain trends indicated

that increasing the roughness increased the lateral dimension of the eddies more than the axial or transverse dimensions.

The 2-D plate results in Fig. 9 were well above the sand-grain trend for both axial and spanwise components, and below the trend for the transverse component. Hence, the growth of the structures in the spanwise and axial direction was significantly larger than the sand-grain trend, which was consistent with the structures that would be shed from cavities. The transverse dimension for the present 2-D geometry was smaller than that produced by a sand-grain plate with the same equivalent roughness height, which coupled with the d-type flow explains the smaller transverse fluctuations as compared to the sand grain trend. The 3-D plate transverse and spanwise turbulence intensity values were well below the sand-grain trends. Considering that the 3-D plate roughness elements were relatively sparse as compared to the 2-D and sand-grain plates (i.e., 93.4% of the 3-D plate test surface was smooth), the smaller increase in the fluctuation levels was expected. Although, significant differences between the machined and sand-grain results were discernible, the equivalent sand-grain roughness concept was a reasonable parameter to characterize the influence of roughness on the turbulence intensity levels for all six plates, where the results were all within approximately 10% of the trends shown in Fig. 9.

The kinematic Reynolds shear stress data is presented in Fig. 10. Smooth plate laser Doppler velocimetry^{21,22} and cross-film measurements³⁷ obtained in the same facility are included in Fig. 10a for comparison purposes. Excellent agreement between the present and previous studies was found.

The kinematic Reynolds shear stress data for each roughness model collapsed on to a single curve when scaled by the local mean streamwise velocity (Fig. 10a). As was the case for the velocity turbulence intensity data (Fig. 5), the 2-D plate shear stress data for $y/\delta < 0.4$ were lower in magnitude than those associated with the other five models. The agreement between the present rough wall data and the incompressible results from Corrsin and Kistler⁸, without the compressibility transformation, was considered very good considering the differences in flow conditions. The present smooth plate kinematic Reynolds shear stress profiles reached a maximum value of approximately 0.0020, while the rough surface plates reached 0.0077, an increase of 285%.

The inner variable scaled results are shown in Figs. 10b and 10c. Plotting y^+ on linear or logarithm scales did not collapse the data (Fig. 10b). Because the smooth plate boundary layer thickness and friction velocity were significantly lower, the smooth plate data lied on a curve that was shifted toward smaller y^+ values. As was the case for the velocity turbulence intensities, the turbulent shear stress profiles (omitting the 2-D plate results) with inner variable scaling collapsed reasonably well when plotted versus y/δ (Fig. 10c).

The x - y plane full compressible Reynolds shear stress [Eq. (2)] profiles, measured with the x - y plane cross-film probe, are shown in Fig. 11. Focusing first on the outer-scaled results (Fig. 11a), the compressible Reynolds shear stress did not collapse onto a single curve, as was the case for the kinematic Reynolds shear stresses (Fig. 5a). The compressible Reynolds shear stress for the smooth model reached a peak near $y/\delta \approx 0.3$ -0.6. The rough wall profiles were more complicated. First, the profiles reached a peak in the outer region near $y/\delta \approx 0.6$, and the magnitude of the peak was found to depend

strongly on the equivalent roughness height. Second, a minimum (or a relatively sharp change in slope) in the profile was observed near $y/\delta \approx 0.4$, followed by an increase as the wall was approached. The compressible Reynolds shear stress levels with inner and mixed scaling (Figs. 11b and 11c) display similar trends as the axial turbulence intensities (Figs. 6b and 6c). Hence, those discussions are not repeated here.

The x - z plane compressible Reynolds shear stress also did not collapse when scaled with inner or outer variables. The results with outer variable scaling are shown in Fig 12. Unlike the x - y data, the x - z plane values did not reach a peak over the distance measured, but increased continuously with decreasing boundary layer height.

The x - y and x - z compressible Reynolds shear stress peak differences relative to the smooth plate peak scaled by the local mean streamwise mass flux for the five rough surface models versus roughness Reynolds number are shown in Fig. 13. The sand-grain roughness results for both components were nearly linear with k_s^+ . The 3-D plate result agreed very well with the linear x - z component trend (slope = 3.7×10^{-5}) established by the sand-grain plates. However, 2-D model result was significantly (25%) above the trend, which indicated that the turbulent structures for the 2-D plate were more correlated in the x - z plane than predicted by the trend. This result is consistent with the turbulence intensity data presented in Fig. 9. The x - y component sand-grain results also increased linearly, but at a much lower rate than the x - z component (x - y slope = 5.6×10^{-6}). The 3-D plate result was well below (20%) the trend. Because 93.4% of the wall surface area was smooth for the 3-D plate, the usual wall damping effects³⁰ on the transverse fluctuation levels were expected.

Combining the cross-film and laser Doppler velocimetry measurements allowed for the estimation of correlation between the transverse velocity and density fluctuations,²³ i.e., $\overline{\rho'v'}/\overline{\rho u}$, which is equal to the negative of the Favre averaged velocity fluctuation, $-\overline{v''}/\overline{U}$. Presented in Fig. 14a are the velocity-density correlation results with outer scaling. Since $\overline{\rho'v'}/\overline{\rho u}$ was a combination of the kinematic Reynolds and x - y compressible Reynolds shear stresses, and since the kinematic Reynolds shear stress profiles with outer scaling nearly collapsed for all of rough surfaces, data with outer scaling exhibited similar trends as the Reynolds shear stress data (Fig. 11a). Plotting the peak density-traverse velocity correlation difference, $\Delta_{\rho'v'}$, scaled by the local mean streamwise mass flux¹⁹ indicated that the rate of increase was approximately linear, and the slope was 8.0×10^{-6} . However, the scatter about the trend was nominally 12%. Hence, conclusions concerning the effects of roughness geometry were not discernible.

The transverse-velocity-density correlation with inner scaling is shown in Fig. 14b. Overall, the results strongly resemble the compressible Reynolds shear stress data shown in Fig. 11b. However, the nearer to the wall ($y^+ \approx 1000$ to 2500) the velocity-correlation data did not collapse as well as the Reynolds shear stress data. The poor collapsing of the near wall data is explained by recalling that the kinematic shear stress levels (Fig. 10a) did not collapse in this region of the boundary layer, and using the strong Reynolds analogy¹⁵ [$\overline{\rho'v'}/\overline{\rho u} = (\gamma - 1)M^2 \overline{u'v'}/\overline{u^2}$] to compare the relative magnitudes of the kinematic and compressible terms in the Reynolds shear stress. Away from the wall where the Mach number was relatively large, the velocity-density correlation was the dominant term the compressible Reynolds shear stress. For example at $y/\delta = 0.7$, the mean Mach number for the rough plates was nominally 2.6, and the ratio of the second-

to-first term in the Reynolds shear stress [i.e., on the right-hand-side of Eq. (2)] was, based on the strong Reynolds analogy, 2.7. Closer to the wall, where the Mach number was small, the kinematic Reynolds shear stress term [first term on the right-hand-side of Eq. (2)] became more important. At $y/\delta = 0.2$, the mean Mach number for the rough plates was nominally 1.4, and the ratio of the second-to-first term in the Reynolds shear stress was 0.8. Hence, it was not overly surprising that the data did not correlate as well closer to the wall.

4.1.4 Spectral and Correlation Results

A normal-film probe was used to collect the frequency resolved spectra at three locations within the boundary layers, $y/\delta_M = 0.25, 0.50$, and 0.75 , over all six wind tunnel models. As mentioned in the Instrumentation Section, these data points were all in the fully turbulent region of the boundary layer. The frequency resolved measurements provide information on the distribution of turbulent mass flux power over a range of frequencies from 1.0 kHz to the normal-film frequency response of 120 kHz. For all normal film probe measurements, the tunnel was operated at a stagnation pressure of $2.41 \cdot 10^5 \pm 0.2\%$ Pa and a stagnation temperature of 296 ± 1.0 K.

In the previous sections, it was demonstrated that the equivalent sand grain height was a useful concept to generalize the effects of roughness on the mean and turbulent statistical flow properties across the boundary for the present wind tunnel models. However, significant topology influences were discerned for the machined plates and were fully discussed. The method of presentation here is to discuss the results in terms of k_s . However, topology effects are discussed when apparent.

Figures 15a-c show the dimensional power spectra [units of $(kg/m^2s)^2$] for each of the six models at the three boundary layer regions ($y/\delta_M = 0.25, 0.50$, and 0.75). Noticeable in all of the spectra are relatively small spikes in the data, the largest of which is located at ~ 30 kHz. This frequency corresponds to a Strouhal⁴⁰ number based on the probe holder diameter of the approximately 0.22. Hence, these spikes are most likely the result of Von Karman vortex sheet induced probe vibrations.

For the smooth plate, the mid-point location had the largest energy levels, followed by the outer, and then the lowest position; however, these differences were relatively small. These data also demonstrated that for the rough wall models, the largest energy levels were in the outer region ($y/\delta_M = 0.75$) of the boundary layer, and the energy was fairly evenly distributed across a wide range of frequencies (approximately 1.0 kHz to 20 kHz). The near wall point ($y/\delta_M = 0.25$) had the least overall power, which was contained in large-scale low-frequency structures. The $y/\delta_M = 0.50$ spectra appeared to be a blending of the upper and lower regions, containing more overall energy than the lower region, spread over a larger range of frequencies.

To provide more detail into the effects of surface roughness on power spectra, Figs. 16a-c show the square root of the power spectra difference for frequencies less than 10 kHz, relative to the flat plate, normalized by the mass flux standard deviation; i.e.,

$$\Delta_{pu(f),rms} = \left(\sqrt{\frac{(\rho u)'^2(f)}{(\rho u)'^2}} \right)_{rough} - \left(\sqrt{\frac{(\rho u)'^2(f)}{(\rho u)'^2}} \right)_{smooth}$$

for the three boundary layer locations for all size models. In general, these data show that that increasing surface roughness height had the effect of increasing the power spectra difference. However, the magnitude of the increase was dependent on both the frequency and boundary layer location. At the lowest point (Fig. 16a), the largest increases in turbulent energy occurred at the lower frequencies, and the spread in the increased with roughness height. Further away from the wall, the effect of increasing roughness height and blockage was spread over a larger range of frequencies (Figs. 16b and c).

A relatively strong topology effect is also noticeable in Figs. 16a-c. The effect is most apparent at $y/\delta_M = 0.75$, however the trend is noticeable at all three locations. Specifically, if a curve were fit to the sand paper results, the differences between the two- and three-dimensional plates exceed that predicted by the correlation. If frequency is hypothetically taken to correspond to eddy structure size (i.e., a qualitative application of Taylor's hypothesis³⁹), then this result indicates that frequency spectrum, and hence the structure size distribution, depends on the roughness topology. This result is consistent with the statistical properties described above.

The scaled power spectral results are presented in Figs. 17 and 18. Figure 17a shows the smooth and 20 Grit plate results for each of the three boundary layer locations with inner scaling, where the mass flux power is scaled by the product squared of the friction velocity and the wall density, and the frequency is converted to a wave number and multiplied by the y-location within the boundary layer. This plot demonstrated that the scaled spectra shifted up and to the right with increasing roughness for all three boundary layer locations. The additional plate results fill the space between the curves. The trace also showed that the sensors resolved frequencies into Overlap Region II [i.e., the inertial

sub-range (slope of $-5/3$)]. Figure 17b shows the scaled power spectra with outer frequency scaling (i.e., the wave number multiplied by the boundary layer thickness). These results also show the up and right shift with roughness, and the curves for a given roughness overlap for high wave numbers. The spectral results converted into velocity fluctuations using the strong Reynolds analogy,¹⁸ scaled for compressibility and plotted with outer frequency scaling in Fig. 17c. For a given rough wall, this scaling collapsed the three boundary layer curves over a large range of frequencies. At the low frequencies, the collapsing broke down. The smooth plate results did not scale as well, where the $y/\delta_M = 0.75$ data fell significantly below the $y/\delta_M = 0.25$ and 0.5 traces; this downward shift was expected.⁷ The power spectral results for all six surfaces, with inner scaling, are shown in Figs. 18a-c for the three boundary layer locations. For $k_1 y < 1$, the $y/\delta_M = 0.25$ data (Fig. 18a) collapse reasonably well; this collapsing degrades moving away from the wall (Figs. 18b and c). At all three locations within the boundary layer, the curves shift to the left with increasing k_s for $k_1 \delta_M > 1$; this effect is most profound at $y/\delta_M = 0.75$.

Autocorrelation information was calculated from the normal-film probe time history data. Overall, the present correlation data agree with the expected trend where $R_E(\tau)$ decreases with increasing τ . All of the traces reached zero around $\tau \sim 100 - 200 \mu s$ depending on the roughness and boundary layer location, with an expected level of noise (~ 0.04). The plots shown in Figs 7a-c were limited to $50 \mu s$ to better show the details of the trace. The large τ trends are integrated into the discussion below and the integral-scales are discussed in the next section.

Since turbulent flow is characterized by a large range of spatial scales, the rate at which the Eulerian time-correlation coefficient drops as τ increases from zero gives an indication of the size of the smallest flow structures. The length of time it takes for $R_E(0)$ to reach zero is an indication of the size of the largest flow structures. A trend noticed from Fig. 19 is that the lower boundary layer position ($y/\delta_M = 0.25$, Fig. 7a) had the smallest rate of time-correlation decrease for all models, indicating that the small-scale structures were largest in the near wall region. This trend was echoed in the power spectra data, which showed for the lower region, the power was distributed toward lower frequency structures (it is assumed here that low frequency corresponds to large-scale structures). This result is consistent with the higher viscosity (due to the larger wall temperature) nearer to the wall dissipating the smaller eddies. For the smooth plate, $y/\delta_M = 0.50$ and $y/\delta_M = 0.75$ correlations had nearly identical autocorrelation time traces, with the only noticeable differences appearing at larger time offsets ($\sim 35 \mu s$). This indicates that the small-scale structures for the two regions were approximately the same; however, the large-scale structures were larger for the outer region of the boundary layer. For the rough surface models, the $y/\delta_M = 0.50$ data showed a smaller rate of decrease than at $y/\delta_M = 0.75$ indicating that the small-scale structure size was largest in the lower point, and decreased moving away from the wall toward the freestream. The autocorrelation time traces at larger time offsets were also different for each boundary layer region, and the results indicated that the large-scale structure size was largest in the outer region and decreased moving toward the wall from the freestream.

To better quantify how surface roughness affected the flow structure sizes, the micro-scale and integral-scale time values for each model were calculated³⁹ and are shown Figs.

20a and b, respectively. Typically Taylor's hypothesis,³⁹ which assumes that the turbulent structures are convected at the mean streamwise velocity, is used to present autocorrelation structure scales as lengths; however, this only works well for low turbulence levels (<1%).³⁹ For this reason, the micro-scale and integral-scale lengths are presented in time coordinates. Qualitative inference to the structure size was inferred from the temporal scales.

The micro-scale values are determined by fitting an osculating parabola to the autocorrelation time trace and determining the x-axis intercept of the parabola. Trends regarding the boundary layer region and surface roughness are apparent in these data. First, the micro-scales were largest at $y/\delta_M = 0.75$, and the trend across all of the models was that the micro-scale decreased as the wall was approached from the freestream. Second, these data showed that the micro-scale increased with increasing surface roughness height. The largest rate of increase was in the near wall region with a decreasing rate toward the freestream. This indicated that surface roughness increased the size of the smallest flow structures (given by the micro-scale), with the largest increase occurring in the near wall region.

Comparing the machined plate results (open symbols in Fig. 20a), it is clear that overall the equivalent sand grain height was effective in capturing the overall trend, however a topology dependence was discernable. In other words, the machined plate results were near the sand paper plate trends, however the rate of increase between the machined plates was significantly different than the trend. As discussed above, the two-dimensional plate produced a cavity type flow that shed structures that should have been

strongly correlated in the x-direction; this finding is consistent with the present higher correlation as compared to the sand grain and three-dimensional plates.

The integral length scale represents the magnitude of the large-scale structures in a turbulent flow. The data in Fig. 20b indicate that the large-scale flow structures decreased as the wall was approached from the freestream, which is consistent with the idea that the wall dampens or limits the large-scale structure sizes. Surface roughness decreased the integral length scale in all three boundary layer regions. The rate at which increasing surface roughness height decreased the integral length scale was largest in the outer region, and decreased as the wall was approached. At $y/\delta_M = 0.25$ and 0.5 , the rough wall integral scales showed a very modest decrease as compared to the difference in the smooth plate results. At $y/\delta_M = 0.75$, the decrease was more pronounced amongst the rough wall models at the lower k_s^+ values. Also, the integral scale was nominally independent of the location in the boundary layer for the larger roughness heights. For $k_s^+ > 240$, the integral time scale was nominally $75 \mu s$. Consistent with this trend was the comparison between the machined plates, which showed inconclusive results with respect to the integral length scale.

The cross-correlation of the two parallel-film sensors was used to give an indication of the flow structure angle [Eq. (4)]. For a flow structure or eddy with an angle of 90 degrees to the streamwise direction, the eddy reaches both parallel-film sensors at the same instant giving a cross-correlation peak at $\tau = 0$. For an eddy with an angle less than 90 degrees, the eddy reaches one of the film sensors before the other, shifting the time correlation peak to a higher time offset (increasing τ). Estimates of the flow structure angle can be found based on the probe sensor separation distance and the local mean

streamwise velocity. For all parallel probe measurements, the tunnel was operated at a stagnation pressure of $2.33 \cdot 10^5 \pm 0.3\%$ Pa and a stagnation temperature of 296 ± 1.0 K.

Figs. 21a-c shows cross-correlation time traces for each of the three boundary layer locations for all six plates. For all six models, the cross-correlation time trace peak drop-off rate is largest for the outer boundary layer region, followed by the middle, and then the lower region. Assuming the eddies are circular or elliptic and that the mean streamwise velocity of the eddies is significantly faster than the eddy rotational velocity, the drop-off rate gives an indication of the eddy streamwise thickness for eddies with a height of at least the parallel-film sensor separation distance. The drop-off rate shows that the small-scale eddy streamwise thickness was largest near the wall boundary and decreased moving toward the freestream. This result from the parallel-film cross-correlation agreed with the results found from the normal-film. The drop-off rate was found to decrease with increasing k_s , indicating surface roughness increased the small-scale streamwise thickness. These results also agreed with the normal-film autocorrelation results, which indicated that the effect of surface roughness was to increase the size of the smallest flow structures (given by the micro-scale) with the largest increase occurring in the near wall region.

The flow structure angles estimated from the cross-correlation traces are shown in Fig. 22 along with error bars indicating sampling rate resolution. The smooth plate result increased from 35 to 60 degrees as y/δ_M increased from 0.25 to 0.75. It appears that, with the exception of the two-dimensional plate and to within the measurement uncertainty, the smooth plate trend holds for the rough wall models. Unlike the other plates, the two-

dimensional plate flow structure angles remained relatively constant across the boundary layer at a value of approximately 40 degrees.

4.2 Subsonic Experimental Results

4.2.1 Mean Flow Measurements

The tunnel stagnation conditions, total temperature, T_o , and total pressure, P_o , were measured upstream of the test section in the stagnation chamber. The static pressure, P_s , was also measured inside the test section for each Mach number. The freestream Mach number was found by measuring the differential pressure, ΔP , using a differential pressure transducer. The measured reference conditions are summarized in Table 4. The velocity profiles for each Mach number and roughened surface were estimated using a Pitot pressure probe to measure the total pressure across the boundary layer. The velocity profiles estimated from the Pitot measurements can be seen in Fig. 23a. Velocity profiles for all six plates measured with the hot-film probes are also presented in Fig. 23b. The velocity profiles generated using both measurement techniques were in excellent agreement. The freestream velocities measured using the Pitot-probe and the hot-film probes also agreed to within 1.5%. The velocity profiles for both Mach numbers show a slight leftward shift with increasing roughness (i.e., C_f) as expected.

From the Pitot data and hot-film data, the boundary layer thickness, δ , momentum thickness, θ , displacement thickness, δ^* , and skin friction coefficient (discussed below), C_f , was calculated for the each plate, with the exception of the smooth plate, where the

direct measurement was used. The y – axis location at which $u/U_e = 98\%$ was taken to be the value of δ .

The skin friction values for the six plates were estimated using three different methods. The first estimate of the skin friction coefficient was found using the integral methods as described previously. The skin friction was also calculated using the velocity method described by Simpson et al.⁴¹ This method fits a line through the velocity profile data in the log-law region on the semi-log plot. The slope of this line multiplied by κ ($= .41$)¹⁵ gives the value of the friction velocity, u^* . With u^* known, the value of the skin friction coefficient can be solved for directly.

The skin friction coefficients for each rough plate and the smooth plate were also measured directly using skin friction gages designed to measure the shear stress at the surface of each plate. The skin friction gages were calibrated by applying a known force to the gage and recording the voltages produced from the strain gages in a half bridge configuration. The skin friction gages were designed using the principles of a cantilever beam to measure the force applied to the head of the gage. The force, F , applied to the cantilever beam is converted to the wall shear stress using the relation $\tau_w = F/A_H$, where A_H is the area of the head of the gage. The measured wall shear stress is found using the calibration curves. The skin friction coefficient is then calculated directly from the definition of C_f , $C_f = \tau_w / \frac{1}{2}\rho V^2$, where $\frac{1}{2}\rho V^2$ is the freestream dynamic pressure. A skin friction trace can be seen in Fig. 24. It was found that the alignment with the tunnel floor proved to be a crucial factor in achieving accurate results. As a result of the difficulty in aligning the roughness elements of the gages to the roughness elements of the tunnel

models, the accuracy of the direct measurements is estimated to be around 15%, which is much greater than the documented 6%.^{17,21}

The measured values of u^* used to calculate the skin friction values are presented in Table 5. The values found using the three different methods are in reasonable agreement with each other ($\cong 15\%$). The direct measurement is within the expected errors with a significant portion of the error resulting from alignment difficulties. The velocity profile results gave the best comparison to the accepted semi-empirical relations.

The velocity defect for each plate is presented in Fig. 25. The velocity defect with the friction velocity estimated with the velocity gradient method (discussed below) resulted in all of the data collapsing reasonably well onto a single curve. The agreement with the smooth plate theory is considered to be excellent. The deviations of the data from the theory are attributed to the uncertainties in the determination of δ and C_f . Presented in Fig. 26 are the law of the wall plots. The smooth plate data is in excellent agreement with the theory. The rough wall data show the expected shift down and to the right of the smooth plate. The equivalent sand grain roughness values along with the roughness parameters (k^+ and k_s^+) are listed in Table 2 for each surface at both Mach numbers. These values were calculated using the methods outlined in Schlichting,⁷ with the velocity gradient based skin friction values.

4.2.2 Turbulence Measurements

Two hot-film probes, a normal wire probe and a cross wire (x-y plane) probe, were used to take velocity and turbulence data across the boundary layer and in the freestream for all the surfaces at Mach 0.22. The freestream Mach number was found using the

differential pressure measurements and the methods previously described. The hot-film probes were calibrated by placing the probes in the freestream and varying the Mach numbers from 0.07 to 0.25. The velocities were then calculated from the Mach numbers and calibration curves for both the normal wire and cross wire hot-film probes were generated.

The normal wire probes were used to measure the velocities across the boundary layer for each rough plate and the smooth plate as stated previously. The normal wire probes were also used to provide the turbulence intensity values for the smooth and rough plates. The outer, inner and mixed variable scaled turbulence intensities are plotted in Fig. 27. The turbulence intensity results yield some interesting trends. First, it was noticed that, unlike the supersonic data, the subsonic data did not collapse with the smooth wall data in the outer region of the boundary layer as expected when scaled with the friction velocity. Instead, the turbulence intensity profiles demonstrated a dependence on roughness. The levels shown in Fig. 27 are consistent with the supersonic results.

The cross-film probes were used to measure the u and v velocity components across the boundary layer for each rough plate and the smooth plate at Mach 0.22. With the velocity components known, the total velocity, U , could be found from and compared to the velocities obtained from the Pitot and normal wire data. The cross-wire results with the various scaling are presented in Fig. 27. The same trends seen in the turbulence intensities from the normal wire data are also found in the cross-wire data. These results could be related to compressibility effects and will be examined further with the turbulence information obtained with the $M = 0.65$ case.

The kinematic Reynolds shear stress values were also calculated from the cross-film data and are shown in Fig. 28. Similar to the turbulence intensity values, the kinematic Reynolds shear stress values are presented with inner, outer, and mixed variable scaling. Two things are noticed when looking at the shear stress data. First, the outer variable scaling again does not collapse the data as was the case for the supersonic flow. Second, the Reynolds shear stress values with both inner and outer variable scaling are slightly lower than the supersonic case. These two trends suggest that the Reynolds shear stress has roughness and Mach number dependencies. Again, the Mach 0.65 turbulence data will be valuable to help sort out this issue. In addition, although the Mach number is low, the differences between the supersonic LDV data and the subsonic cross-wire data may be attributed to compressibility effects with the cross-wire probe. Recall that the supersonic cross-wire data demonstrated a strong roughness dependency that was absent from the LDV data.

4.3 Supersonic Numerical Results

Numerical simulations using an in-house cell-centered, finite volume, parabolized Navier-Stokes solver were performed by Latin.¹⁹ However, Fan⁴⁶ re-accomplished that work and further extended it by examining two additional rough wall models. Hence, to avoid duplication, the results from Fan's thesis are discussed here. In addition, Fan also investigated the two subsonic conditions, however comparisons with the experimental data have not been performed. Pritchett⁴⁷ is in the process of re-accomplishing those results with the exact experimental test conditions as part of his thesis work. Hence, this section focuses on the supersonic test condition.

The predicted boundary layer height, momentum thickness and skin friction coefficient for all six plates from each of the three turbulence models are listed in Table 6. From an examination of the numerical results, it can be seen that with increasing roughness height, the boundary layer thickness increased accordingly due to additional turbulence mixing and entrainment of freestream fluid, as did the experimental data. The predicted integral properties for the smooth plate (Table 6) were all within nominally 5.0% of the experimental data. Interestingly for the rough-wall predictions, each of the three models performed well on a different integral parameter. For example, the Kragstad model produced the largest skin friction coefficients, which were still less than the experimental data by nominally 6.0%. However, the van Driest model produced the better boundary layer thickness predictions (within 6.5%), where the Cebeci-Chang formulation produced better momentum thickness predictions (within 4.0%). The differences between the models were significant, where some predicted quantities were 25% apart.

The skin friction coefficients for a representative sample of the results consisting of the smooth plate, 80 grit plate (smallest roughness) and the 20 grit plate (largest roughness) versus local Reynolds number are shown in Fig. 29. The trends for the remaining three plates were very similar to those shown in Fig. 29. For the smooth plate, the skin friction coefficient decreased with local Reynolds number smoothly. On the other hand, for the rough plates, the skin friction coefficients arose abruptly at the starting point of roughness, then decreased with Reynolds number. Only the Cebeci-Chang model gave a smooth reduction, the other two showed oscillations at the point where the roughness was "turned on." The magnitude of the oscillations depended on the

roughness geometry, where the smaller roughness Reynolds numbers produced smaller oscillations.

Representative numerical velocity profiles for the smooth, 80 Grit and 20 Grit plates are plotted in Fig. 30. Again, the results for the remaining three plates are very similar to those shown in Fig. 30. As the results indicated, all three models produced similar profiles that were in good agreement with the experimental data. Shown in Fig. 31 are the velocity profiles for all six plates plotted with defect law^{1,30,39} scaling. The collapsing of the defect law profiles was the expected result based on the low-speed database^{1,30,39} and the high-speed presented earlier (shown on Fig 31). The agreement between the present predictions and the experimental data was considered very good.

The law of the wall plots for the smooth, 80 Grit and 20 Grit plates, with van Driest scaling, are shown in Fig. 32. The predicted profile for the smooth plate is in excellent agreement with both flat plate theory and the experimental data. For the rough plates, the numerical profiles deviated from the smooth plate theory leading to the velocity shift as expected for the rough-walls. The predicted velocity profiles agreed very well with the experimental data in the outer region. The differences between the three models became more significant in the inner region ($y^+ < 100$). However, experimental data were not available in this region for comparison.

The mean density profiles are shown in Fig. 33. The numerical results are compared to two estimates of the density obtained from the experimental data. The Crocco-Buseman integral^{30,33} was used for one estimate, and assuming a locally isentropic flow was used for the other. For the smooth and rough plates, the calculations were all in good agreement with experimental data.

The turbulence shear stress profiles for the smooth, 80 Grit and 20 Grit plates, normalized by the local mean velocity, are plotted in Fig. 34. The predicted Reynolds shear stresses from all three turbulence models for all six plates matched the LDV data very well, demonstrating that the Reynolds shear stress was well modeled by each formulation. As was the case for the experimental data, the numerical shear stress profiles in the outer region were all independent of the roughness Reynolds number for the outer scaling used in Fig. 34. For the roughest case, the van Driest model produced slightly better agreement with the experimental data, when compared to the other two.

Chapter 5

Conclusions and Recommendations

5.1 Conclusions

An experimental study of the influence of surface roughness on the mean and turbulent flow properties of a high-speed ($M = 0.22 - 2.8$, $Re/m = 2.0-2.5 \times 10^7$) turbulent boundary layer flow was performed. Six wall topologies including a smooth and five rough surfaces consisting of three random sand-grain plates ($k_s^+ = 100, 400, 570$) and two uniformly machined plates ($k = 0.56$ mm for both) were tested. The experimental measurement techniques included a conventional Pitot pressure probe, laser Doppler velocimetry, hot-wire anemometry, and color schlieren photography. Mean flow measurements included detailed surveys of the velocity and density. The turbulent flow profiles included direct measurements of the kinematic velocity turbulence intensities, mass flux turbulence intensities, the kinematic Reynolds shear stress, the compressible Reynolds shear stress and the density-velocity fluctuation correlation. In general, the results of this study describe the influence of roughness on the magnitude and scaling of the mean and turbulent statistical flow properties across the supersonic boundary layers. Specific conclusions for each phase of the program are listed below.

5.1.1 Supersonic Experimental Study

For the supersonic test condition, the roughness elements were observed to protrude into the supersonic portion of the boundary layer, and the corresponding shock and expansion waves distorted the boundary edge and interacted with the boundary layer turbulence. The trends in the mean flow, observed for incompressible rough wall flow, were found to hold for the present study when Van Driest II scaling was used.

In general, the rough wall kinematic statistical turbulent flow properties measured with the laser Doppler velocimetry system, collapsed on to a single curve when scaled with outer flow variables. The only exception was the 2-D plate, and it was expected that the turbulence production mechanisms associated with the d-type cavity were significantly different than for the remaining plates, which all had 3-D roughness patterns. Roughness was found to extend the region of inner scaling applicability for the kinematic properties further out into the boundary layer. Turbulent flow statistical properties with the explicit thermodynamic dependence did not collapse when scaled by local mean quantities, and increased almost linearly with k_s^+ . Relative to the smooth plate results, the (ρw) turbulence intensity component showed the largest rate increase with roughness, followed by the (ρu) - and then the (ρv) -component. In terms of second order correlations, the x - z component of the full compressible Reynolds shear stress increased at the fastest rate, followed by transverse-velocity-density correlation, and then the x - y component of the compressible Reynolds shear stress. When scaled by inner flow variables, the rough wall axial mass flux turbulence intensity, the x - y component of the compressible Reynolds shear stress, and the transverse component of the turbulent apparent mass flux data collapsed for the inner 70% of the boundary layer. It was shown

that the influence of smaller roughness elements increased the skin frictional losses more than the boundary layer turbulence levels. However, as the roughness height was increased, the turbulence production relative to the frictional losses increased.

Increasing surface roughness equivalent sand grain height had the effects of increasing the power spectra and the power spectra difference between the three boundary layer regions ($y/\delta = 0.25, 0.5, \text{ and } 0.75$), and shifted the turbulent energy toward the lower frequencies in the near wall region. The spectra measurements confirmed the Overlap II Region (inertial subrange) for all of the plates tested at each measurement location. Surface roughness was found to increase the size of the small-scale structures (the increase was nearly linear with the k_s^+). The size of the large-scale structures was found to decrease with roughness height, and for very large roughnesses ($k_s^+ \geq 240$), the integral scale approached the same value ($75 \mu s$) across the entire boundary layer. The turbulent flow structure angles were smallest near the wall (lower region) and increased toward the boundary layer edge. Lastly, the two-dimensional plate cavity eddy production mechanism produced structures that had higher axial correlation than the trends for the sand grain plates indicated.

In summary, all of the quantitative data presented above indicated that roughness had the effect of populating the boundary layer with higher energy eddies (i.e., fluctuating levels) that were distributed over narrower range of length scales, as compared to the smooth plate. Hence, the roughness elements had the effect of altering the turbulence production and transport mechanisms across the entire boundary layer, as compared to the smooth plate. In addition, the presence of the Overlap regions indicated that the expected energy cascade and dissipation mechanisms^{7,19,23} were present for the rough

wall flows. These findings have important implications for both Reynolds averaged and Large-Eddy simulation techniques.

Lastly, in all of the data, the equivalent sand-grain roughness was found to be an effective parameter to characterize the overall effects of roughness on the turbulent flow properties (i.e., clear trends with k_s^+ were discernible). The machined 2-D and 3-D plate results were in reasonable agreement with the sand-grain trends, however significant variances (up to 25%) were observed and were related back to roughness topology. Hence, although effective, the equivalent sand grain parameter did not capture all of the roughness topology effects on the turbulence production.

5.1.2 Subsonic Test Condition

The subsonic test portion of the study was not as complete as that for the supersonic test condition. The primary reason was that the particle image velocimetry system proved to be inadequate for turbulence measurements. The PI is in the process of installing a laser Doppler velocimetry system to overcome this shortfall. However, a rather extensive investigation of the $M = 0.22$ test condition was performed with hot/cross-film anemometry, and the $M = 0.65$ mean flow was well documented with the Pitot probe. A summary of the findings with comparisons to the supersonic data is given below.

The velocity profile, velocity defect, and law wall data all behaved as anticipated. The law wall plots taken from the roughness data for both the compressible and incompressible cases shifted down and to the right of the smooth plate data with increasing skin friction, while the smooth plate data for both cases was found to be in

excellent agreement with the law wall theory. The velocity defect for both cases, when scaled by the friction velocity, collapsed very well onto a single curve with the only deviations attributed to the uncertainties of the boundary layer heights and the skin friction values.

The three methods used to predict the skin friction coefficients were found to be in agreement to within 20%. Though high, this falls within the expected uncertainties of obtaining skin friction. It was found that the velocity profile method results gave the best comparison to the accepted semi-empirical relations. It was also found that alignment of the skin friction gages for direct measurement proved to be a very critical factor in the accuracy of the results.

The turbulence information obtained from the hot-film anemometry data yielded some unexpected results. It was found that the turbulence intensities for the incompressible subsonic case showed a dependence on roughness that was not apparent for the supersonic case. It was also found that the Reynolds shear stress not only showed the same roughness dependence, but a possible Mach number dependence as well. It is acknowledged that more work needs to be completed to support these conclusions.

5.1.3 Supersonic Numerical Study

The principal objective of the present study was to investigate the applicability of current low-speed rough-wall turbulence models for high-speed flow. Three algebraic rough-wall turbulence models (van Driest, Kragstad and Cebeci-Chang) were tested. All three are founded in modifying the mixing length van Driest damping function to produce the correct velocity shift and skin friction coefficient. The models were evaluated against

mean flow and turbulent shear stress data at Mach 2.7. In summary, all three model produced mean, integral and turbulence results that agreed well with the experimental data. The largest difference between the models occurred in the near wall region, where experimental data was not available.

5.2 Recommendations

The goal of this work was to provide a better understanding of the effects of compressibility on the rough wall turbulent boundary layers. The first step in the process was a comprehensive supersonic experimental program that provided a very in-depth analysis of the effects of roughness on supersonic turbulent boundary layers. The second step was to provide a similar analysis for two subsonic conditions [incompressible ($M = 0.22$) and compressible ($M = 0.65$)]. This part of the study was hindered by the lack of an LDV system. Hence, the first recommendation is to complete the subsonic experiments with an LDV system. This effort is currently underway. At the time of this writing, the laser had been purchased, and the university was in the process of supplying the correct power to lab. The AFRL propulsion directorate has agreed to loan the PI a two-component LDV system to complete this work. With these data, more complete analysis of the influence of compressibility on the boundary layer properties will be performed.

Beyond the scope of this work, and based on the PI's previous investigation of streamline curvature driven pressure gradients,²² it is recommended that the test matrix be expanded to include wall curvature effects. This effort should be directed at providing flow field insight suitable for second order turbulent transport modeling. This

recommendation is based on the PI's experience with wall curvature and the associated complicated impact on the turbulent shear stress, and as indicated in Ref. [48], algebraic and two-equation models cannot capture the essential dynamics without very crude empirical corrections. Furthermore, to obtain reasonable comparisons, the experimental data must be acquired in "shear layer coordinates," defined as the average between the upstream freestream and the wall directions. This was deemed necessary because the models' inaccurate predictions of the normal stresses prohibited transformation of the numerical results, and in the body intrinsic system, the shear stress values could be negative, which cannot be predicted by eddy viscosity type models. Lastly, large-eddy simulation of wall bounded flows is more prohibitive than originally believed. Hence, the RANS approach will be prevalent in the near to distant future (~ 20 to 100 years). In summary, to provide realistic simulation for a long list of practical Air Force applications (e.g., thermal protection for access to space, turbomachinery, inlets and nozzles, and scramjet combustors) fundamental and detailed studies such as that provided in this study are required over a broader range of conditions, and surface curvature is a reasonable next step.

References

- ¹Schlichting, H., *Boundary Layer Theory*, Mechanical Engineering, McGraw-Hill Book Inc., 1955.
- ²Wilcox, D., *Turbulence Modeling for CFD*, DCW Industries, Inc., 1993.
- ³Fernholz, I., Finley, M., and Mikulla, V., "A Further Compilation of Compressible Boundary Layer Data with a Survey of Turbulence Data," AGARDograph No. 263, NATO, Technical Editing and Reproduction Ltd, London, England, Nov. 1981.
- ⁴Nikuradse, J. "Stromungsgesetze in Rauhen Rohren," *Forschg.-Arb. Ing.-Wesen*, 1933.
- ⁵Simpson, R., "A Generalized Correlation of Roughness Density Effects on the Turbulent Boundary Layer," *AIAA Journal*, Vol. 11 No. 2, Feb. 1973, pp. 242-244.
- ⁶Antonia, R. A. and Wood, D. H. "Calculation of a Turbulent Boundary Layer Downstream of a Small Step Change in Surface Roughness," *Aeronautical Quarterly*, Aug. 1975, pp. 202-210.
- ⁷Perry, A. E., Lim, K. L., and Henbest, S. M., "An Experimental Study of the Turbulent Structure in Smooth- and Rough-Wall Boundary Layers," *Journal of Fluid Mechanics*, Vol. 177, pp. 437-466.
- ⁸Corrisin, S. and Kistler, A., "Free-Stream Boundaries of Turbulent Flow," NACA Report 1244, 1955.
- ⁹Dussauge, J-P., Smith, R., Smits, A., Fernholtz, H., Finley, P., and Spina, E., "Turbulent Boundary Layers in Subsonic and Supersonic Flow," AGARDograph No. 335, NATO, Canada Communications Group, Hull (Quebec) Canada, July 1996.

- ¹⁰Goddard, F., "Effects of Uniformly Distributed Roughness on Turbulent Skin-Friction Drag at Supersonic Speeds," *J. Aero/Space Sciences*, Vol. 26 No. 1, 1959, pp. 1-24.
- ¹¹Berg, D., "Surface Roughness Effect on a Mach 6 Turbulent Boundary Layer," *AIAA Journal*, Vol. 17, No. 9, 1979, pp. 929-930.
- ¹²Reda, D., Ketter, F., and Fan, C., "Compressible Turbulent Skin Friction on Rough and Rough/Wavy Walls in Adiabatic Flow," *AIAA Journal*, Vol. 13, 1975, pp. 553-555.
- ¹³Van Driest, E., "Turbulent Boundary Layers in Compressible Fluids," *J. Aeronautical Sciences*, Vol. 26, No. 3, 1951, pp. 287-319.
- ¹⁴Liepmann, H. and Goddard, F., "Note on Mach Number Effect Upon the Skin Friction of Rough Surfaces," *J. Aero/Space Sciences*, Vol. 24, No. 10, 1957, pp. 784.
- ¹⁵Morkovin, M., "Effects of Compressibility on Turbulent Flows," *The Mechanics of Turbulence* edited by A. Favre, New York: Gordon and Breach, 1961, pp. 368-380.
- ¹⁶Smits, A. J., Spina, E. F., Alving, A. E., Smith, R. W., Fernando, E. M., and Donovan, J. F. "A Comparison of the Turbulence Structure of Subsonic and Supersonic Boundary Layers," *Physics of Fluids*, A Vol. 1 No. 11, 1989, pp. 1865-1875.
- ¹⁷Spina, E., Smits, A., and Robinson, S. "The Physics of Supersonic Turbulent Boundary Layers," *Annual Review of Fluid Mechanics*, Vol. 26, 1994, pp. 287-319.
- ¹⁸Smits, A. and Dussauge, J-P., *Turbulent Shear Layers in Supersonic Flow*, American Institute of Physics, Woodbury New York, 1996.
- ¹⁹Latin, R. M. *The Influence of Surface Roughness on Supersonic High Reynolds Number Turbulent Boundary Layer Flow*, AFIT/DS/ENY/98M-02, PhD dissertation, Air Force Institute of Technology, April 1998.

- ²⁰Hale, C., "Experimental Investigation of a Supersonic Turbulent Boundary Layer with Adverse Pressure Gradient," MS Thesis, AFIT/GAE/ENY/95D-12, Dec., 1995.
- ²¹Luker, J., Hale, C., and Bowersox, R., "Experimental Characterization of the Turbulent Shear Stresses for Distorted Supersonic Boundary Layers," *Journal of Propulsion and Power*, Vol. 14, No. 1, 1998, pp. 110-118.
- ²²Luker, J., Bowersox, R., Buter, T., "Influence of A Curvature Driven Favorable Pressure Gradient on a Supersonic Turbulent Boundary Layer," *AIAA Journal*, Vol. 38, No. 8, 2000, pp. 1351-1359.
- ²³Bowersox, R., "Combined Laser Doppler Velocimetry and Cross-Wire Anemometry Analysis," *AIAA Journal*, Vol. 34, No. 11, 1996, pp. 2269-2275.
- ²⁴Smith, D. and Smits, A., "A Study of the Effects of Curvature and Compression on the Behavior of a Supersonic Turbulent Boundary Layer," *Experiments in Fluids*, Vol. 18, 1995, pp. 363-369.
- ²⁵Hazelton, D., Bowersox, R., Nuemann, D., and Hayes, J., "Skin Friction Measurements in a Mach 6 Inlet Test," AIAA-97-2884, 33rd AIAA/ASME/SAE/ASEE Joint Propulsion Conference, Seattle WA, July 6-9, 1997.
- ²⁶Holman, J. P., *Experimental Methods for Engineers*, 3rd Ed., McGraw-Hill, New York, 1978.
- ²⁷Durst, F., Melling, A., and Whitelaw, J., *Principles and Practice of Laser-Doppler Anemometry*, Academic Press, New York, 1981.
- ²⁸Adrian, R., "Laser Velocimetry," *Fluid Mechanics Measurements*, 2nd Ed., Edited by R. Goldstein, Taylor & Francis, Washington DC, 1996, pp. 175-293.

- ²⁹Fiore, A. W. "Experimental Data For Compressible Turbulent Flow," Air Force Wright Aeronautical Laboratories, WPAFB, OH, June 1983.
- ³⁰Schetz, J., *Boundary Layer Analysis*, Prentice Hall, 1993.
- ³¹Hopkins, E., and Inouye, M., "An Evaluation of Theories for Predicting Turbulent Skin Friction and Heat Transfer on Plates at Supersonic and Hypersonic Mach Numbers," *AIAA Journal*, Vol. 9, No. 6, pp. 993-1003.
- ³²White, Frank M. *Viscous Fluid Flow* (Second Edition). McGraw-Hill, Inc., 1991.
- ³³Hinze, O., *Turbulence*, McGraw-Hill, New York, 1975.
- ³⁴Klebanoff, P. S., "Characteristics of Turbulence in a Boundary Layer with Zero Pressure Gradient," Report 1247, National Committee for Aeronautics (and NASA TN 3178), May 1954.
- ³⁵Elena, M. and LaCharme, J.-P., "Experimental Study of a Supersonic Turbulent Boundary Layer Using a Laser Doppler Anemometer," *Journal of Theoretical and Applied Mechanics*, Vol. 7, No. 2, 1988, pp. 175-190.
- ³⁶Heller, H. and Bliss, D., "Aerodynamically Induced Pressure Oscillations in Cavities - Physical Mechanisms and Suppression Concepts," AFFDL-TR-74-133, Air Force Flight Dynamics Laboratory, Wright-Patterson Air Force Base, OH, February 1975.
- ³⁷Miller, R., Dotter, J., Bowersox, R., and Buter, T., "Measurements of Compressible Turbulence in a Supersonic Wall Bounded Flow with Pressure Gradient," *2nd Symposium on Transitional and Turbulent Compressible Flows*, Joint ASME/JSME Fluids Engineering Conference, Hilton Head SC, FED-Vol. 224, 1995, pp. 193-200.
- ³⁸Bendat, J. and Piersol, A., *Random Data Analysis and Measurement Procedures*, 2nd Ed. (Revised and Expanded), John-Wiley & Sons, 1986.

- ³⁹Cebeci, Tuncer and Smith, A. M. O. *Analysis of Turbulent Boundary Layers*. Applied Mathematics and Mechanics, Academic Press, 1974.
- ⁴⁰Shames, I., *Mechanics of Fluids*, 2nd Ed., McGraw-Hill, 1982.
- ⁴¹Simpson, Roger L. and George, Jacob, "Some Effects of Sparsely Distributed Three-Dimensional Roughness Elements on Two-Dimensional Turbulent Boundary Layers" *AIAA 2000-0915, 38th Aerospace Sciences Meeting and Exhibit*, January 10-13, 2000, Reno, NV
- ⁴²Dvorak, F.A., "Calculation of Turbulent Boundary Layers on Rough Surfaces in Pressure Gradient." *AIAA Journal* Vol.7, No.9, 1969, pp. 1752-1759.
- ⁴³Cebeci, T. and Chang, K.C. "Calculation of Incompressible Rough-Wall Boundary-Layer Flows," *AIAA Journal* Vol. 16, No.7, 1978, pp. 730-735.
- ⁴⁴Kragstad, P., "Modification of the van Driest Damping Function to Include the Effects of Surface Roughness," *AIAA Journal* Vol.29, No. 6, 1990, pp. 888-894.
- ⁴⁵Anderson, D. A., J. C. Tannehill, and R.H. Pletcher, *Computational Fluid Mechanics and Heat Transfer*, Hemisphere, New York, 1984.
- ⁴⁶Fan, H., *Numerical Analysis and Turbulence Modeling of High-Speed Turbulent Flows Over Rough Surfaces*, MS Thesis, Department of Aerospace Engineering and Mechanics, The University of Alabama, 1998.
- ⁴⁷Pritchett, V., *Experimental and Numerical Investigation of Subsonic Compressible Rough Wall Flow*, Thesis in Progress, Department of Aerospace Engineering and Mechanics, The University of Alabama, 2001.
- ⁴⁸Johnson, D., Menter, F. and Rumsey, C., "The Status of Turbulence Modeling for External Aerodynamics," *AIAA-94-2226*, June 1994.

Tables

Table 1a. Supersonic Measurement Flow Conditions

Measurement	P_t (Pa)	T_t (K)	Re/m ($\cdot 10^7$)
Pitot	$2.17 \cdot 10^5 \pm 0.4\%$	296 ± 1.0	1.9 ± 0.3
Cross-Film (x-y Plane)	$2.22 \cdot 10^5 \pm 0.3\%$	293 ± 1.0	2.0 ± 0.3
Cross-Film (x-z Plane)	$2.39 \cdot 10^5 \pm 0.3\%$	296 ± 1.0	2.1 ± 0.3
Laser Doppler	$2.41 \cdot 10^5 \pm 0.5\%$	294 ± 1.0	2.1 ± 0.3
Color Schlieren	$2.17 \cdot 10^5 \pm 0.4\%$	296 ± 1.0	1.9 ± 0.3

Table 1b. Subsonic Measurement Flow Conditions

Measurement	P_t (Pa)	T_t (K)	Re/m ($\cdot 10^7$)
Pitot, $M = 0.22$	$4.34 \cdot 10^5 \pm 0.5\%$	299 ± 1.0	2.2 ± 0.3
Pitot, $M = 0.65$	$1.51 \cdot 10^5 \pm 0.5\%$	298 ± 1.0	2.6 ± 0.3
Hot-Film, $M = 0.22$	$4.48 \cdot 10^5 \pm 0.5\%$	297 ± 1.0	2.3 ± 0.3
Cross-Film, $M = 0.22$	$4.46 \cdot 10^5 \pm 0.5\%$	298 ± 1.0	2.2 ± 0.3
Skin Friction, $M = 0.22$	$4.37 \cdot 10^5 \pm 0.5\%$	294 ± 1.0	2.2 ± 0.3
Skin Friction, $M = 0.65$	$1.50 \cdot 10^5 \pm 0.5\%$	297 ± 1.0	2.5 ± 0.3

Table 2a. Supersonic Surface Conditions

Model	\bar{k} (mm)	$\sqrt{k'^2}^a$ (mm)	k_{max}^a (mm)	T_w^b (K)	ρ_w^b (kg/m ³)	k_s^c (mm)	k_s^{+c}	A_B (mm ²)
Flat	0.007	0.005	0.02	276.	0.11	0.00	0.	0.0
2-D	0.56	0.007	0.58	274.	0.12	1.09	289.	35.6
3-D	0.56	0.007	0.58	273.	0.12	0.91	241.	9.1
80 Grit	0.53	0.17	1.10	273.	0.12	0.44	104.	33.7
36 Grit	0.90	0.34	1.40	273.	0.12	1.42	395.	57.2
20 Grit	0.83	0.50	1.70	273.	0.12	1.98	571.	52.7

Table 2b. M = 0.22 Surface Conditions

Model	\bar{k} (mm)	$\sqrt{k'^2}^a$ (mm)	k_{max}^a (mm)	T_w^b (K)	ρ_w^b (kg/m ³)	k_s^c (mm)	k_s^{+c}	A_B (mm ²)
Flat	0.007	0.005	0.02				0.	0.0
2-D	0.56	0.007	0.58				501	35.6
3-D	0.56	0.007	0.58				269	9.1
80 Grit	0.53	0.17	1.10				168	33.7
36 Grit	0.90	0.34	1.40				479	57.2
20 Grit	0.83	0.50	1.70				443	52.7

Table 2c. M = 0.65 Surface Conditions

Model	\bar{k} (mm)	$\sqrt{k'^2}^a$ (mm)	k_{max}^a (mm)	T_w^b (K)	ρ_w^b (kg/m ³)	k_s^c (mm)	k_s^{+c}	A_B (mm ²)
Flat	0.007	0.005	0.02				0.	0.0
2-D	0.56	0.007	0.58				552	35.6
3-D	0.56	0.007	0.58				166	9.1
80 Grit	0.53	0.17	1.10				180	33.7
36 Grit	0.90	0.34	1.40				386	57.2
20 Grit	0.83	0.50	1.70				322	52.7

^aFor the 2-D and 3-D plates, the standard deviation was taken as 1/3 the machining accuracy (22.4 μ m), ^bAdiabatic wall temperature, ^c $k_s = 0$ by definition ($k^+ \approx 1.1$.)

Table 3. Measurement Uncertainty

Measurement	Uncertainty		
x, y (mm)	0.25, 0.13		
δ_i, δ (mm)	1.0, 2.5		
δ^* (mm)	0.08		
θ_i, θ (mm)	0.04, 0.02		
$C_{f,0}, C_f (\cdot 10^{-4})$	1.0, 2.0		
$M_e (\cdot 10^{-2})^b$	1.4		
$y/\delta^a \Rightarrow$	0.2	0.5	1.0
$\bar{u}/u_e (\cdot 10^{-2})^b$	1.3	1.4	1.3
$\sqrt{u'^2}/\bar{u} (\cdot 10^{-3})$	2.1	1.9	1.5
$\sqrt{v'^2}/\bar{u} (\cdot 10^{-3})$	0.8	1.1	1.1
$\overline{u'v'}/\bar{u}^2 (\cdot 10^{-4})$	0.7	2.9	0.4
$\bar{\rho u}/\rho_e u_e (\cdot 10^{-2})$	2.9	3.3	3.6
$\sqrt{(\rho u)' ^2}/\bar{\rho u} (\cdot 10^{-3})$	6.0	7.0	2.0
$\sqrt{(\rho v)' ^2}/\bar{\rho u} (\cdot 10^{-3})$	5.0	4.0	3.0
$\sqrt{(\rho w)' ^2}/\bar{\rho u} (\cdot 10^{-3})$	5.0	3.5	2.5
$(\rho u)'(\rho v)' / \bar{\rho u}^2 (\cdot 10^{-4})$	4.2	4.3	1.1
$(\rho u)'(\rho w)' / \bar{\rho u}^2 (\cdot 10^{-4})$	4.2	4.3	1.1
$\bar{\rho}/\rho_e (\cdot 10^{-2})$	3.2	3.6	3.8
$\overline{\rho' v'}/\bar{\rho} \bar{u} (\cdot 10^{-4})$	4.3	5.2	1.2

^aErrors in Units Plotted (Based on Smooth Plate Results)^bPitot Probe, ^cLaser Doppler Velocimetry, and Hot-Wire Anemometry

Table 4a. Supersonic Reference Values ($x = 54$ cm)

Model	M_e	δ (mm)	δ_M (mm)	δ^* (mm)	θ (mm)	B'	C_f	u^* (m/s)	Δx_o (cm)	Re_x ($\cdot 10^7$)	Re_θ ($\cdot 10^4$)
Flat	2.75	12.4	15.4	3.32	0.80	N/A	0.00159	26.	27.5	1.6 ± 0.8	1.6
2D	2.73	16.8	18.1	5.82	1.32	21.4	0.00363	38.	7.9	1.2 ± 0.6	2.6
3D	2.73	15.8	17.3	5.67	1.29	21.8	0.00353	38.	8.1	1.2 ± 0.6	2.6
80 Grit	2.73	14.7	16.3	4.77	1.11	23.9	0.00302	35.	9.2	1.2 ± 0.6	2.2
36 Grit	2.72	18.0	19.2	6.24	1.43	21.4	0.00393	40.	8.0	1.2 ± 0.6	2.9
20 Grit	2.70	17.7	18.2	6.26	1.45	21.0	0.00399	40.	7.7	1.2 ± 0.6	2.9

^aDefined such that $u/u_e = 0.99$, ^bDefined such that $M/M_e = 0.99$

Table 4b. Subsonic Reference Values

Surface	M_e	δ (mm)	θ_i (mm)	θ_r (mm)	τ_w (Pa)	Re/m (10^6)	$Re\theta$ (10^3)
Flat Plate	0.22	14.8	0.22	1.43	37.1	22.3	32.0
2D Plate	0.23	17.5	0.21	2.27	151	22.2	50.6
3D Plate	0.23	16.6	0.15	2.23	132	22.5	50.3
80 Grit Plate	0.23	16.0	0.19	1.72	117	22.9	39.3
36 Grit Plate	0.23	16.1	0.36	2.01	155	22.2	44.8
20 Grit Plate	0.24	18.3	0.24	2.31	150	22.9	53.0

Surface	M_e	δ (mm)	θ_i (mm)	θ_r (mm)	τ_w (Pa)	Re/m (10^6)	$Re\theta$ (10^3)
Flat Plate	0.65	7.69	0.22	1.04	112	25.5	26.5
2D Plate	0.67	12.5	0.21	2.18	443	25.5	55.9
3D Plate	0.66	10.6	0.15	1.85	335	25.4	47.1
80 Grit Plate	0.67	10.9	0.19	1.75	350	25.1	44.1
36 Grit Plate	0.68	12.2	0.36	2.09	449	26.0	54.6
20 Grit Plate	0.69	12.2	0.24	2.20	417	26.2	57.8

Table 5. Friction Velocity

u* (m/s)	Integral Analysis		Velocity Profile		Skin Friction Gage	
	M = .22	M = .65	M = .22	M = .65	M = .22	M = .65
Smooth Plate	2.90	8.15	2.69	7.77	2.72	7.54
2D Plate	4.74	13.4	5.51	15.7	6.38	18.5
3D Plate	4.76	12.3	3.81	13.5	5.14	10.7
80 Grit Plate	4.25	12.1	4.82	14.0	4.54	12.9
36 Grit Plate	4.52	13.4	5.60	15.7	5.46	15.7
20 Grit Plate	4.92	13.7	5.49	15.2	5.69	17.9

Table 6. Summary of Numerical Roughness Data

Model	δ (mm)	θ (mm)	C_f
Smooth	11.8	0.77	0.0015
2D, van Driest	16.8	1.23	0.0030
2D, Kragstad	19.0	1.41	0.0035
2D, Cebeci-Chang	18.6	1.37	0.0033
3D, van Driest	16.8	1.21	0.0029
3D, Kragstad	18.6	1.37	0.0034
3D, Cebeci-Chang	18.2	1.33	0.0032
80 Grit, van Driest	15.9	1.13	0.0027
80 Grit, Kragstad	16.8	1.21	0.0029
80 Grit, Cebeci-Chang	16.2	1.16	0.0028
36 Grit, van Driest	17.2	1.26	0.0031
36 Grit, Kragstad	19.3	1.45	0.0038
36 Grit, Cebeci-Chang	19.3	1.44	0.0035
20 Grit, van Driest	17.2	1.29	0.0032
20 Grit, Kragstad	19.7	1.49	0.0040
20 Grit, Cebeci-Chang	20.5	1.53	0.0038

Figures

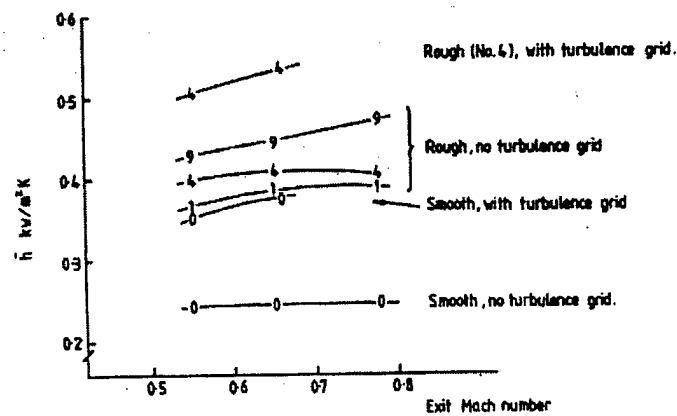
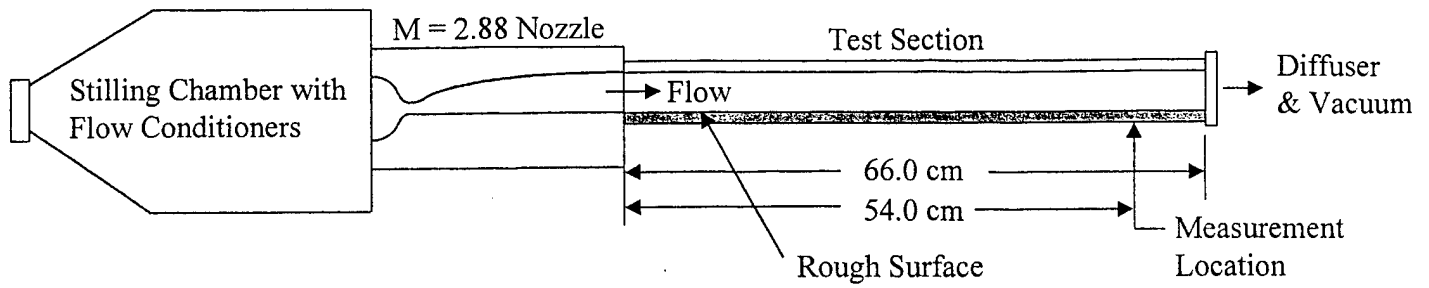
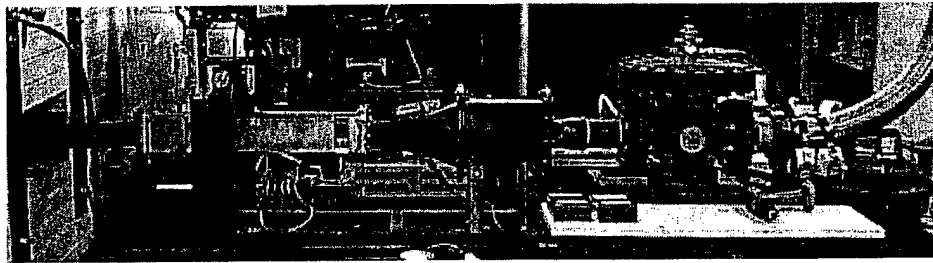


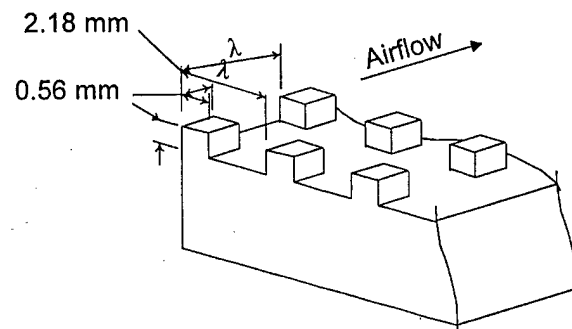
Fig. 1 Effect of Roughness and Freestream Turbulence (7%) on mean heat transfer coefficients in a high pressure turbine stage, $Re = 1.2 \times 10^6$, and 0, 1, 4, and 9 correspond to smooth and distributed particle sizes of 54, 105, and 250 μm , respectively [Turner et al. (1985) as shown in Lakshminarayana (1996)].



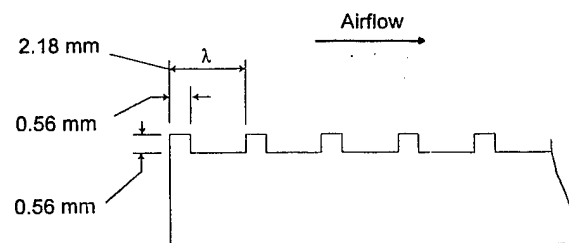
(a) Schematic of Supersonic Wind Tunnel



(b) Photograph of Subsonic Wind Tunnel

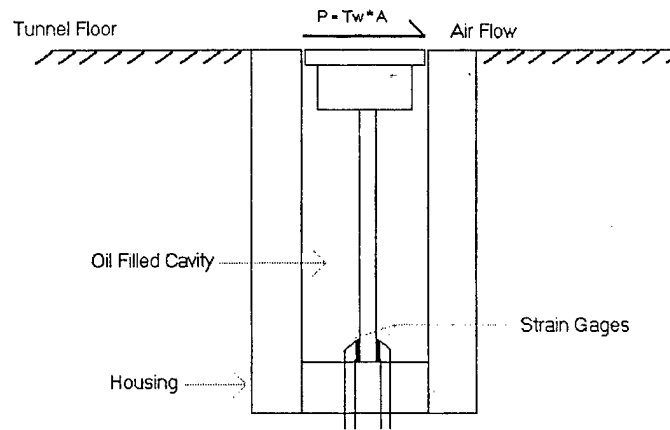


Three-Dimensional Plate

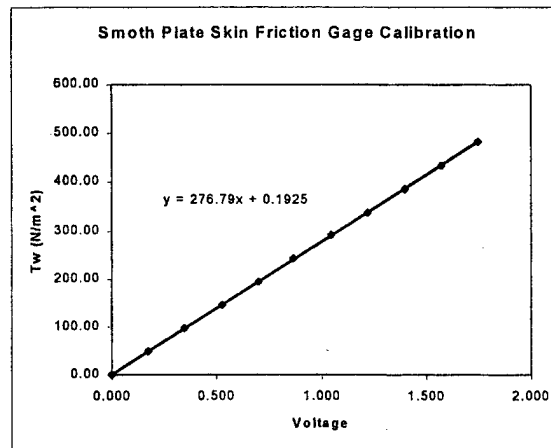


Two-Dimensional Plate

(c) Machined Roughness Patterns



(d) Skin Friction Gage Concept

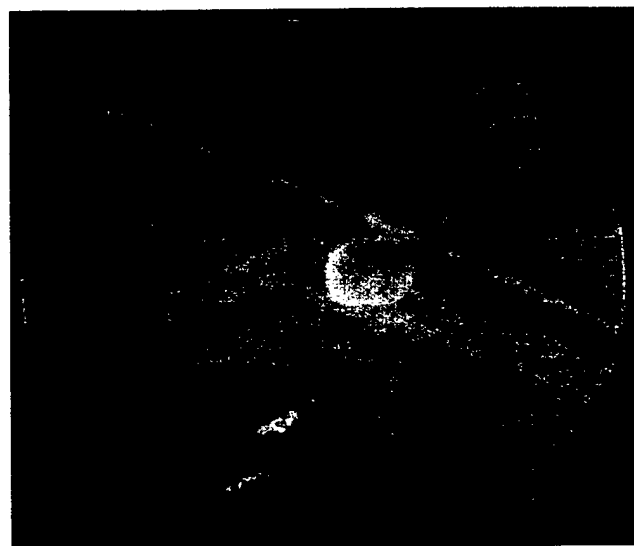


(e) Fig 6 P & B

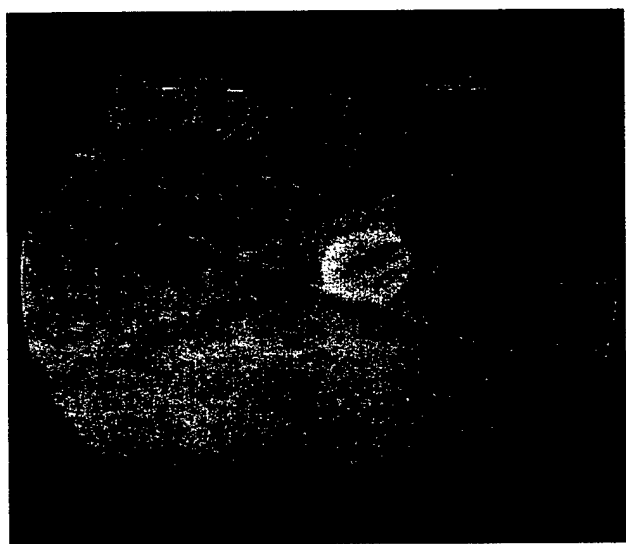
Figure 2. Wind Tunnel Facilities and Models



Flat Plate Color Schlieren



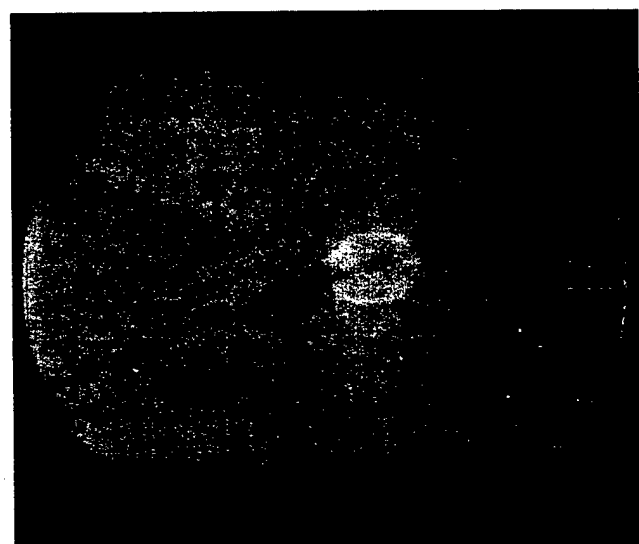
80 Grit Plate Color Schlieren



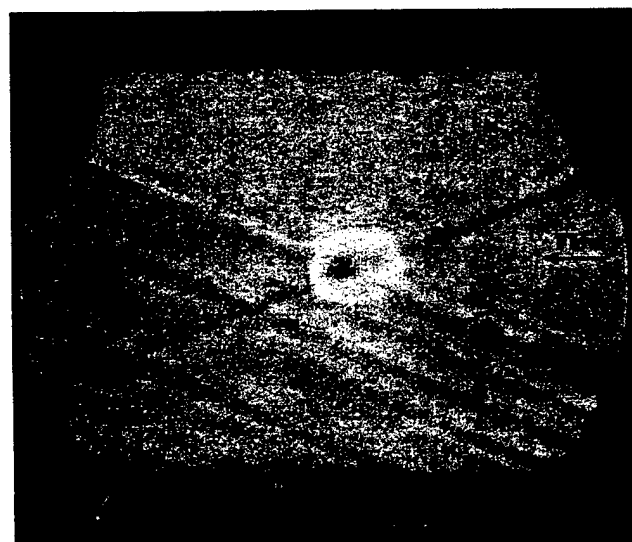
3D Plate Color Schlieren



36 Grit Plate Color Schlieren

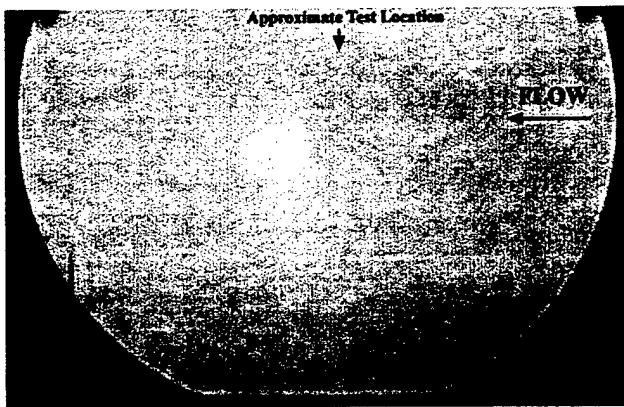


2D Plate Color Schlieren

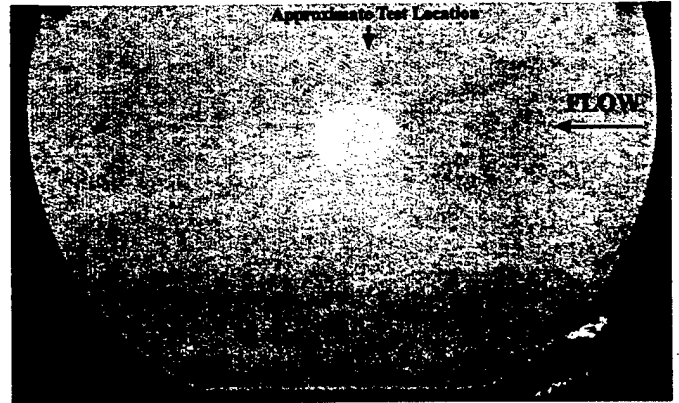


20 Grit Plate Color Schlieren

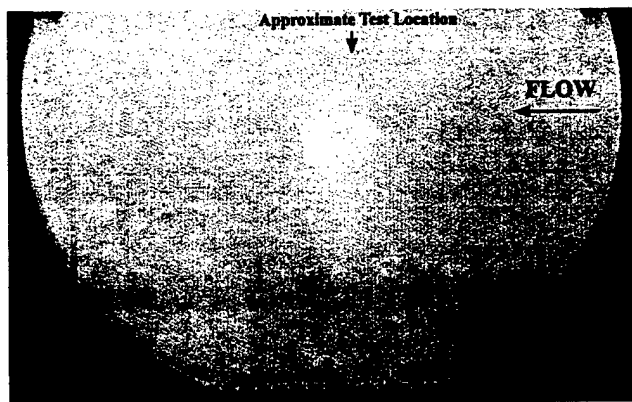
Figure 3a. Nozzle Exit, Horizontal Knife Edge, Color Schlierens



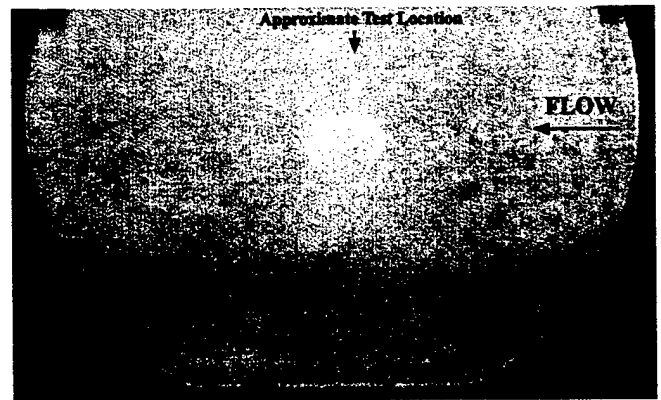
Flat Plate Color Schlieren



80 Grit Plate Color Schlieren



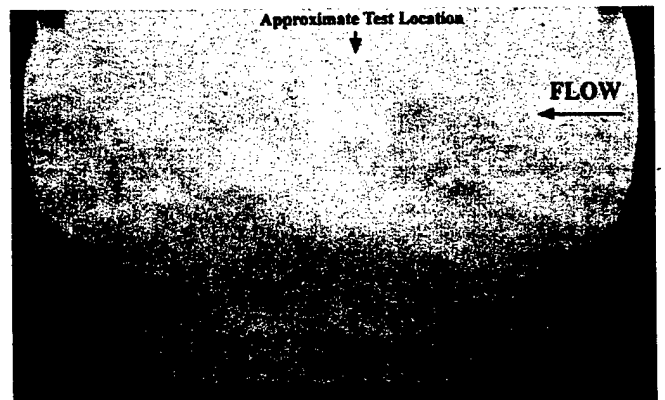
3D Plate Color Schlieren



36 Grit Plate Color Schlieren

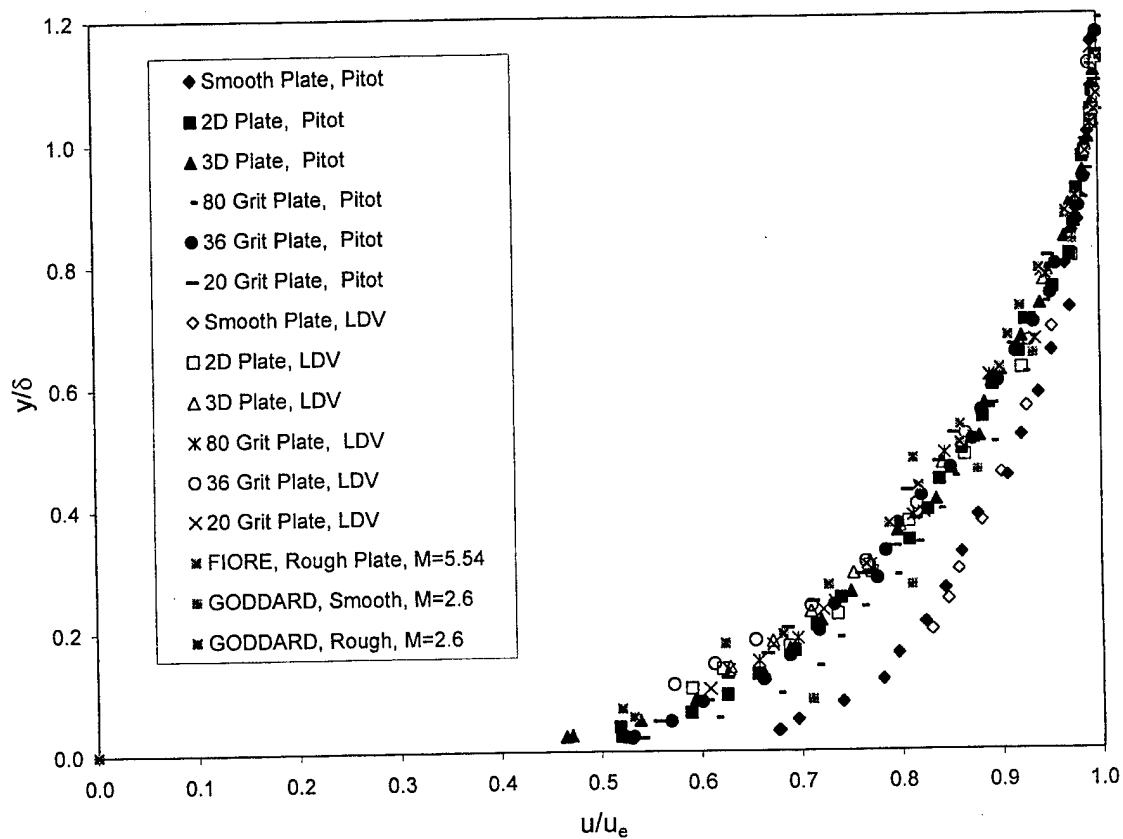


2D Plate Color Schlieren

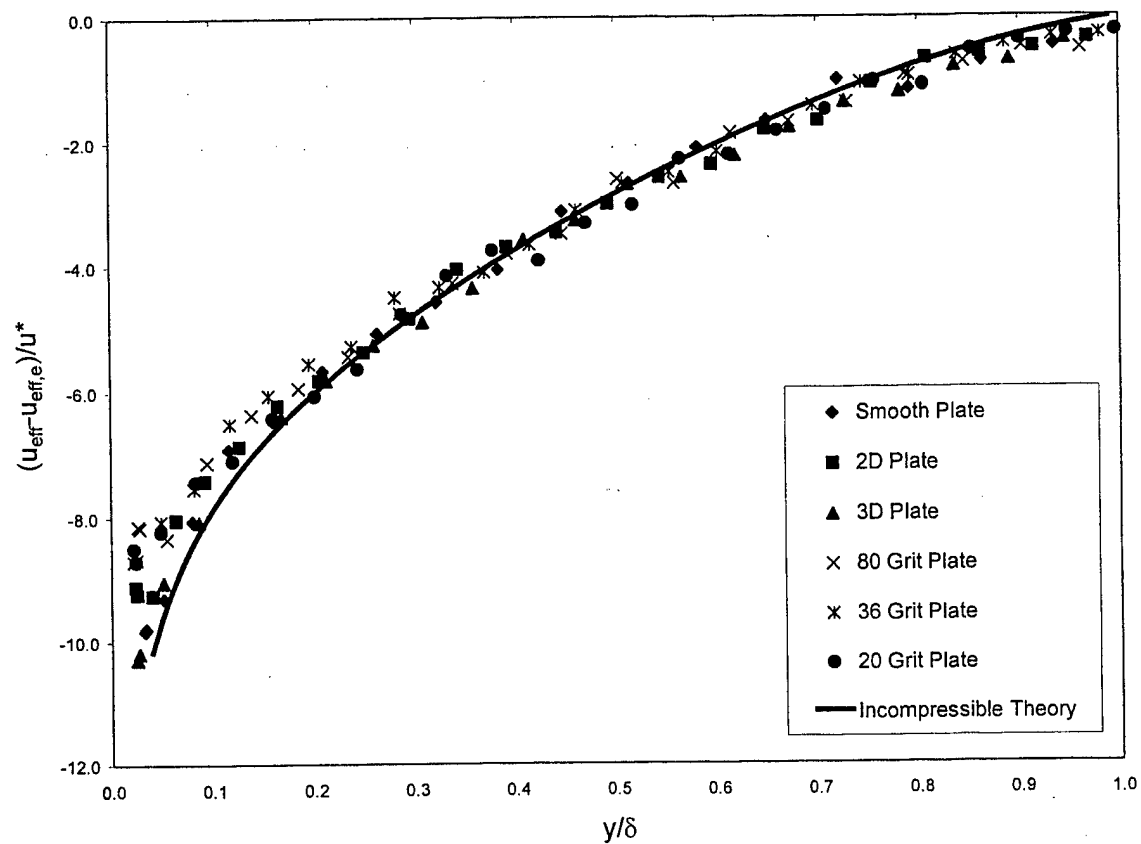


20 Grit Plate Color Schlieren

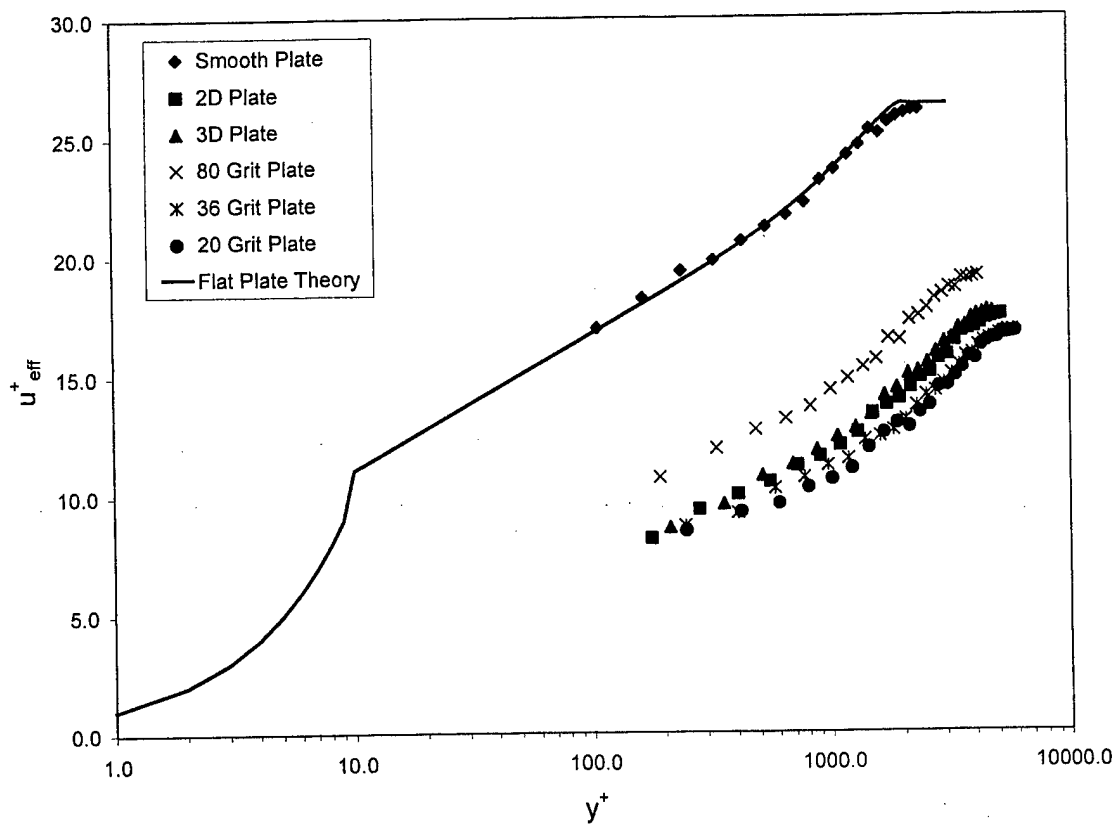
Figure 3b. Test Location, Horizontal Knife Edge, Color Schlierens



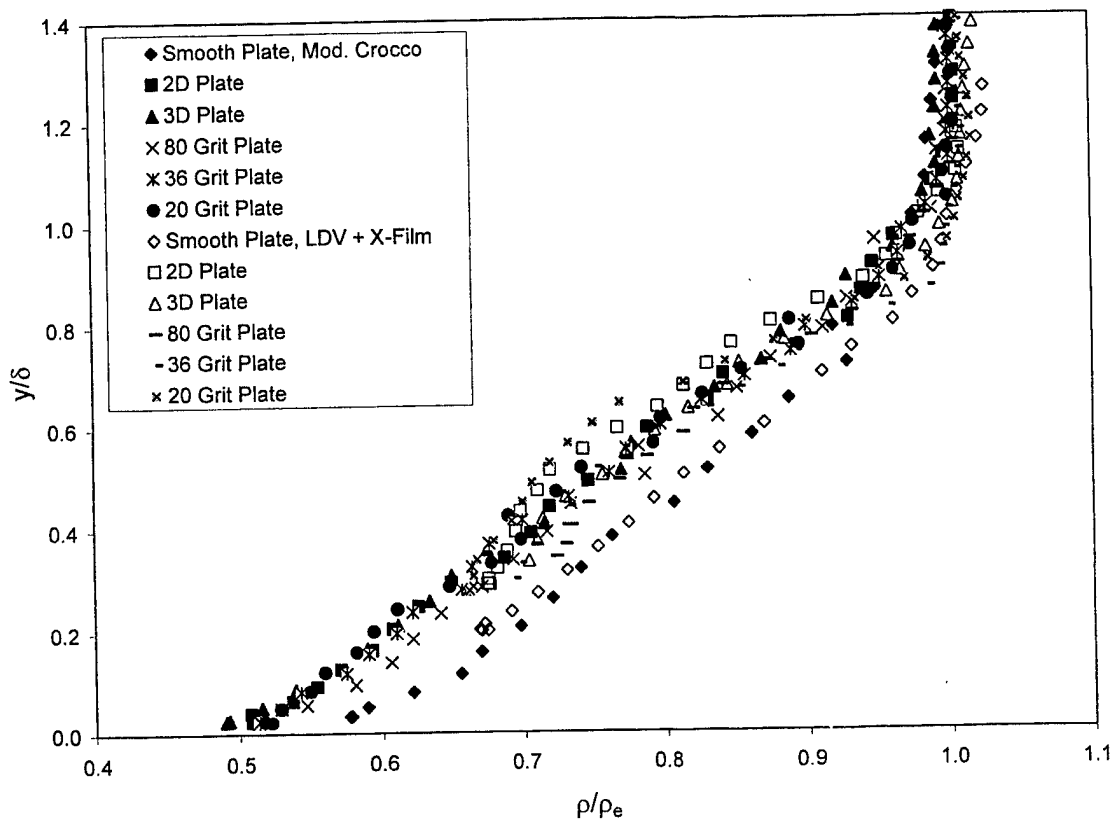
(a) Mean Velocity Profiles (LDA and Pitot Data)



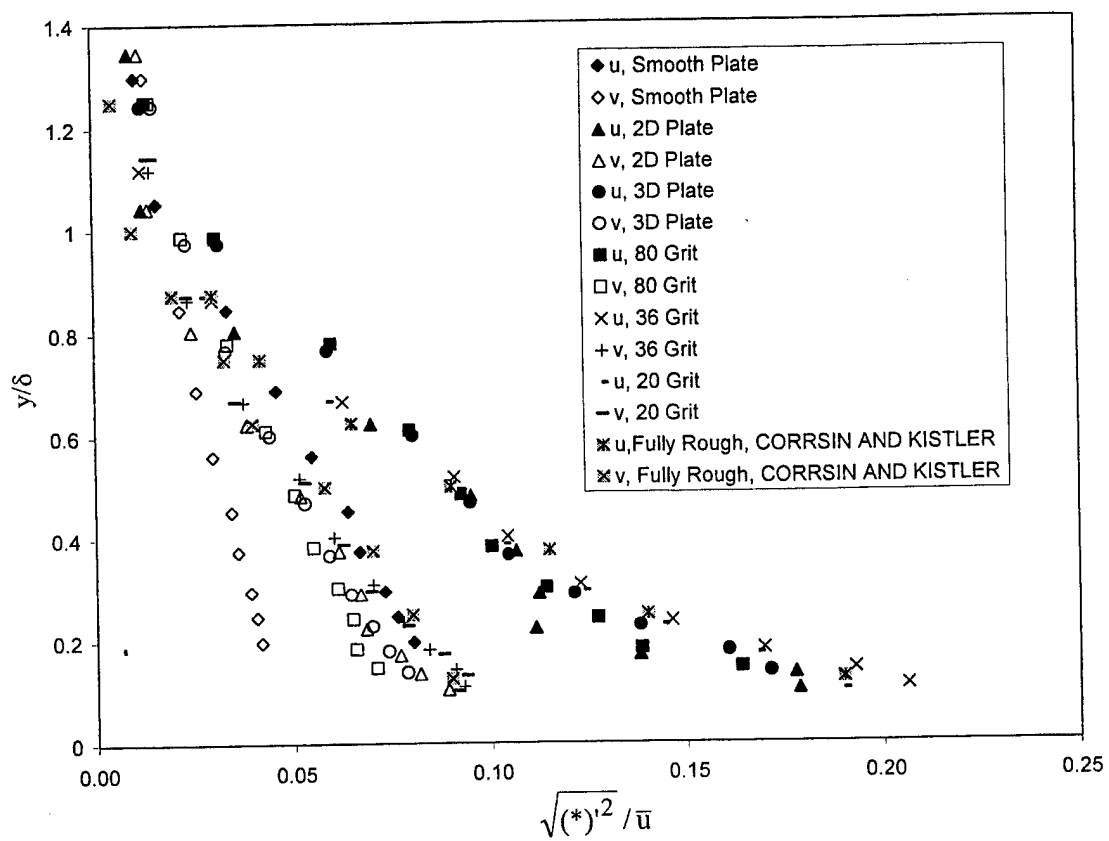
(b) Effective Velocity Defect (Pitot Data)



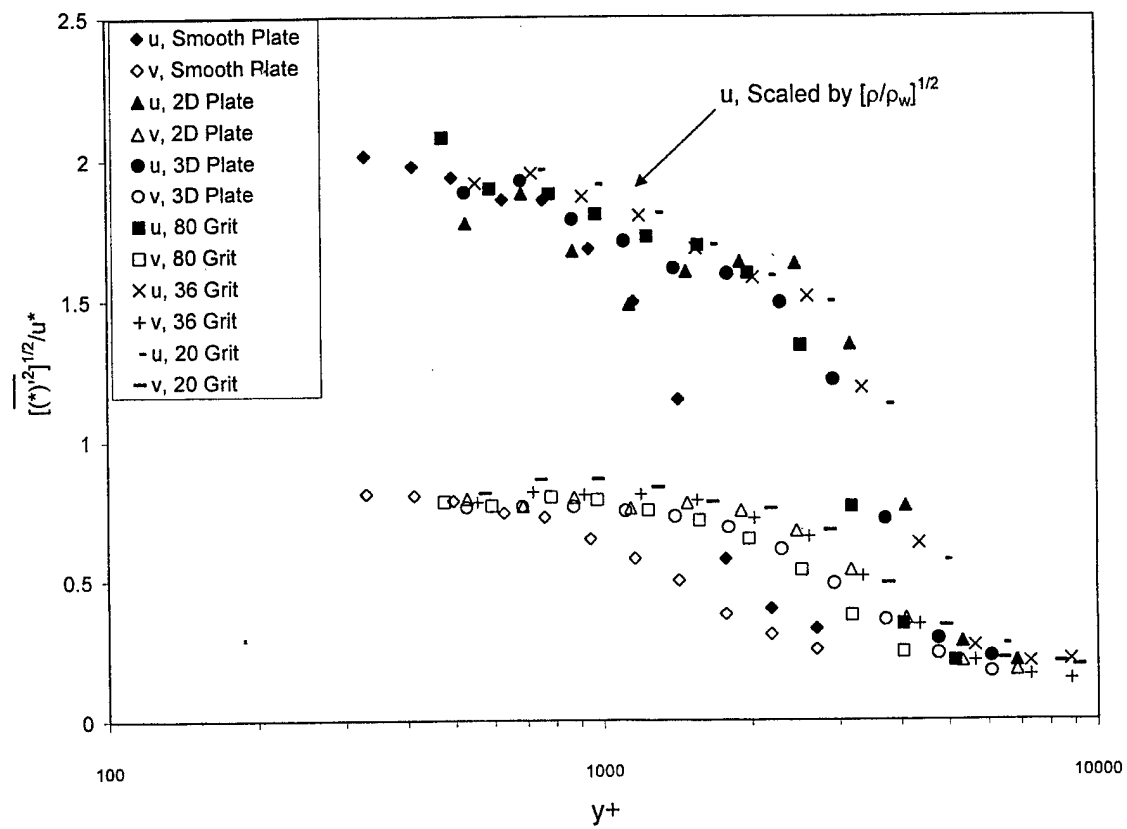
(c) Effective Law of the Wall Plot (Pitot Data)



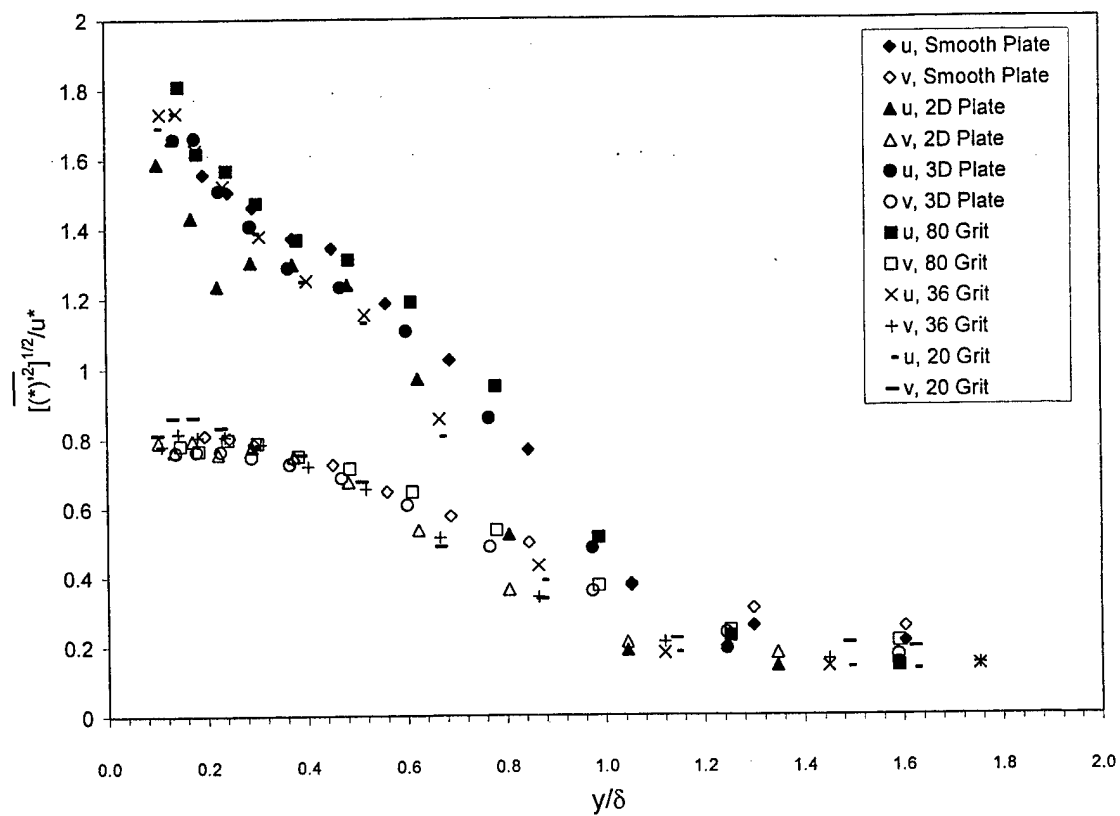
(d) Density (Modified Crocco and Combined LDA and Cross-Film)
Figure 4 Mean Flow Profile Data



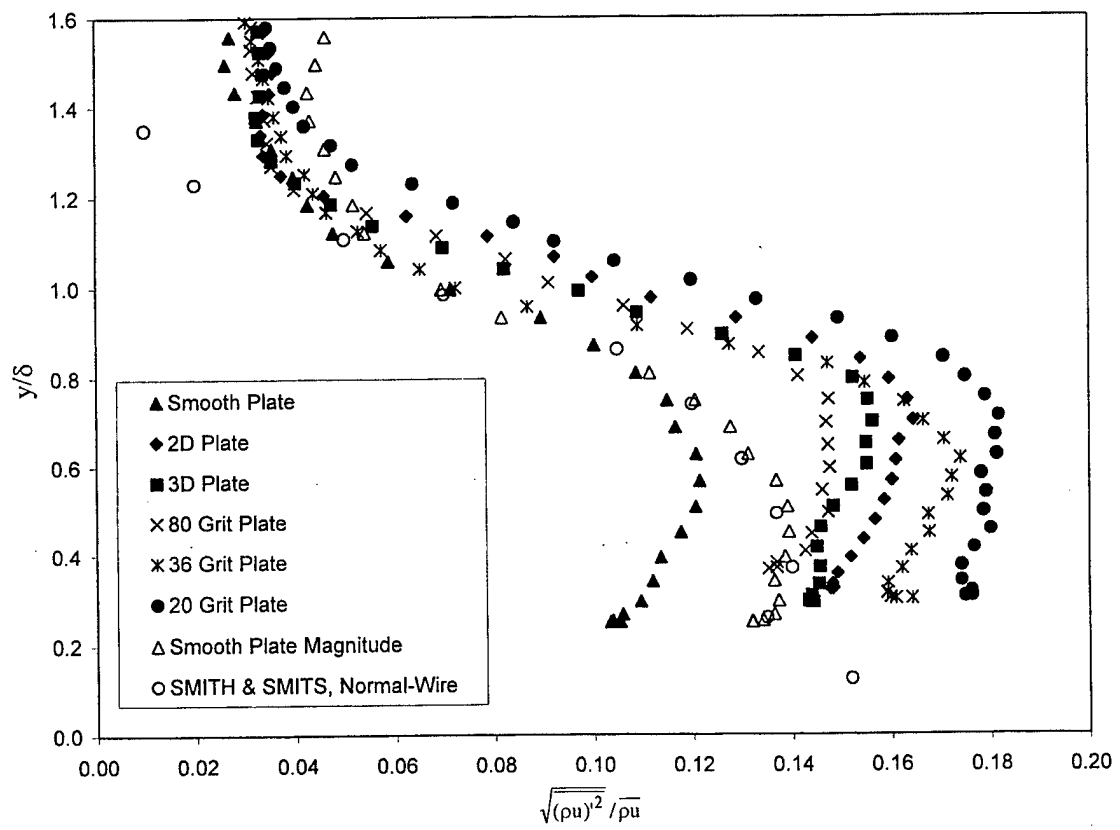
(a) Outer Variable Scaling



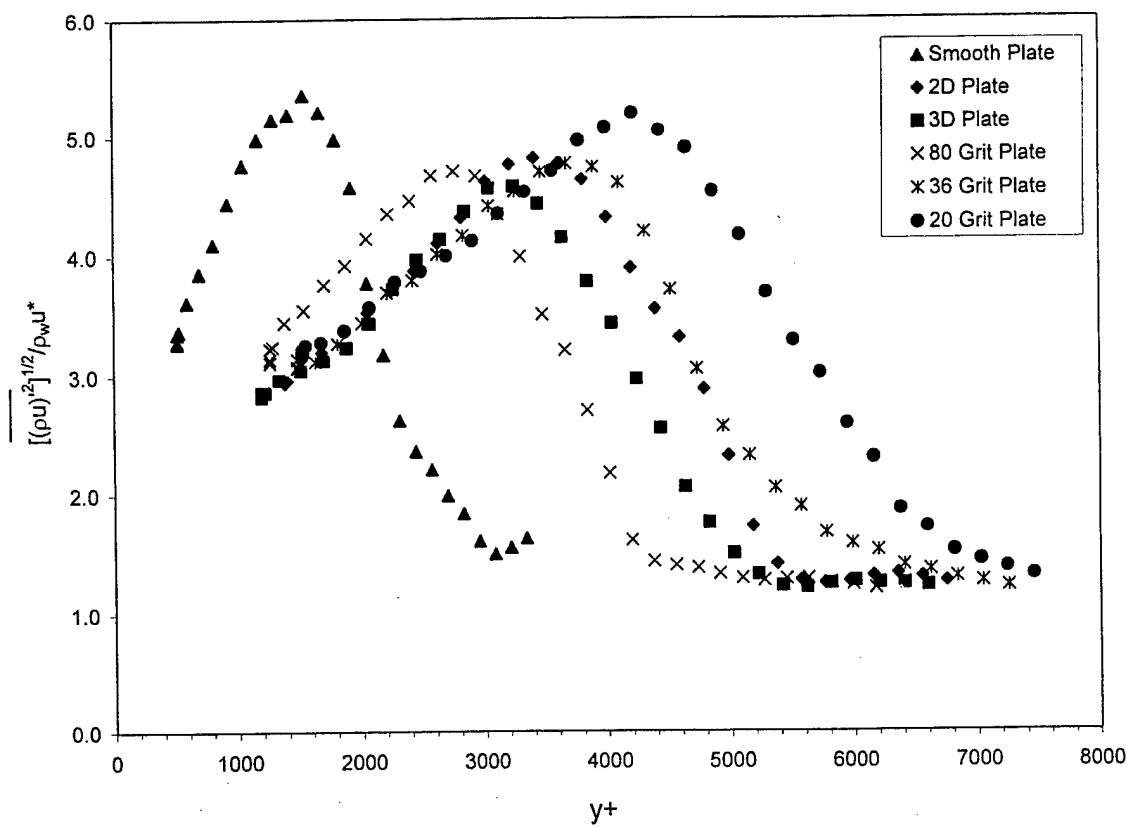
(b) Inner Variable Scaling



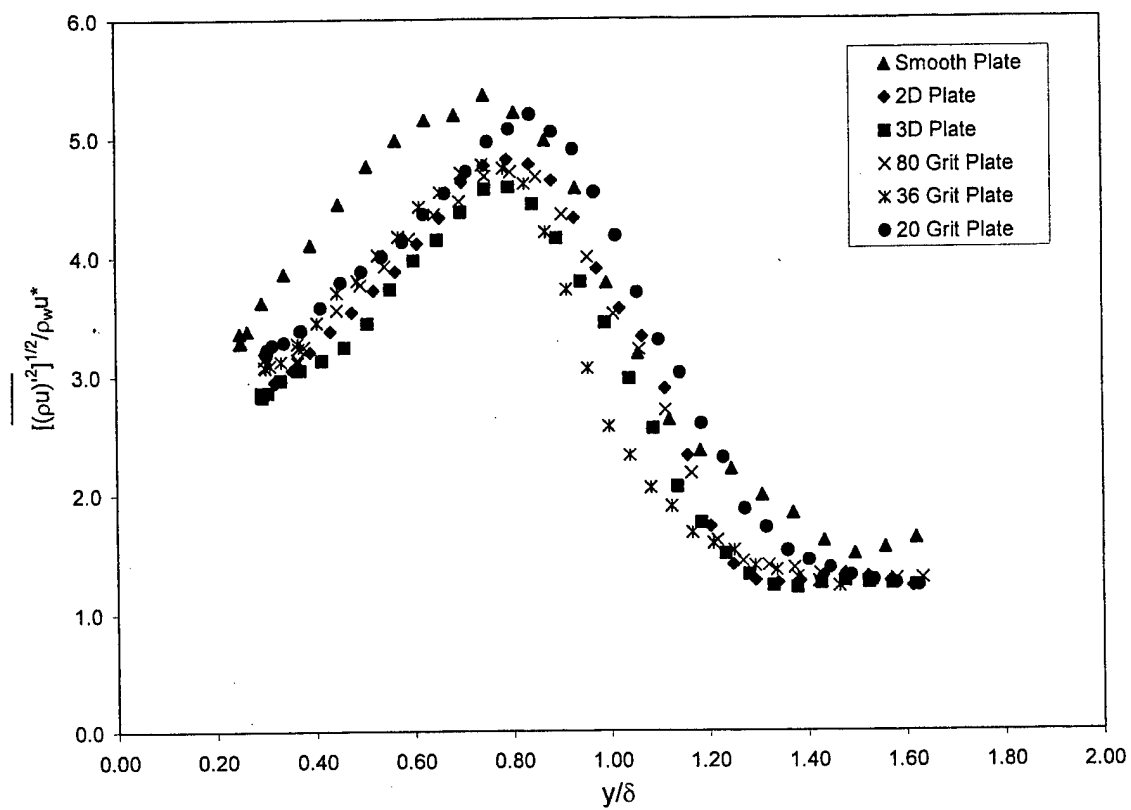
(c) Mixed Variable Scaling
 Fig. 5 u - and v -Turbulence Intensity Profiles



(a) Outer Variable Scaling



(b) Inner Variable Scaling



(c) Mixed Variable Scaling
 Fig. 6 ρu -Turbulence Intensity Profiles

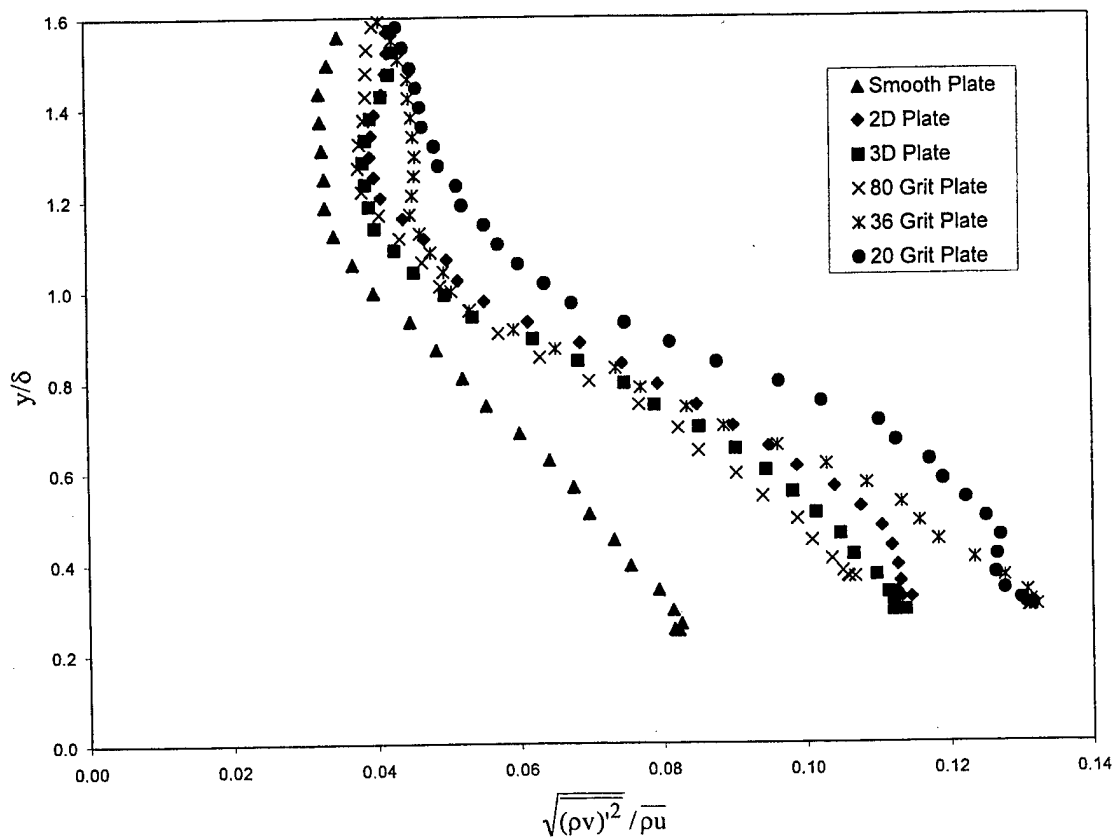


Fig. 7 ρv -Turbulence Intensity Profiles (Outer Variable Scaling)

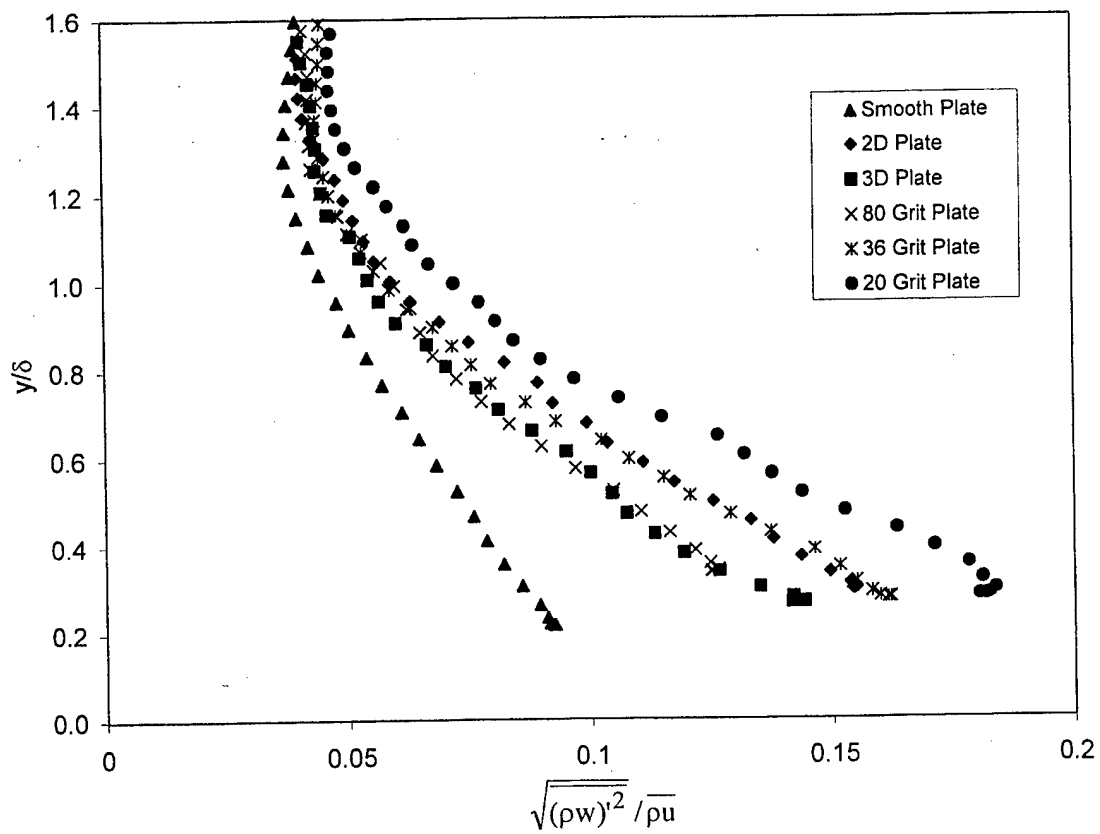


Fig. 8 ρw -Turbulence Intensity Profiles (Outer Variable Scaling)

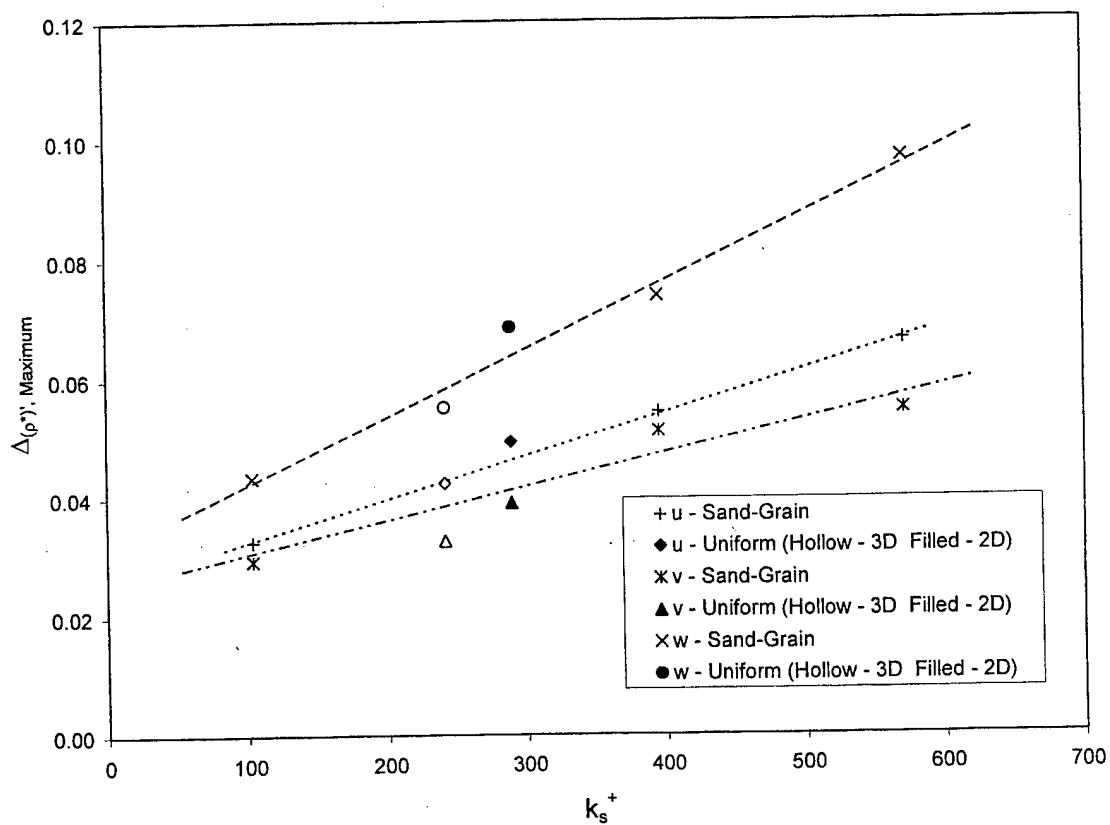
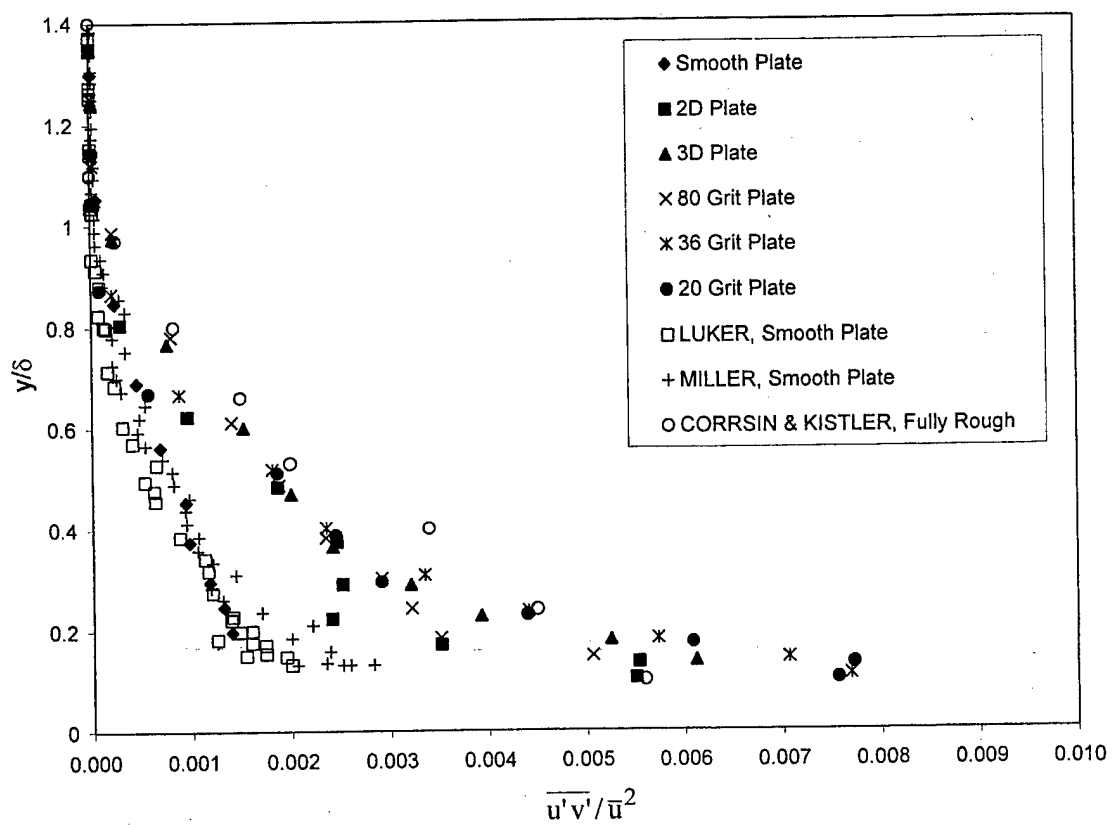
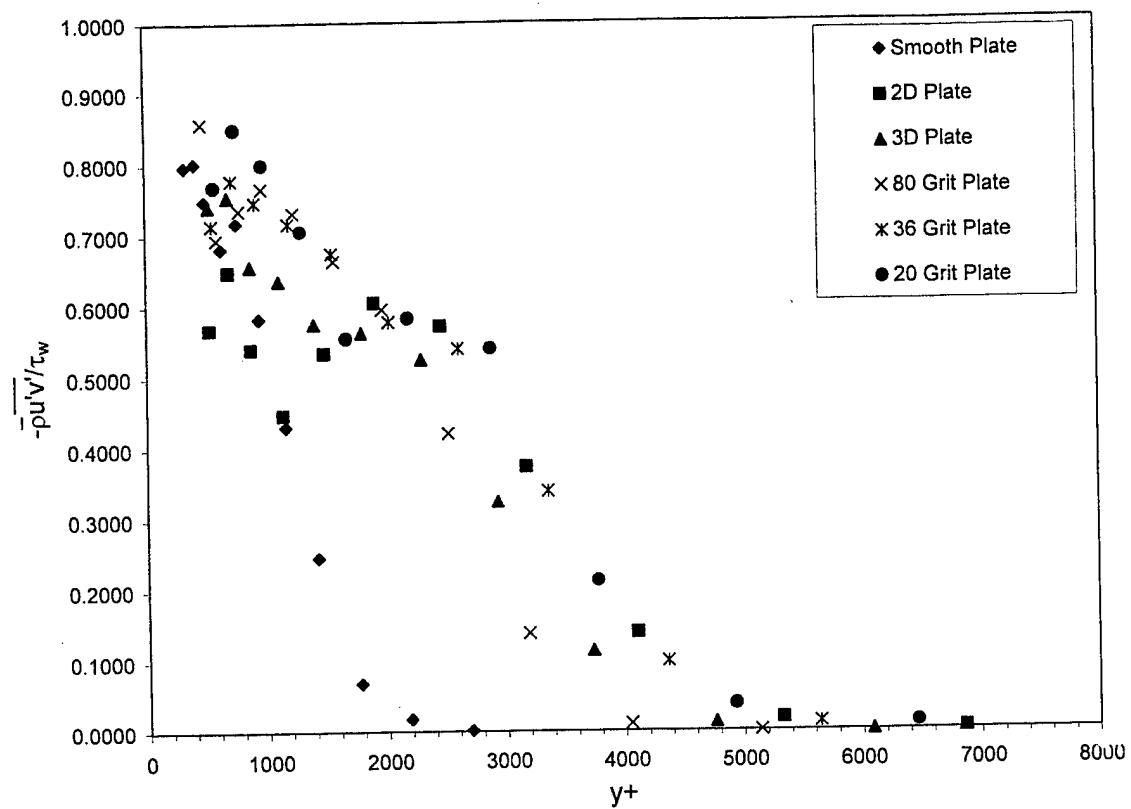


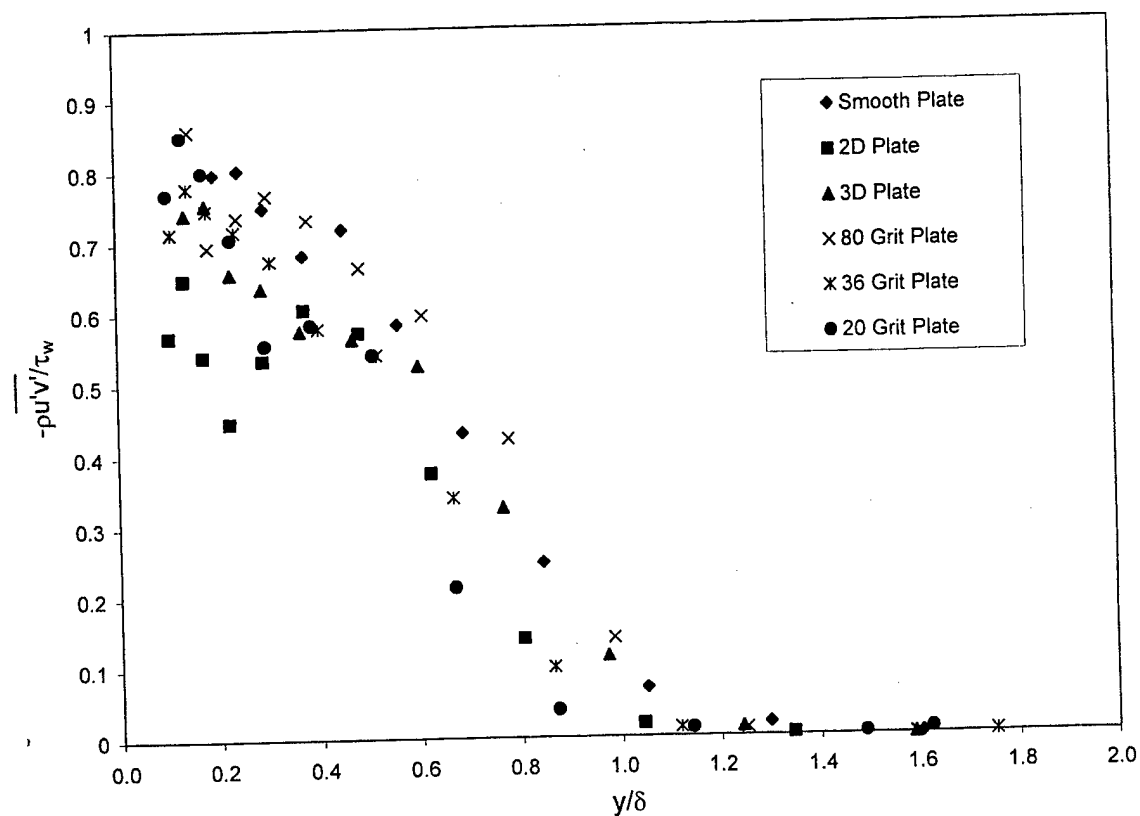
Fig. 9 Mass Flux Turbulence Intensities Versus k_s^+ (Outer Variable Scaling)



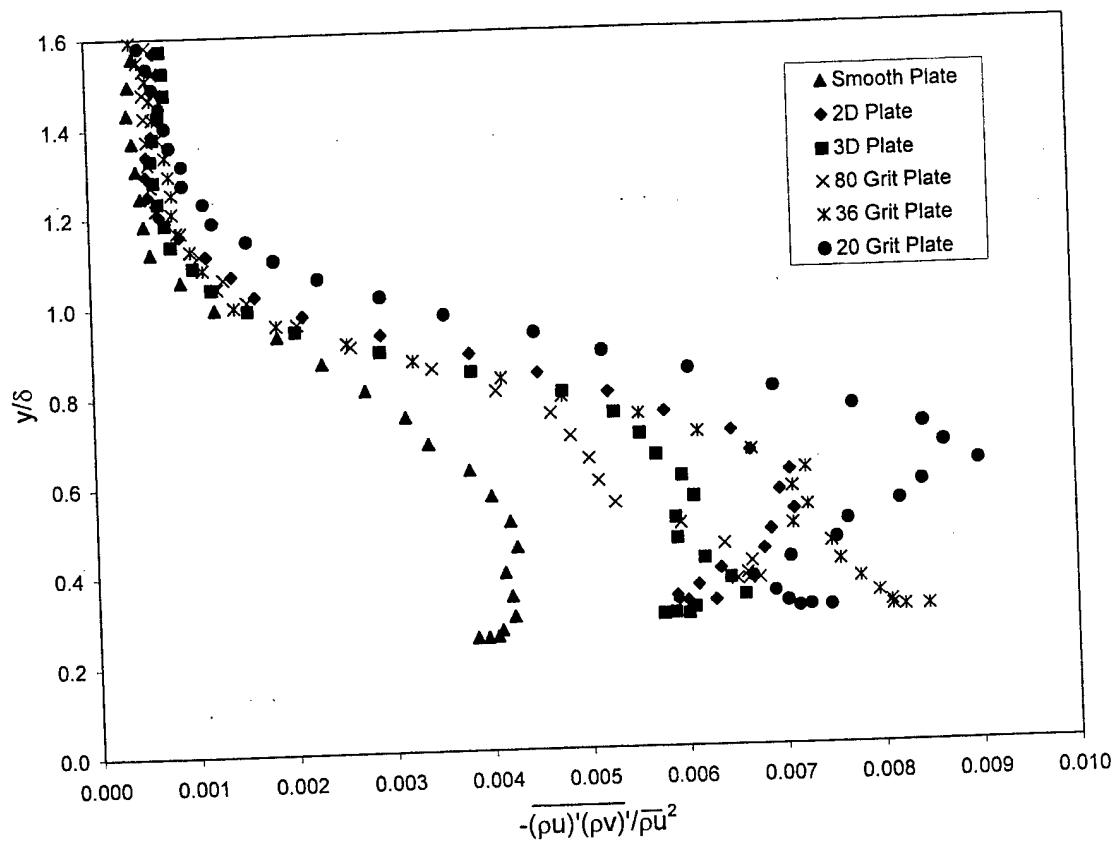
(a) Outer Variable Scaling



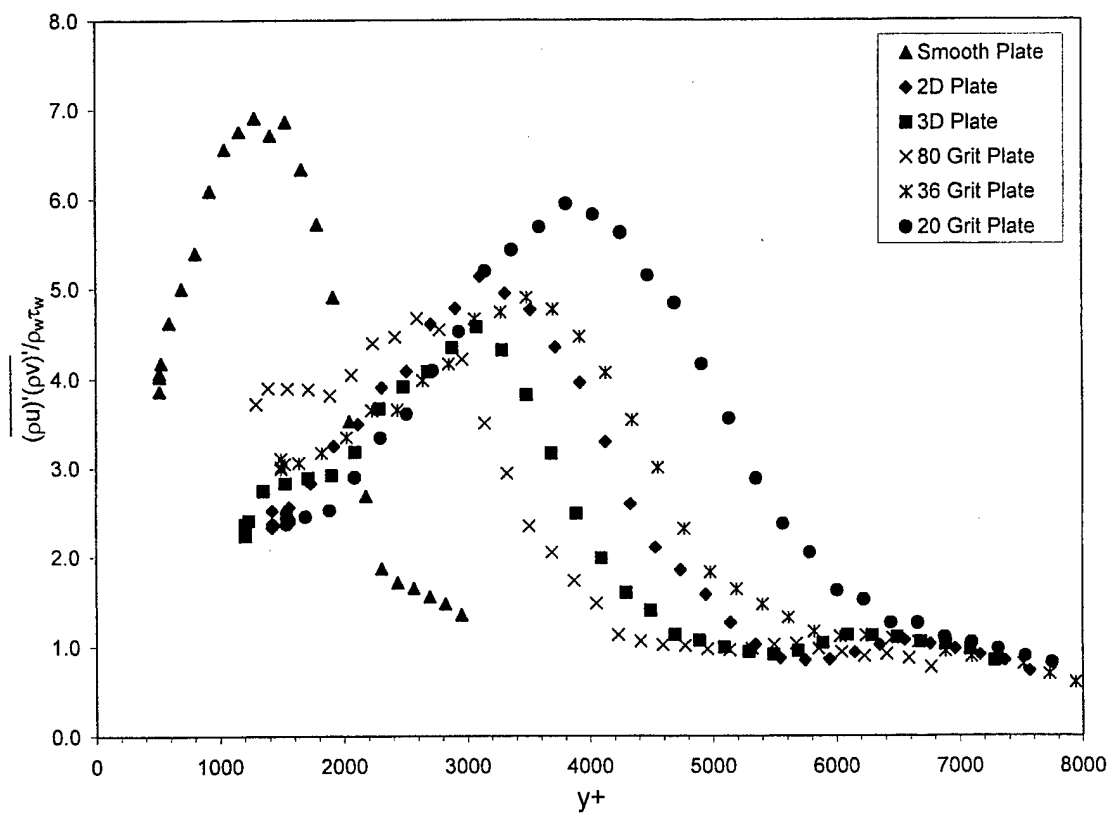
(b) Inner Variable Scaling



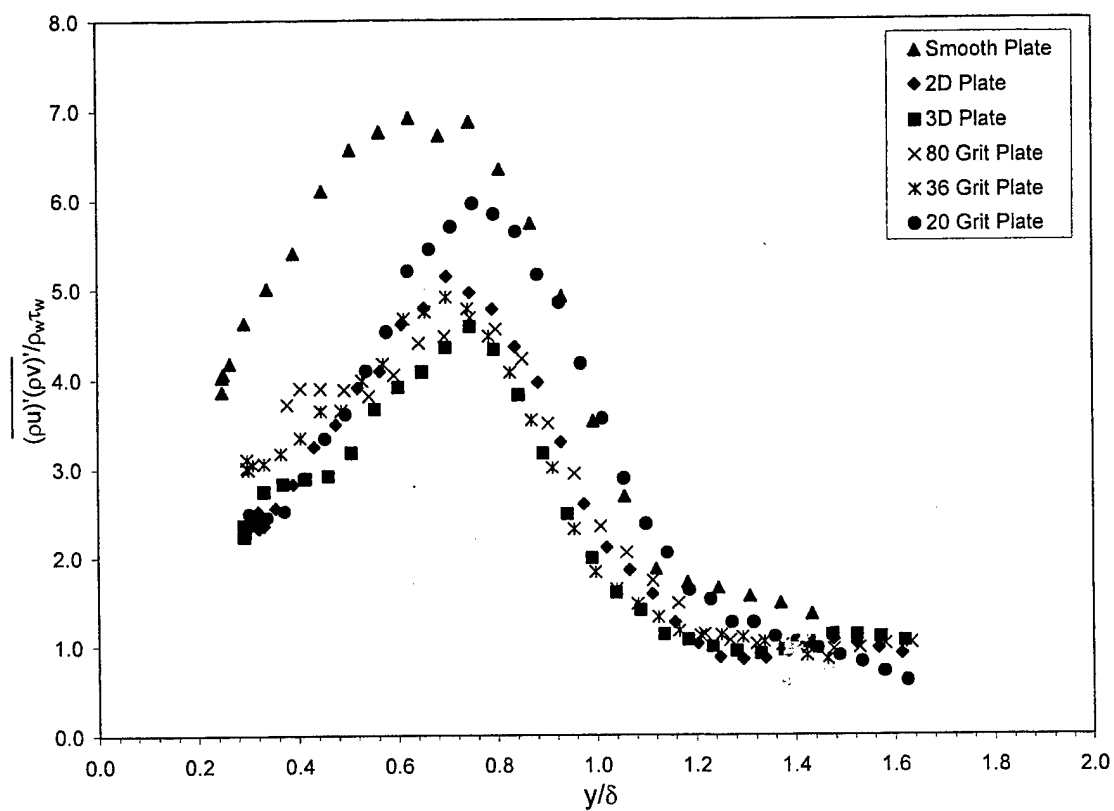
(c) Mixed Variable Scaling
 Fig. 10 Kinematic Turbulent Shear Stress Profiles



(a) Outer Variable Scaling



(b) Inner Variable Scaling



(a) Mixed Variable Scaling
Fig. 11 X-Y component Compressible Reynolds Shear Stress

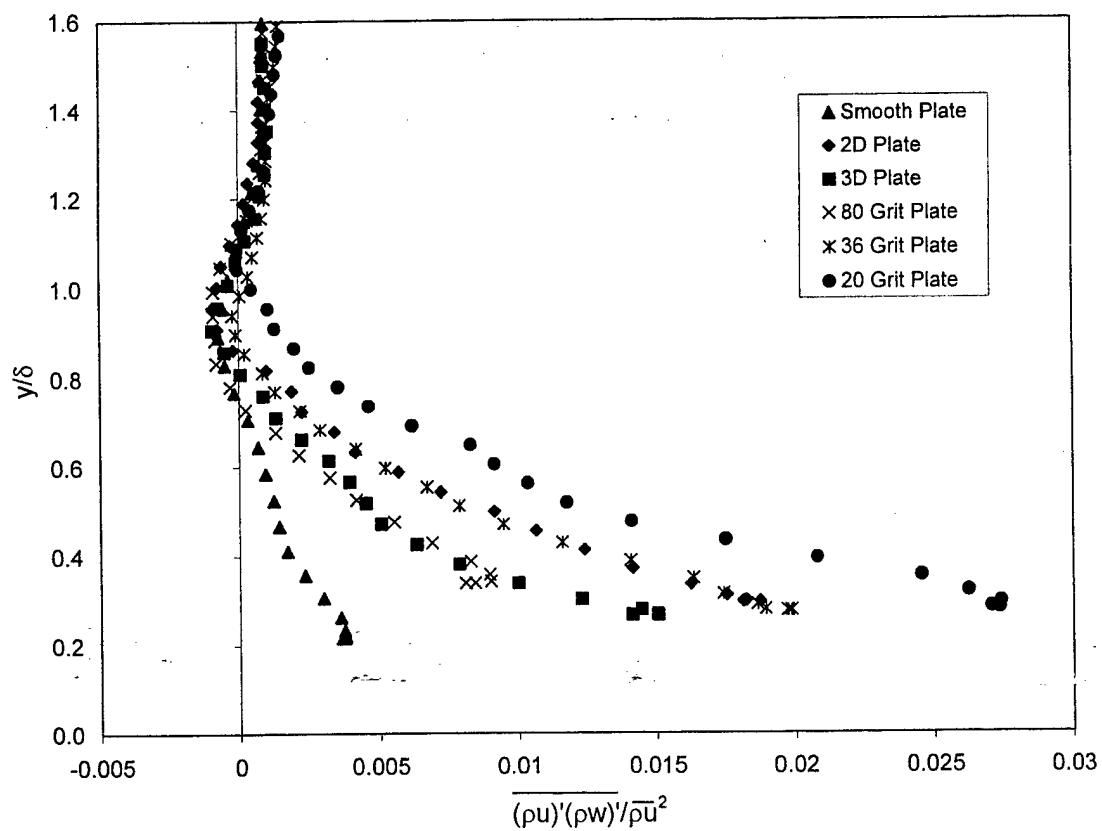


Fig. 12 X-Z Component Compressible Reynolds Shear Stress (Outer Variable Scaling)

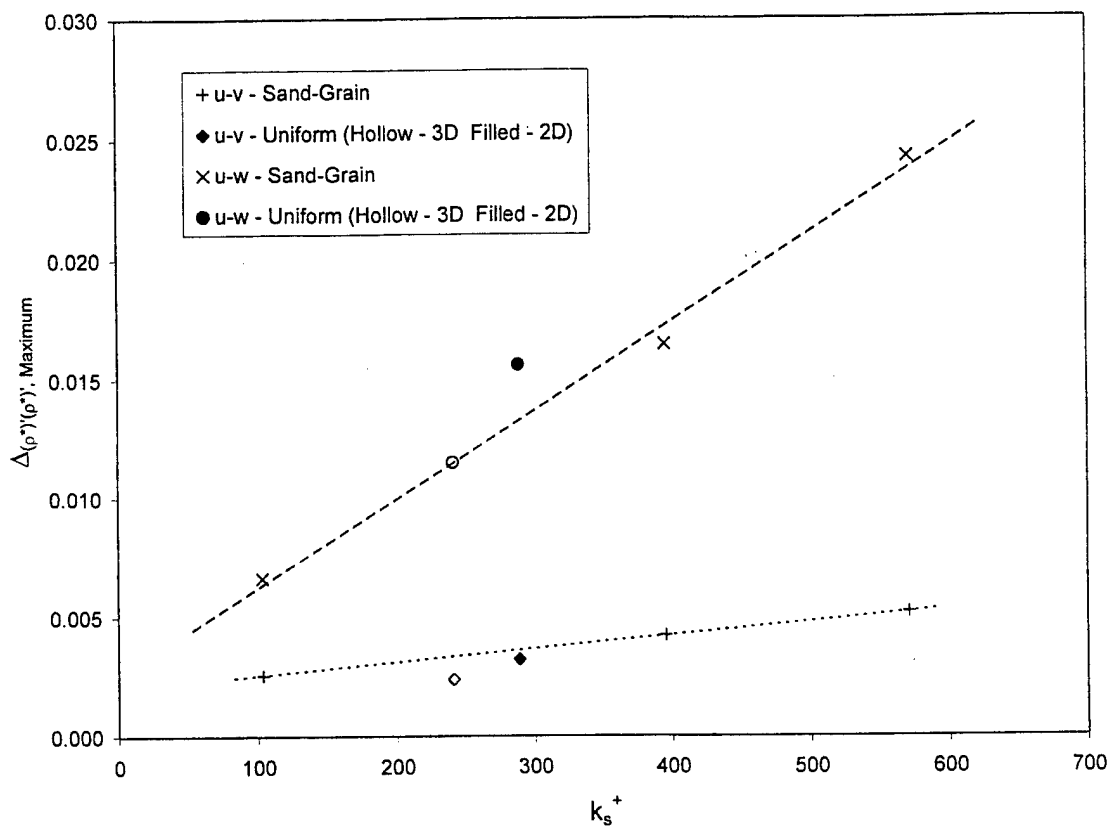
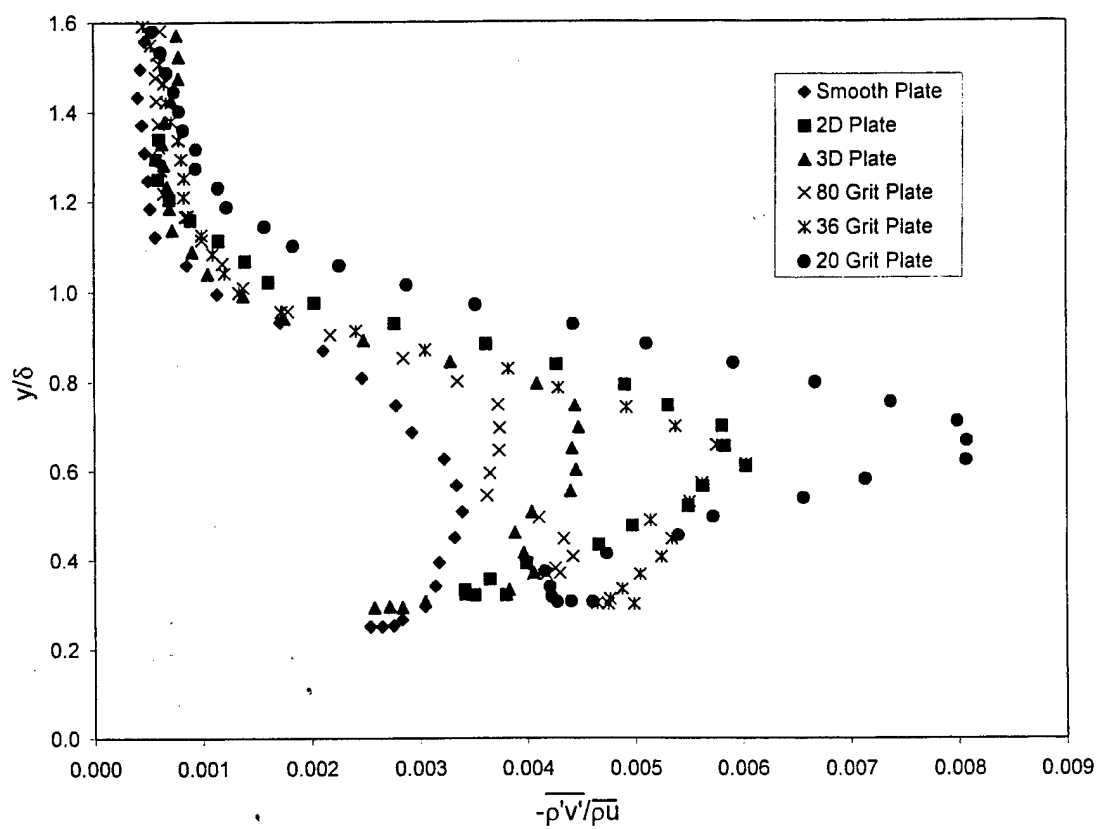
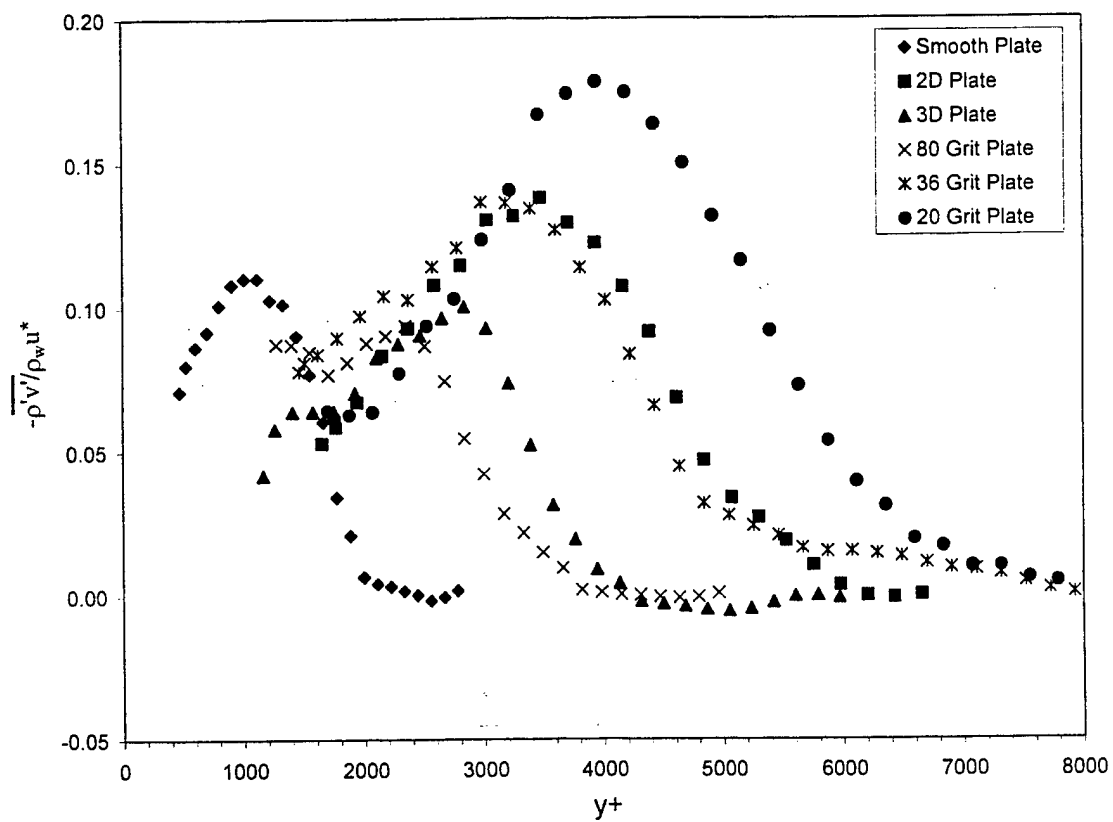


Fig. 13 Peak Difference in the Compressible Reynolds Shear Stress (outer scaling) versus k_s^+

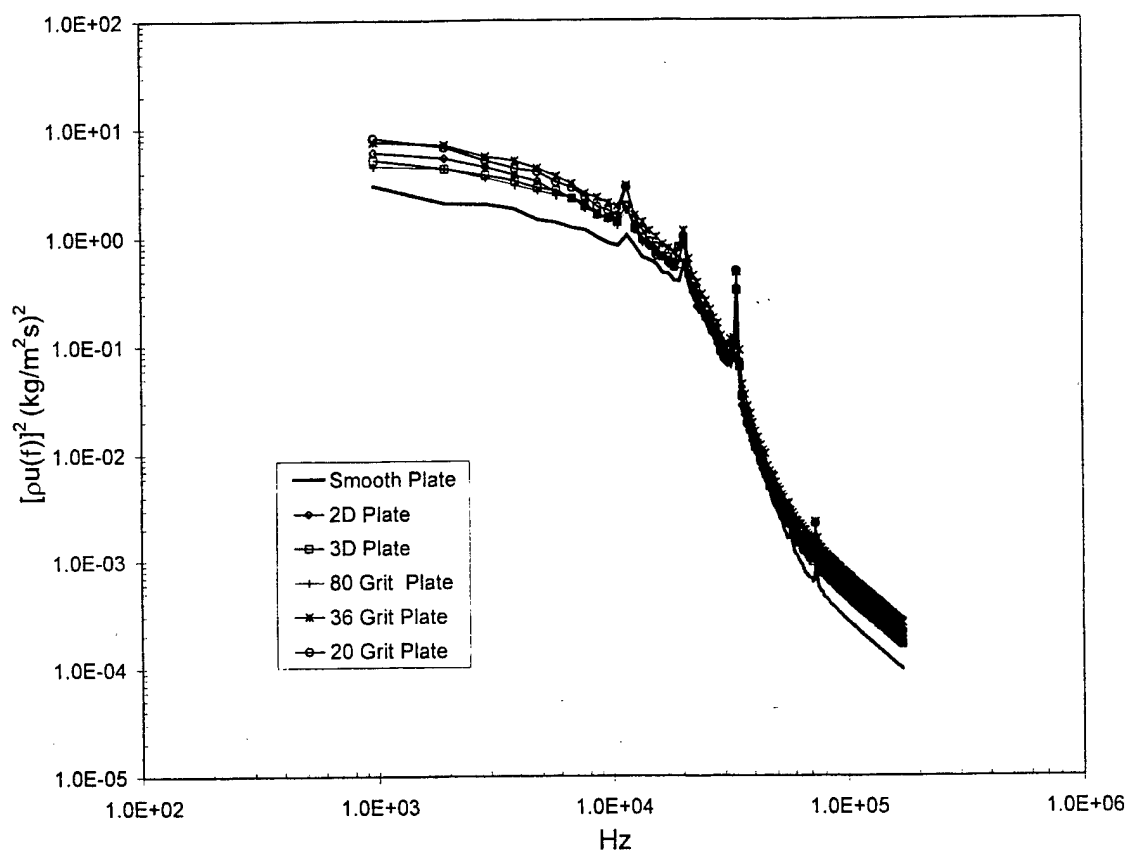


(a) Outer Variable Scaling

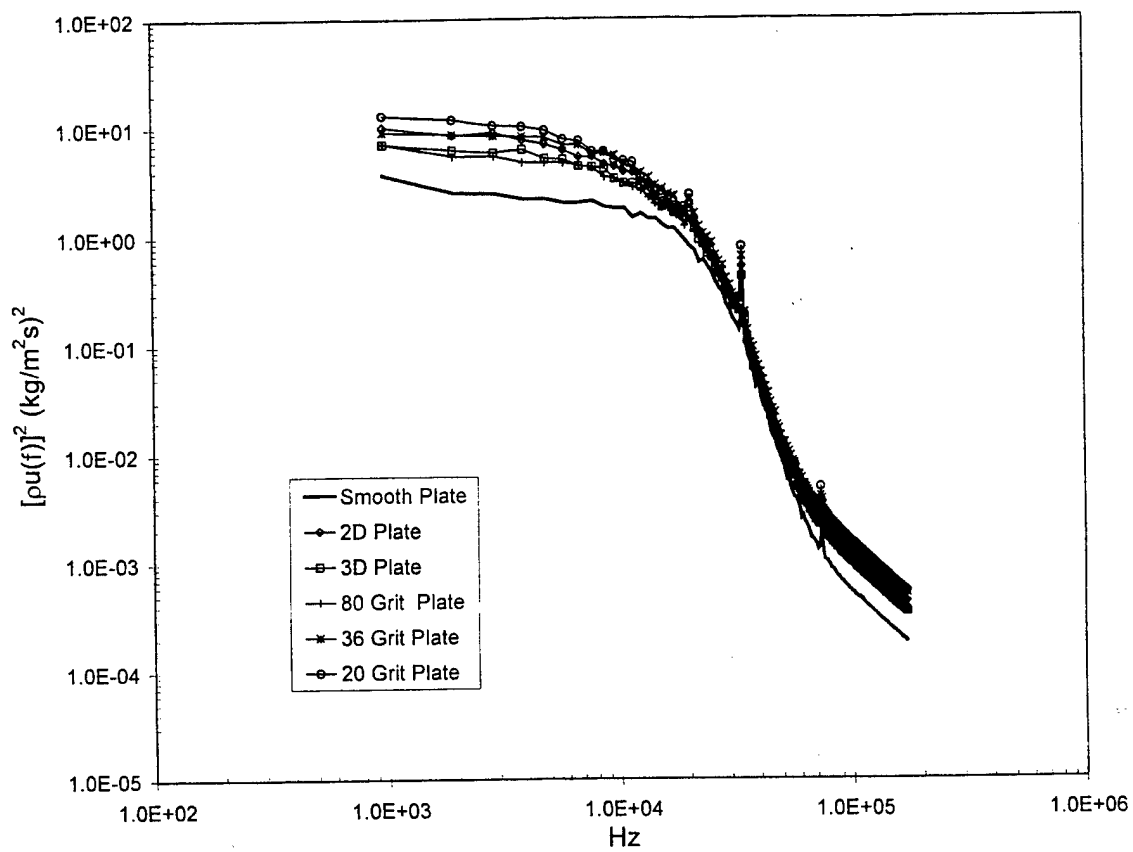


(b) Inner Variable Scaling

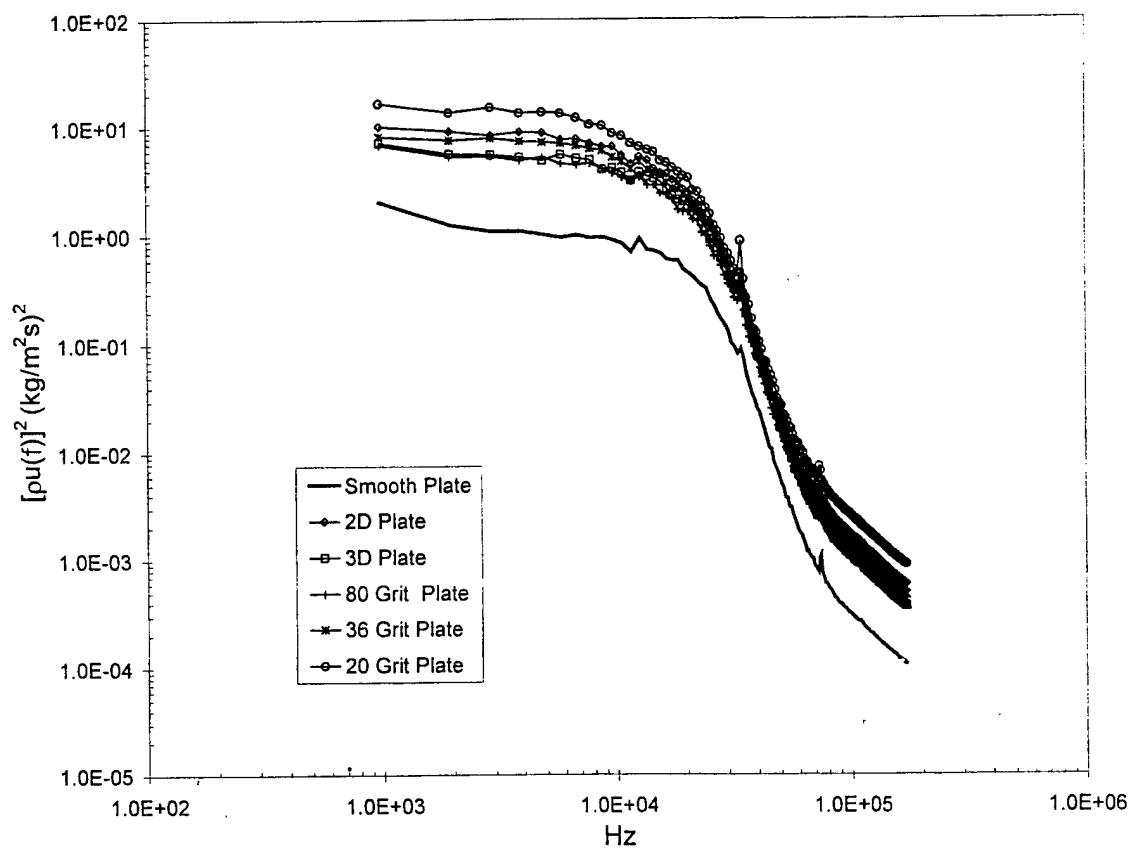
Figure 14 Second Order Density-Velocity Correlation Results



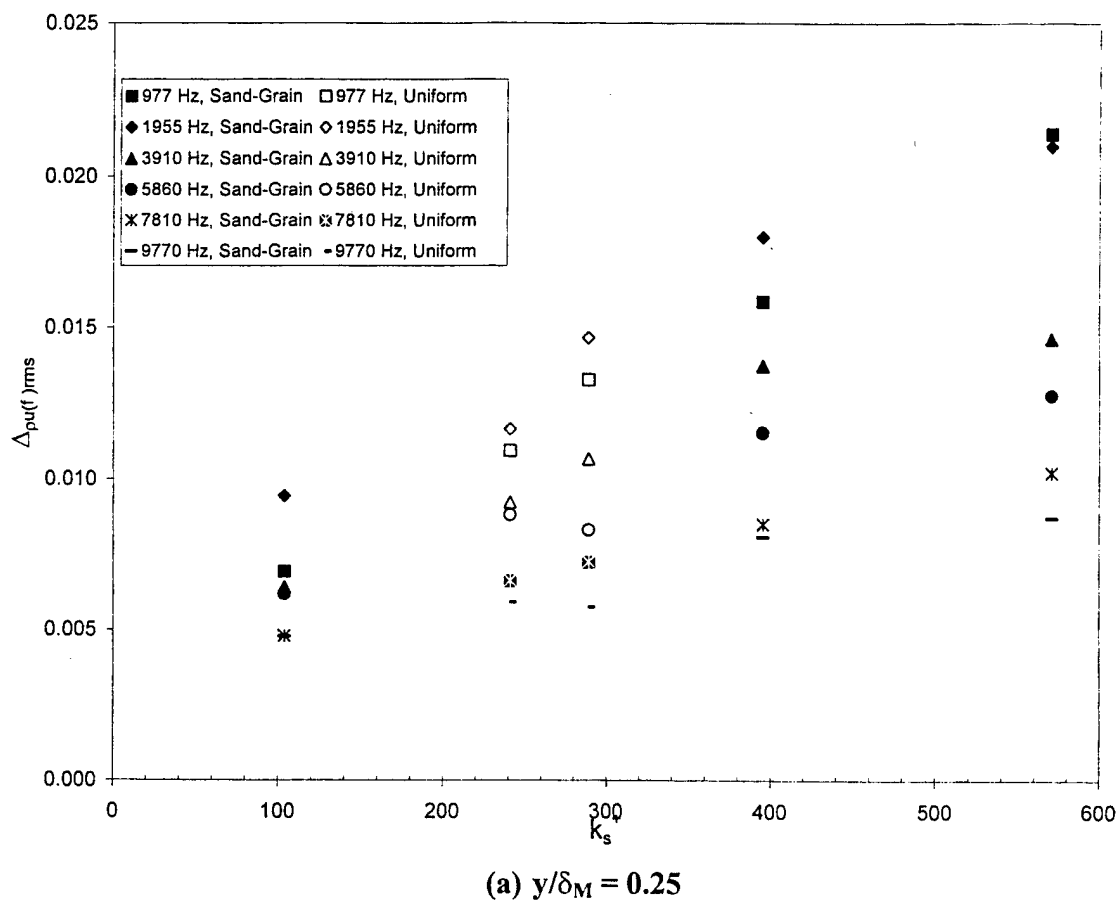
(a) $y/\delta_M = 0.25$

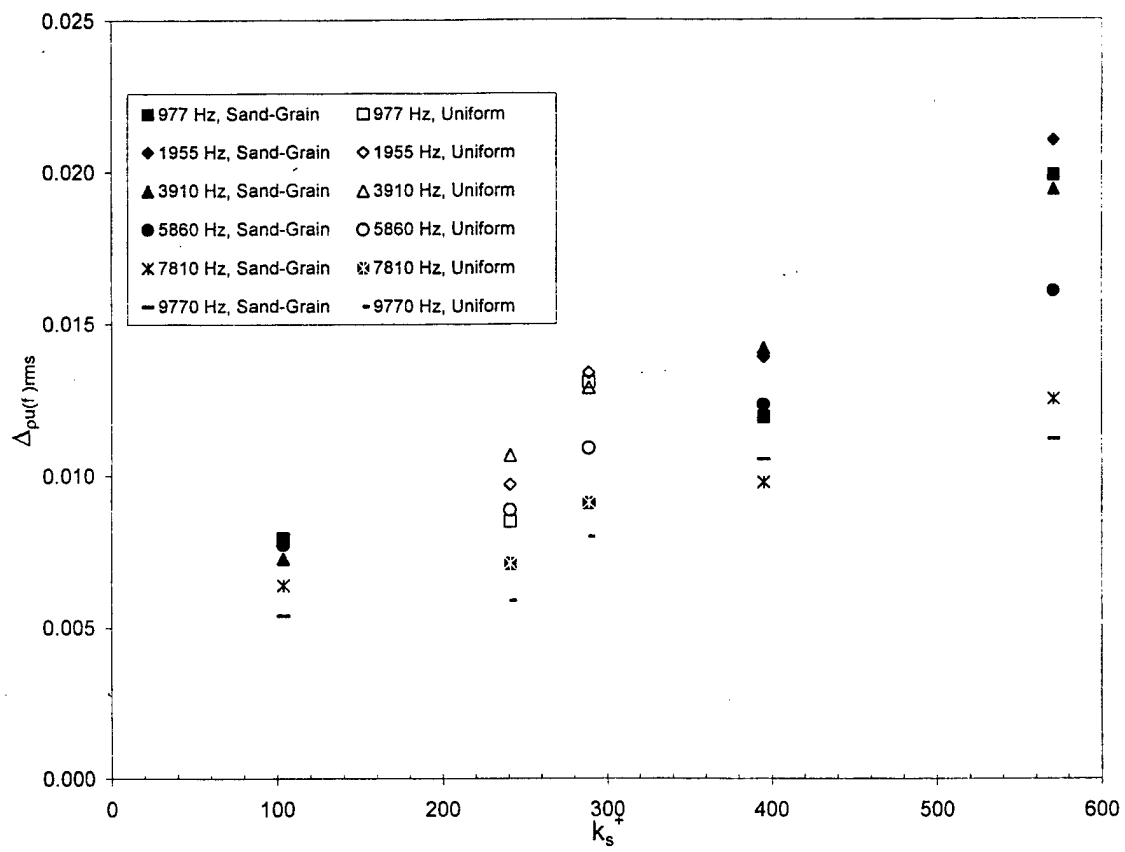


(b) $y/\delta_M = 0.5$

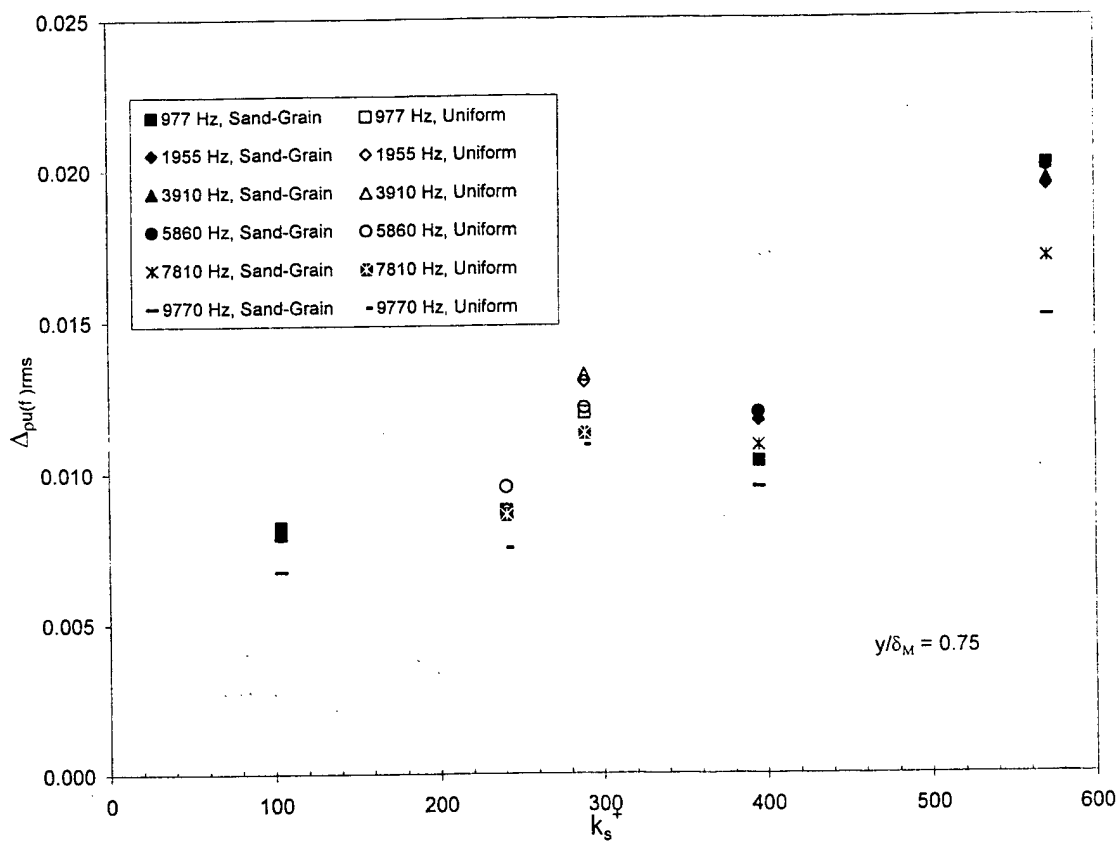


(c) $y/\delta_M = 0.75$
Figure 15 Dimensional Power Spectra



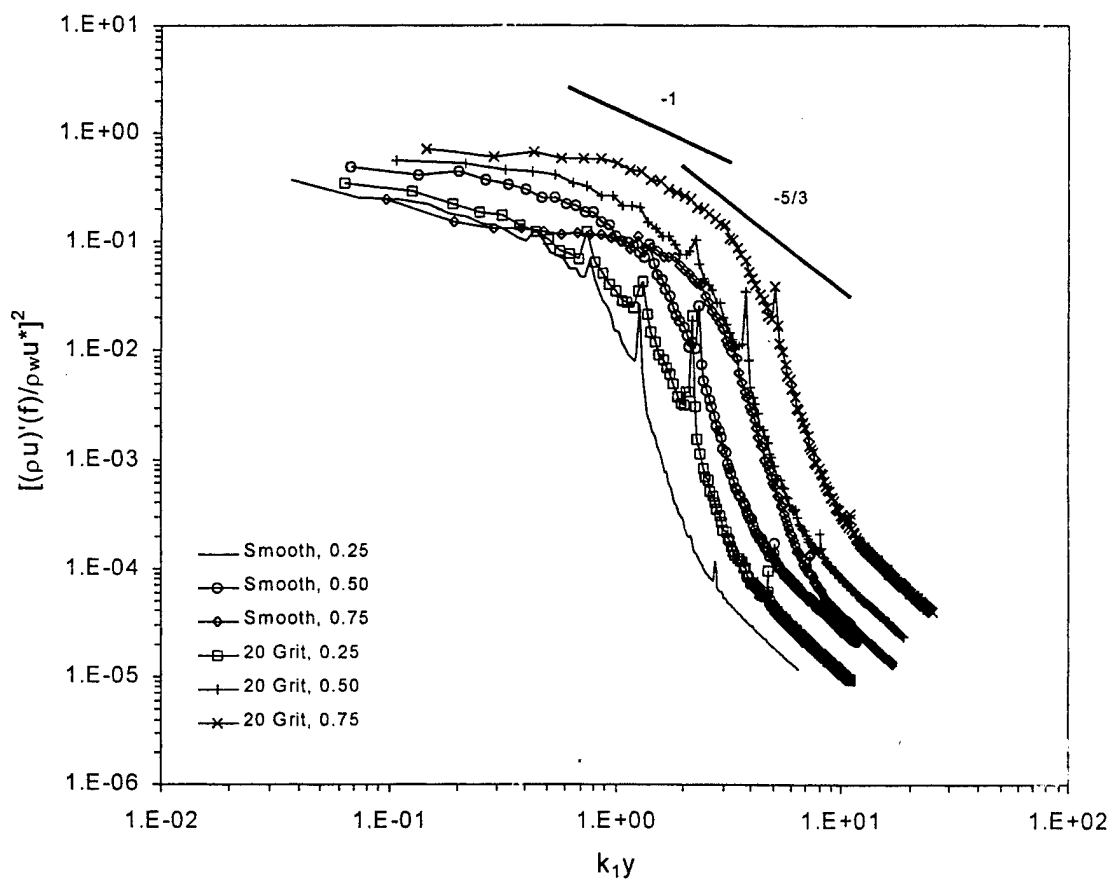


(b) $y/\delta_M = 0.5$

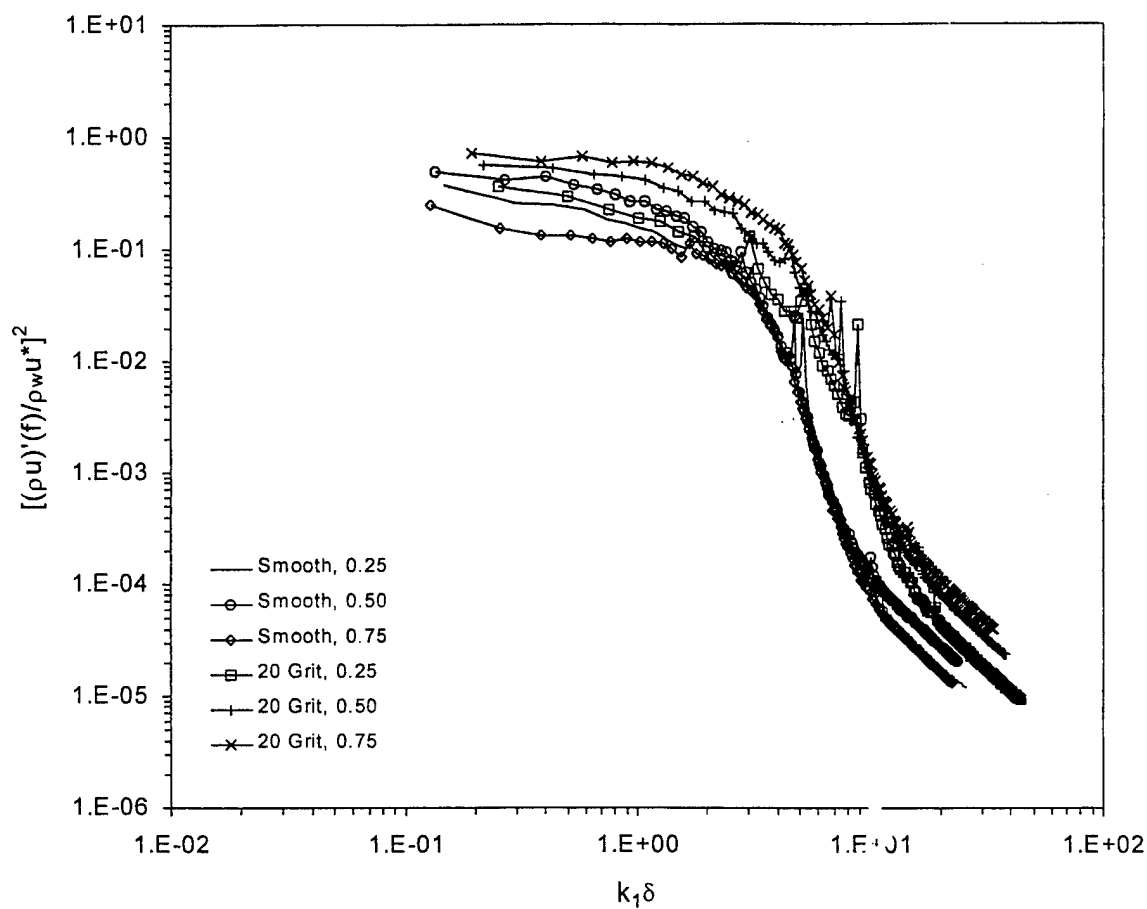


(c) $y/\delta_M = 0.75$

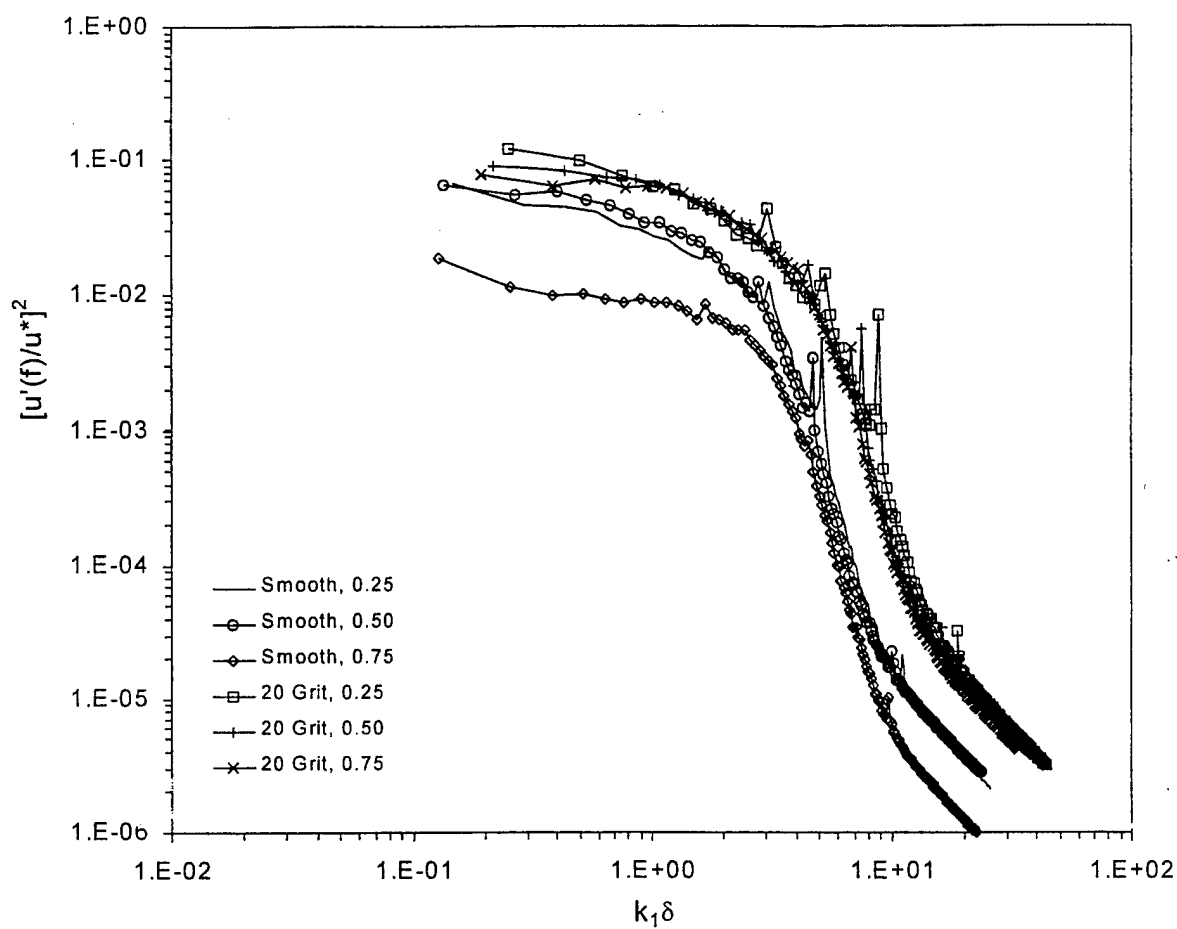
Figure 16 Power Spectra Difference versus Roughness Reynolds Number.



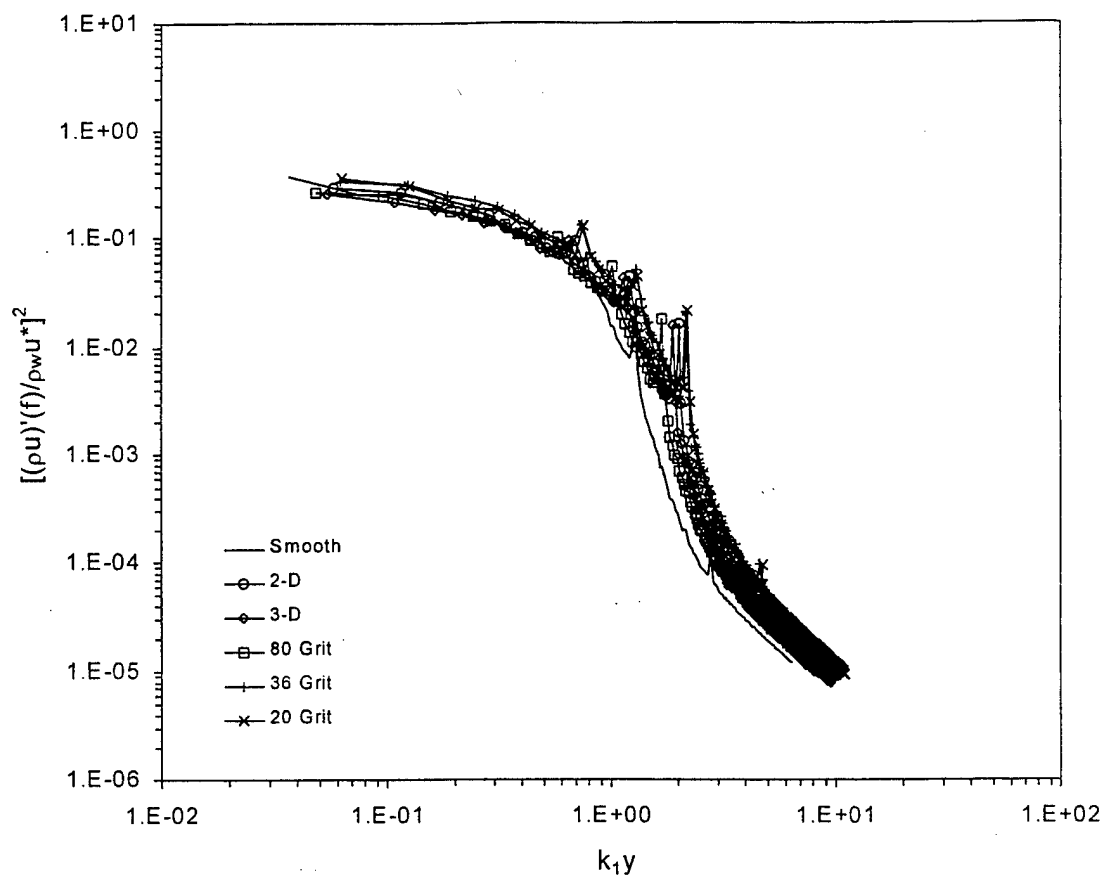
(a) Inner Scaling



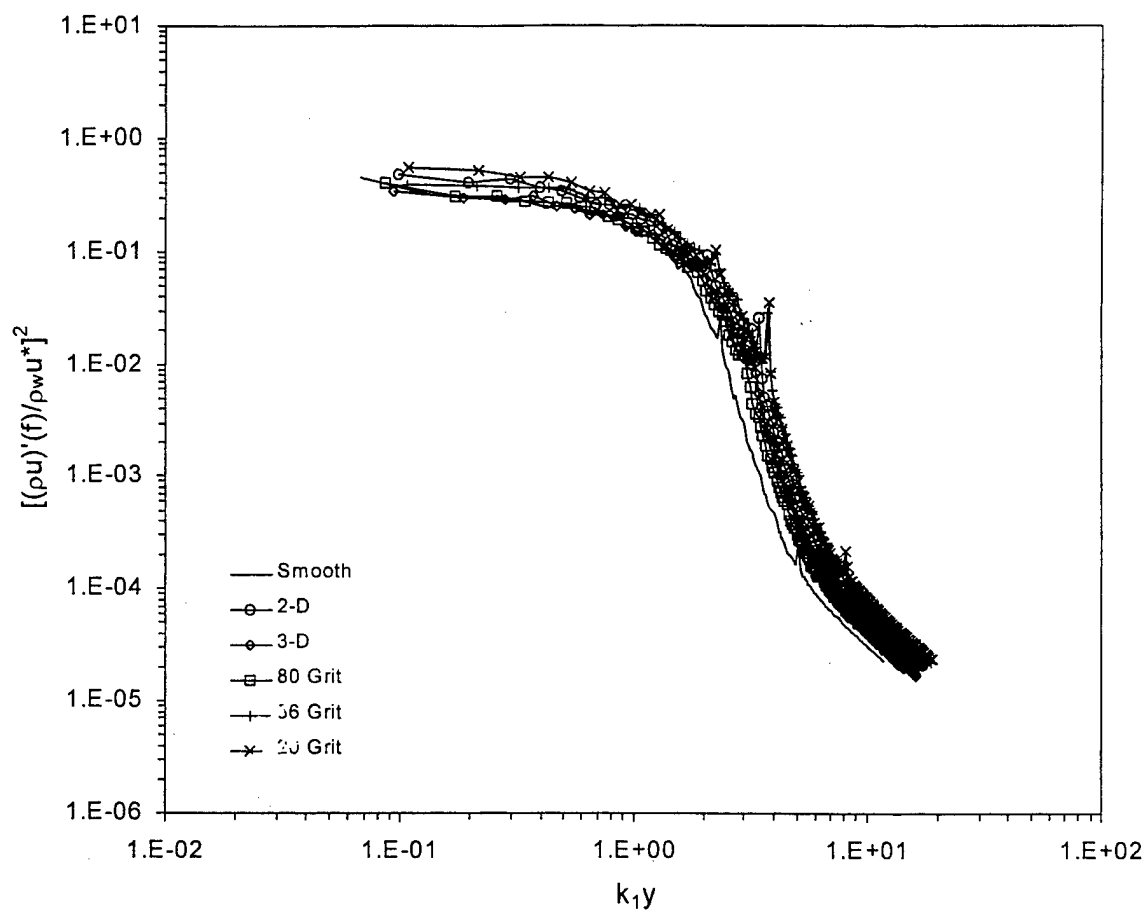
(b) Outer Scaling



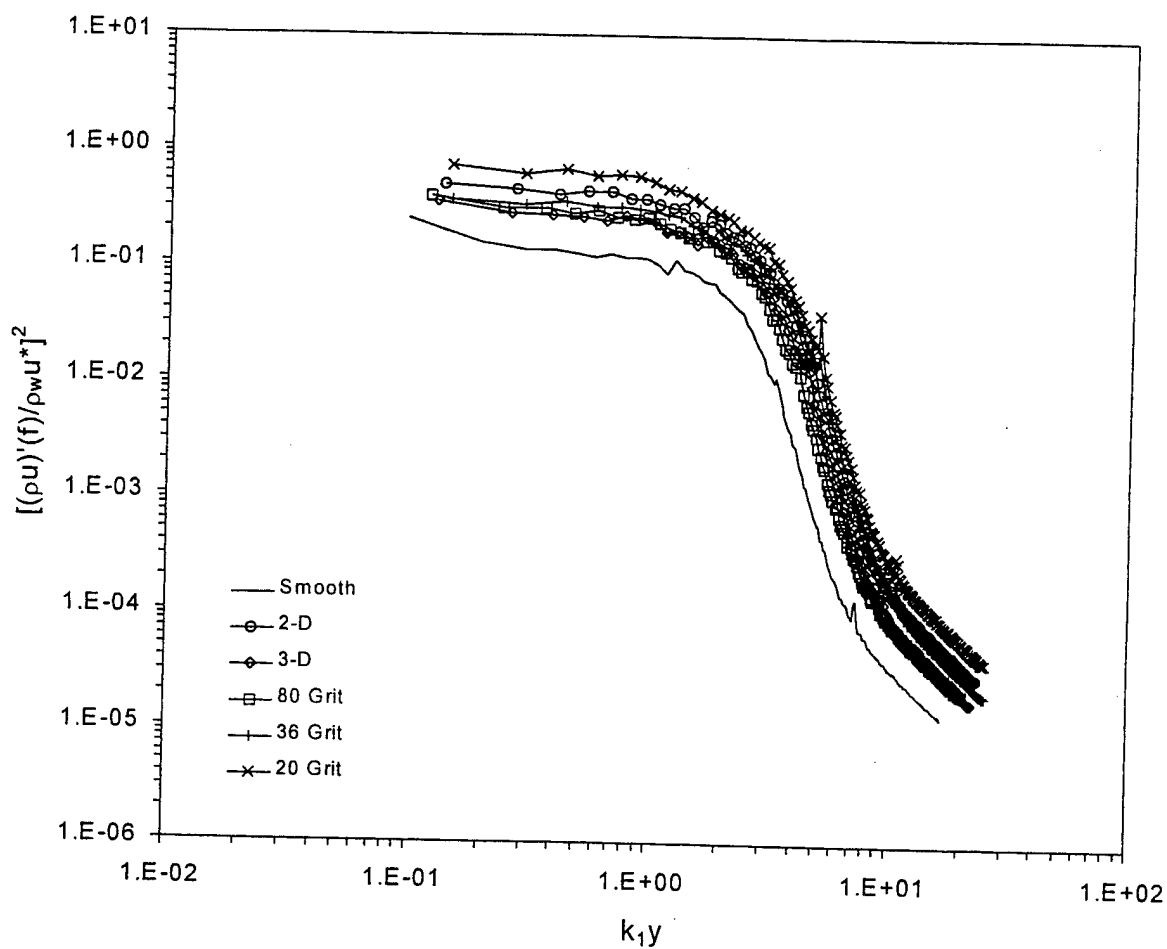
(c) Outer Scaling with the Strong Reynolds Analogy
 Figure 17 Energy Spectra Results with Inner and Outer Scaling of the frequency.



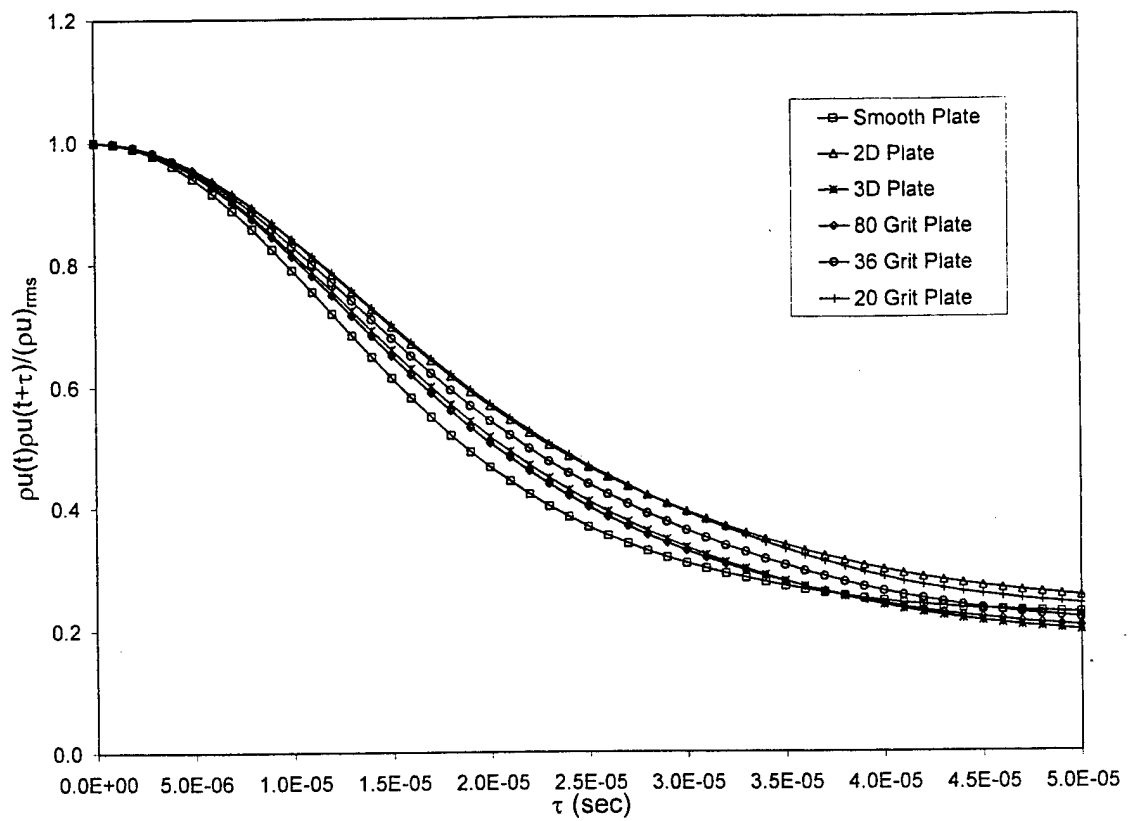
(a) $y/\delta_M = 0.25$



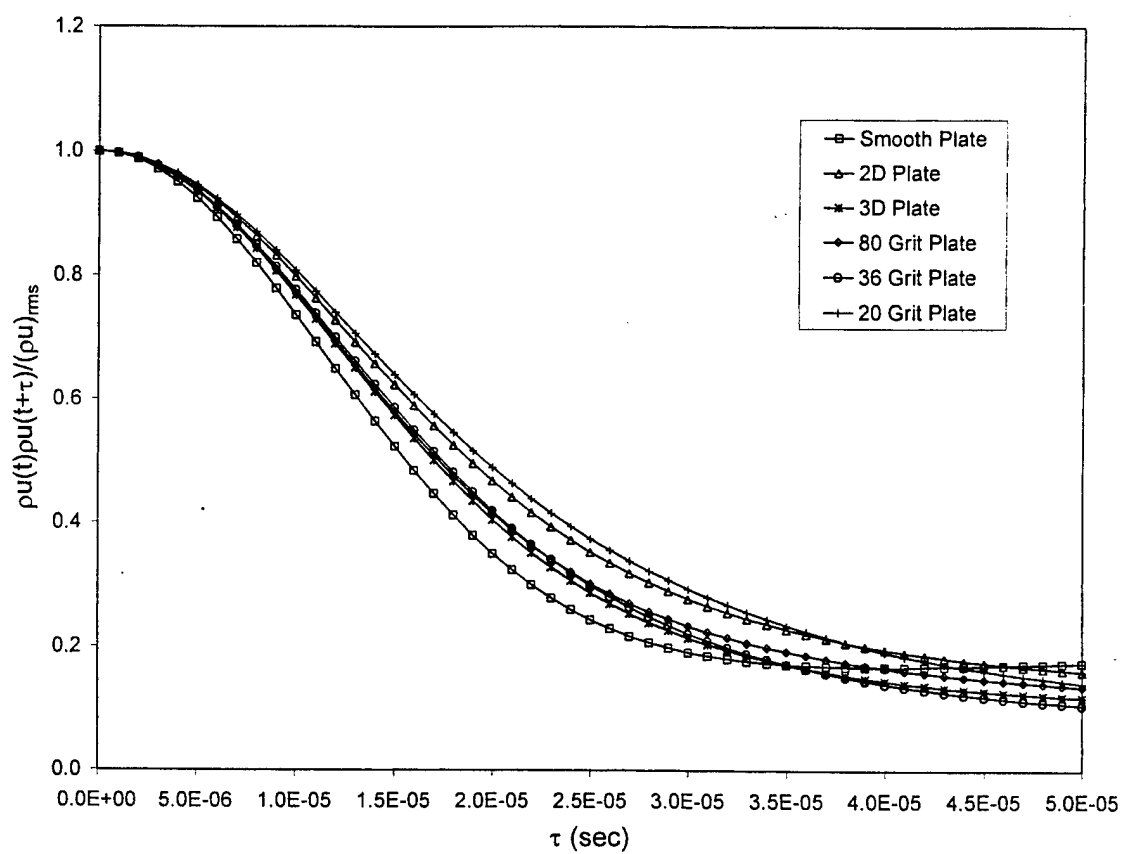
(b) $y/\delta_M = 0.50$



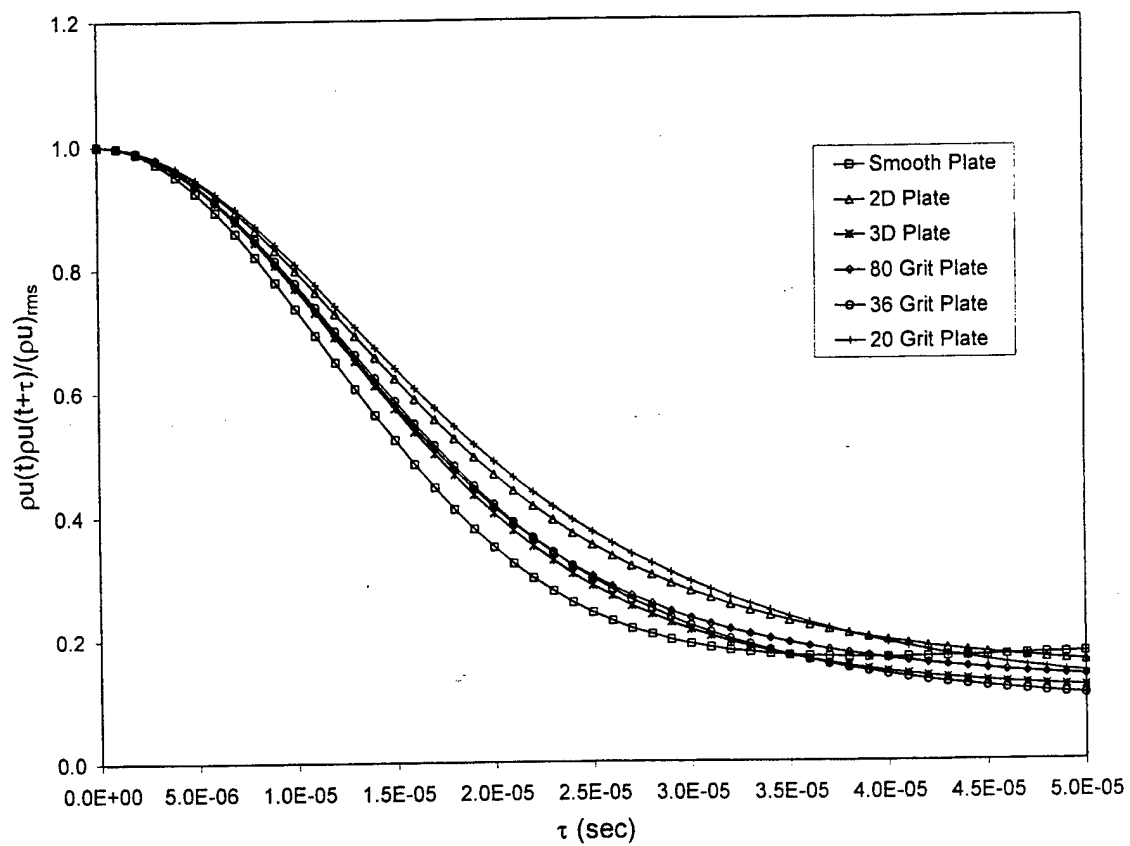
(c) $y/\delta_M = 0.75$
Figure 18 Energy Spectra Results with Inner Scaling.



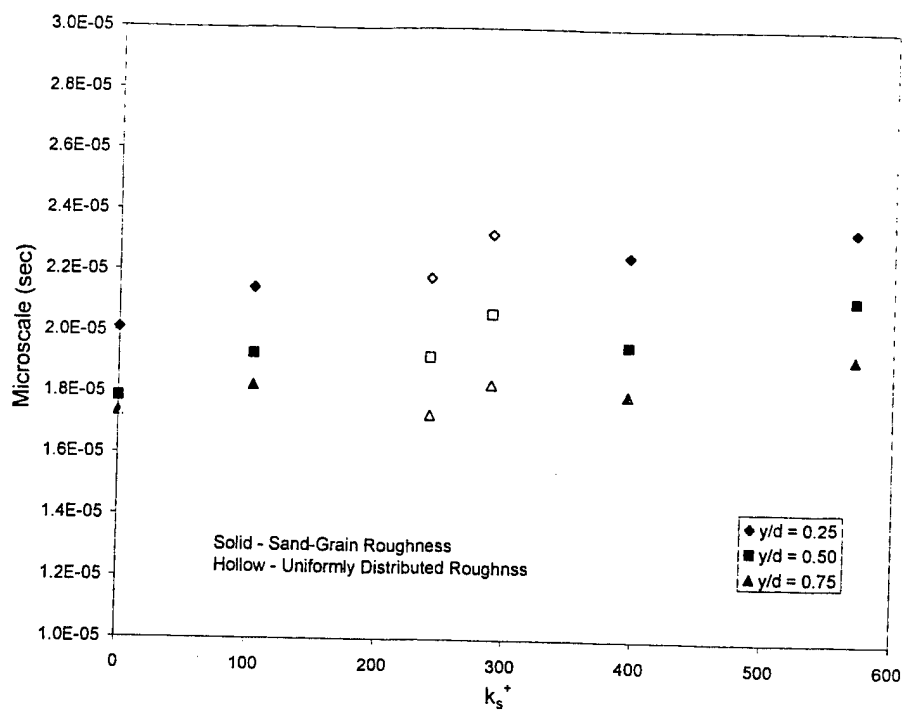
(a) $y/\delta_M = 0.25$



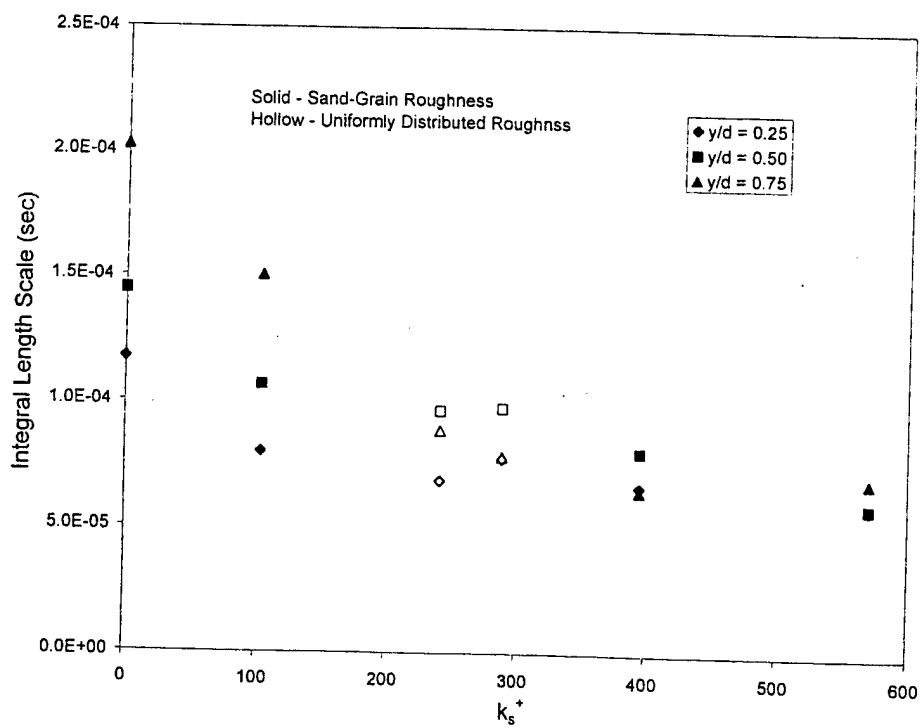
(b) $y/\delta_M = 0.50$



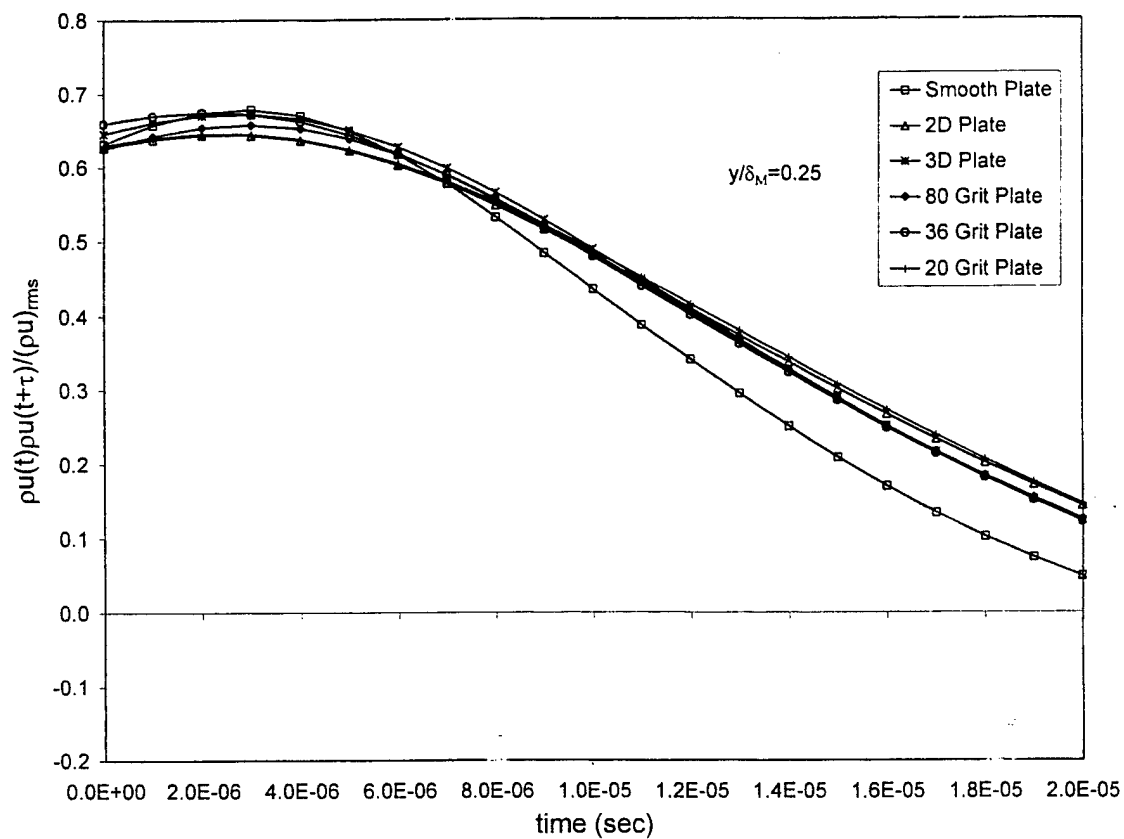
(c) $y/\delta_M = 0.75$
Figure 19 Autocorrelation Functions.



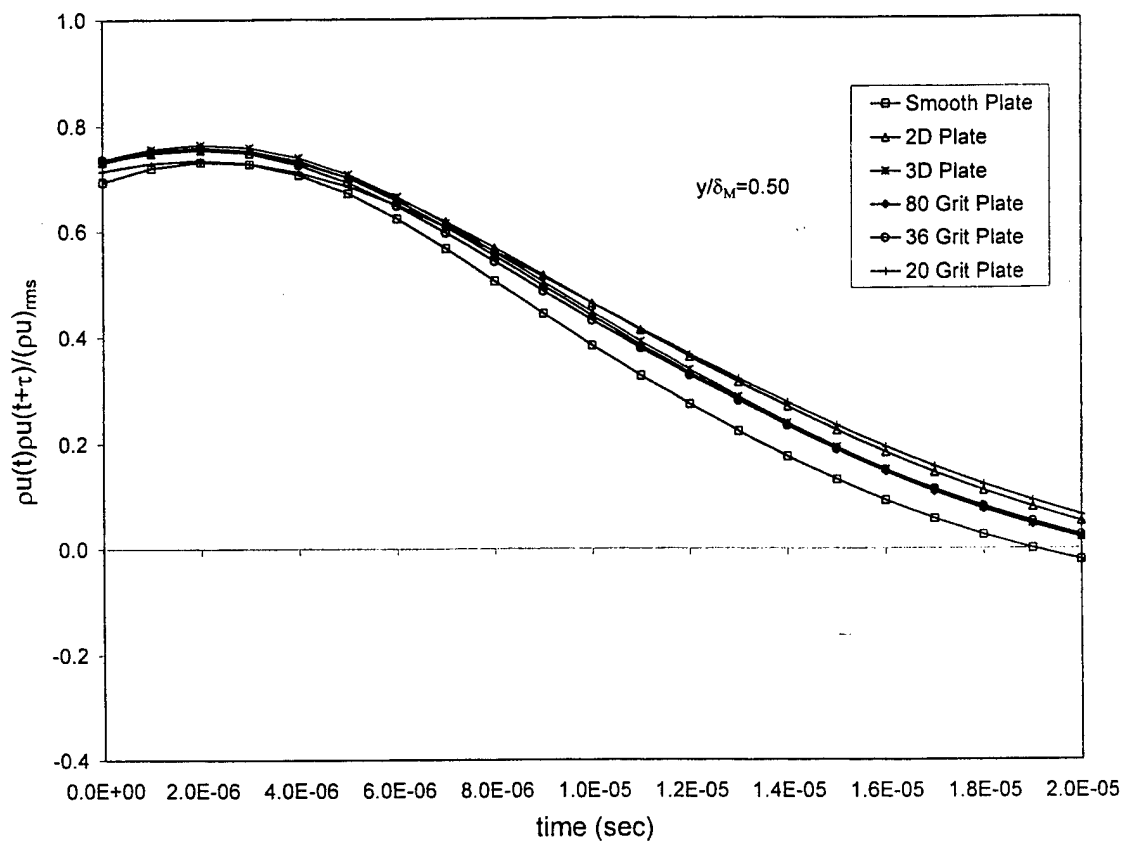
(a) Micro-scale



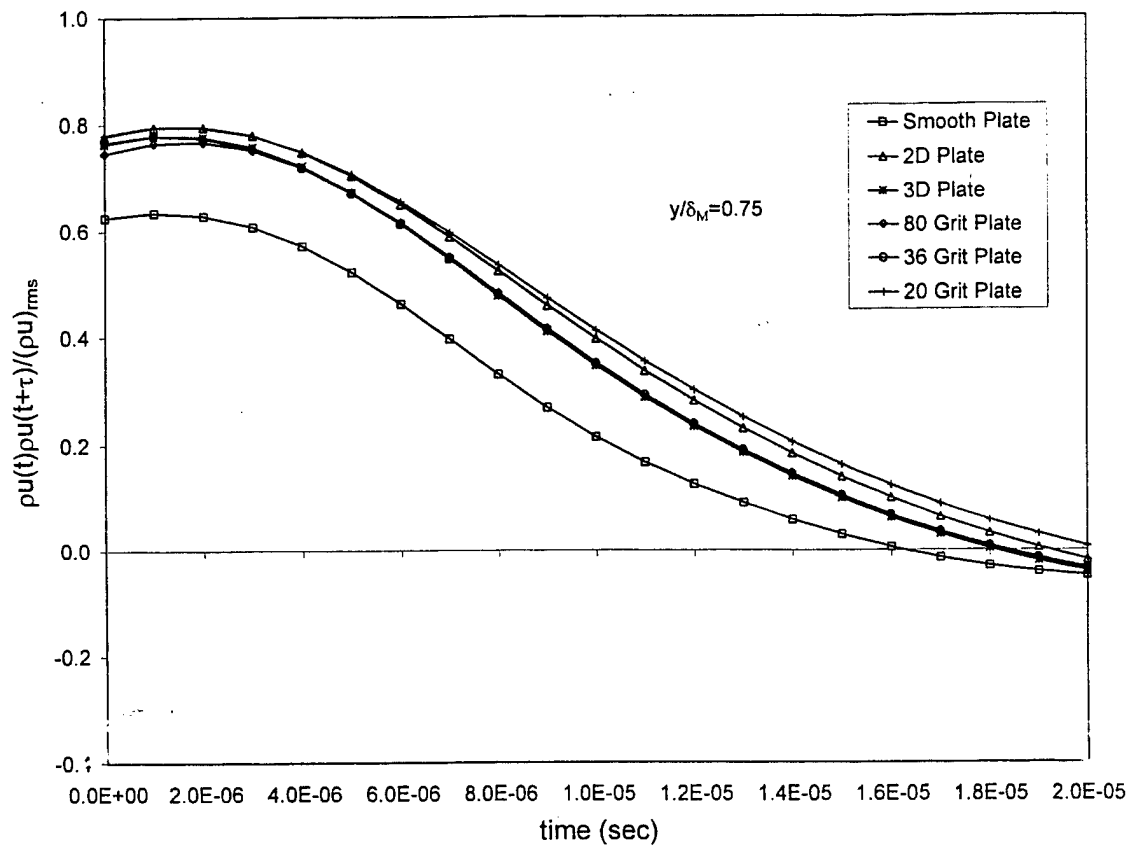
(a) Integral-Scale
Figure 20 Time-Scales.



(a) $y/\delta_M = 0.25$



(b) $y/\delta_M = 0.50$



(c) $y/\delta_M = 0.75$
Fig. 21 Parallel-Wire Cross-Correlation Traces.

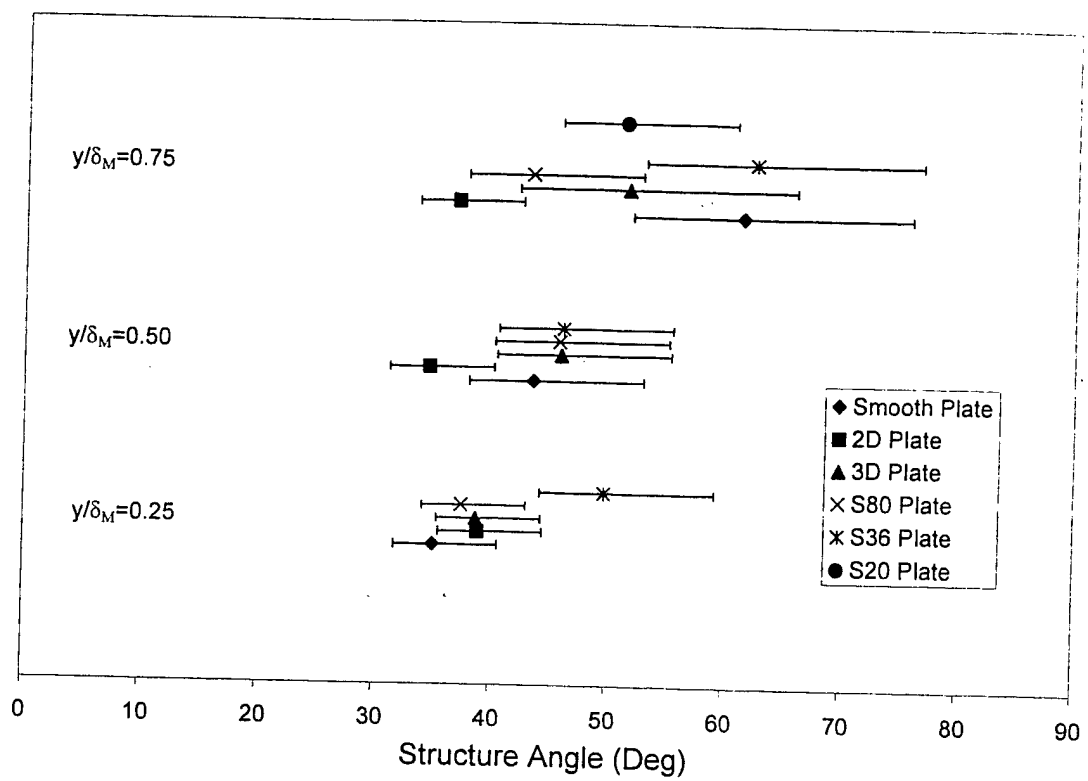
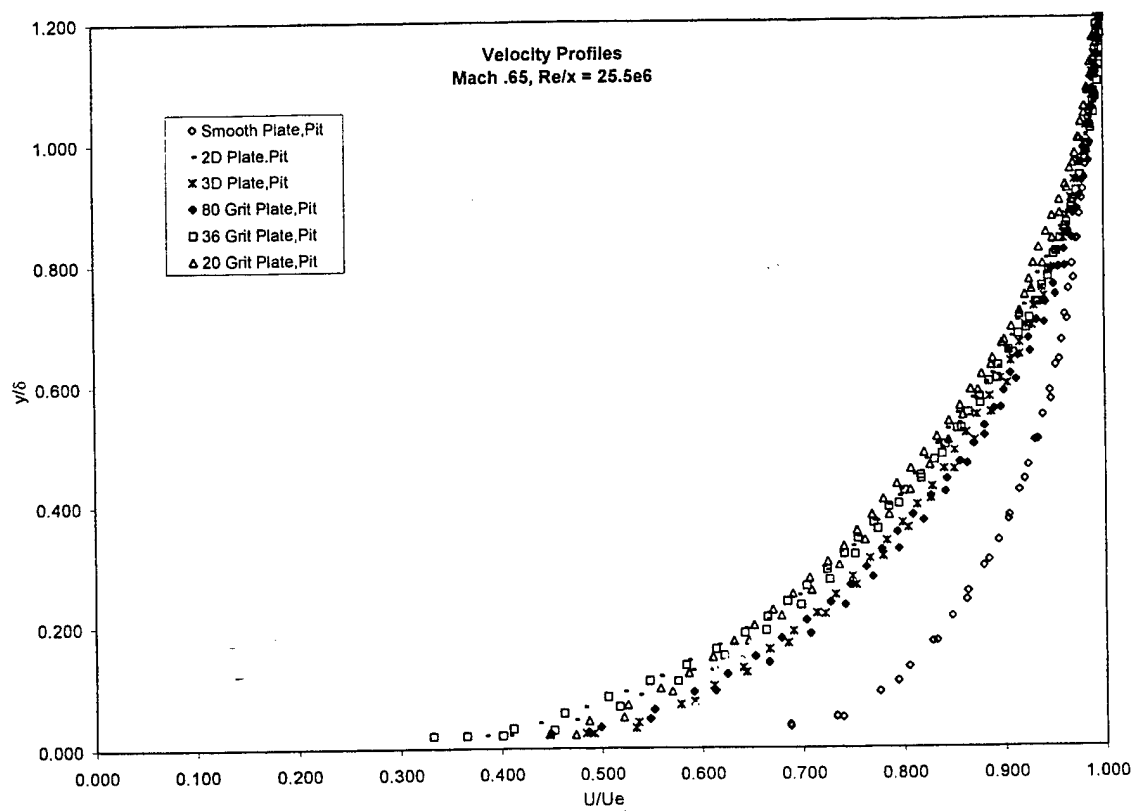
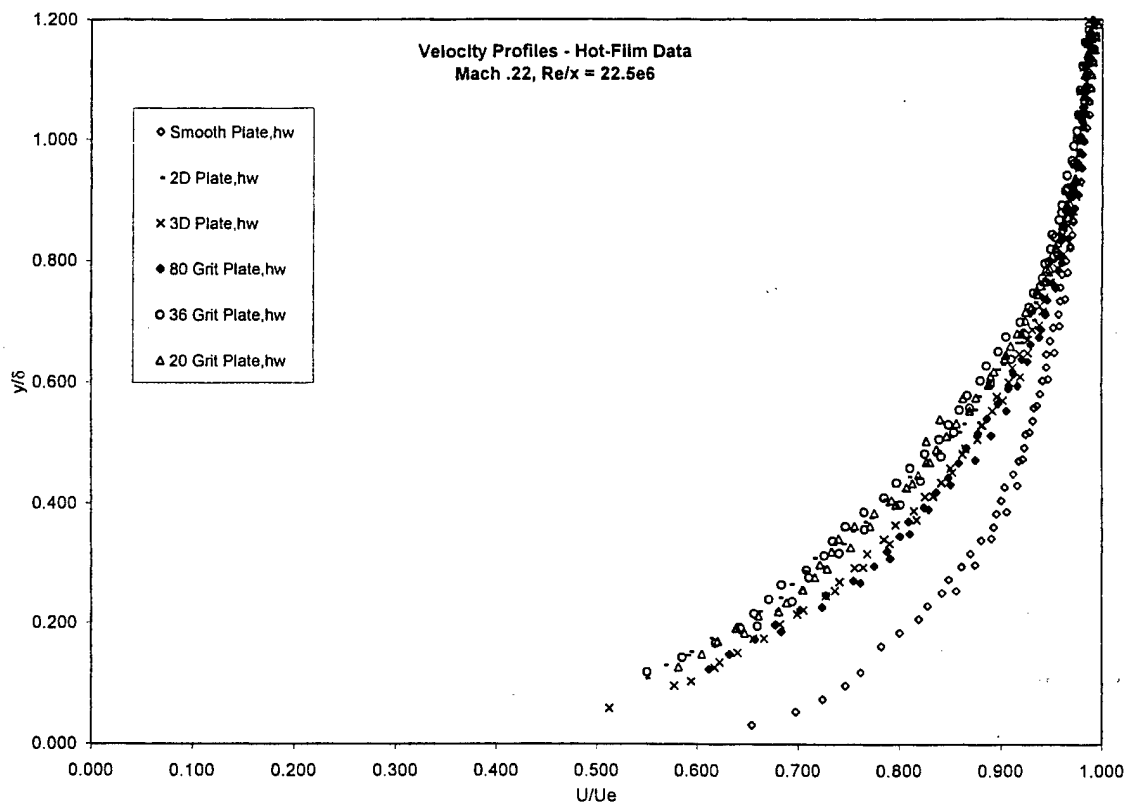


Fig. 22 Structure Angle



(a) $M = 0.65$ (Pitot Probe)



(b) $M = 0.22$ (Hot-Wire Probe)
Fig. 23 Velocity Profiles

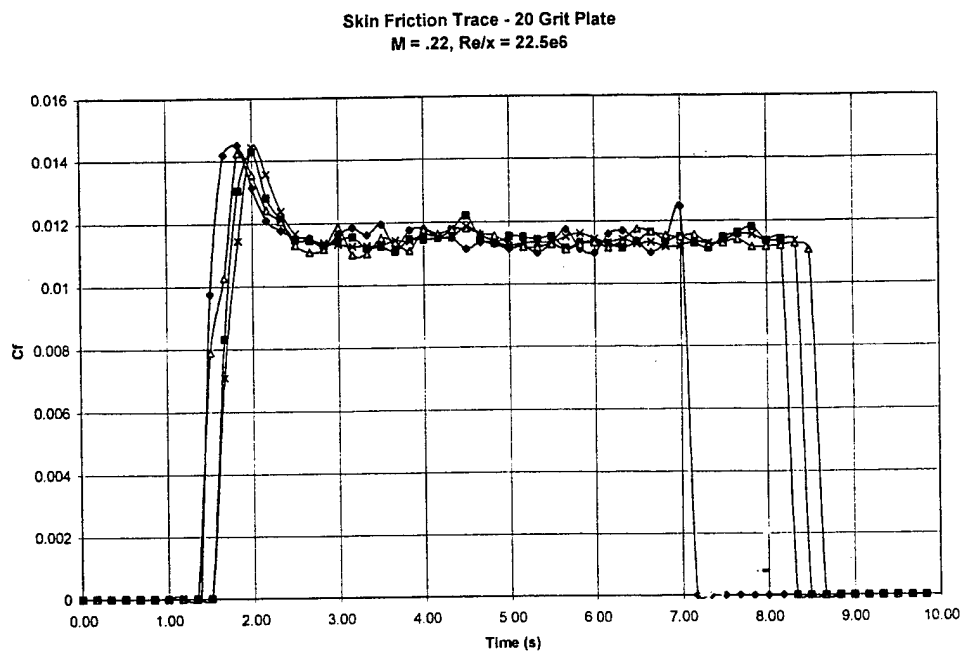
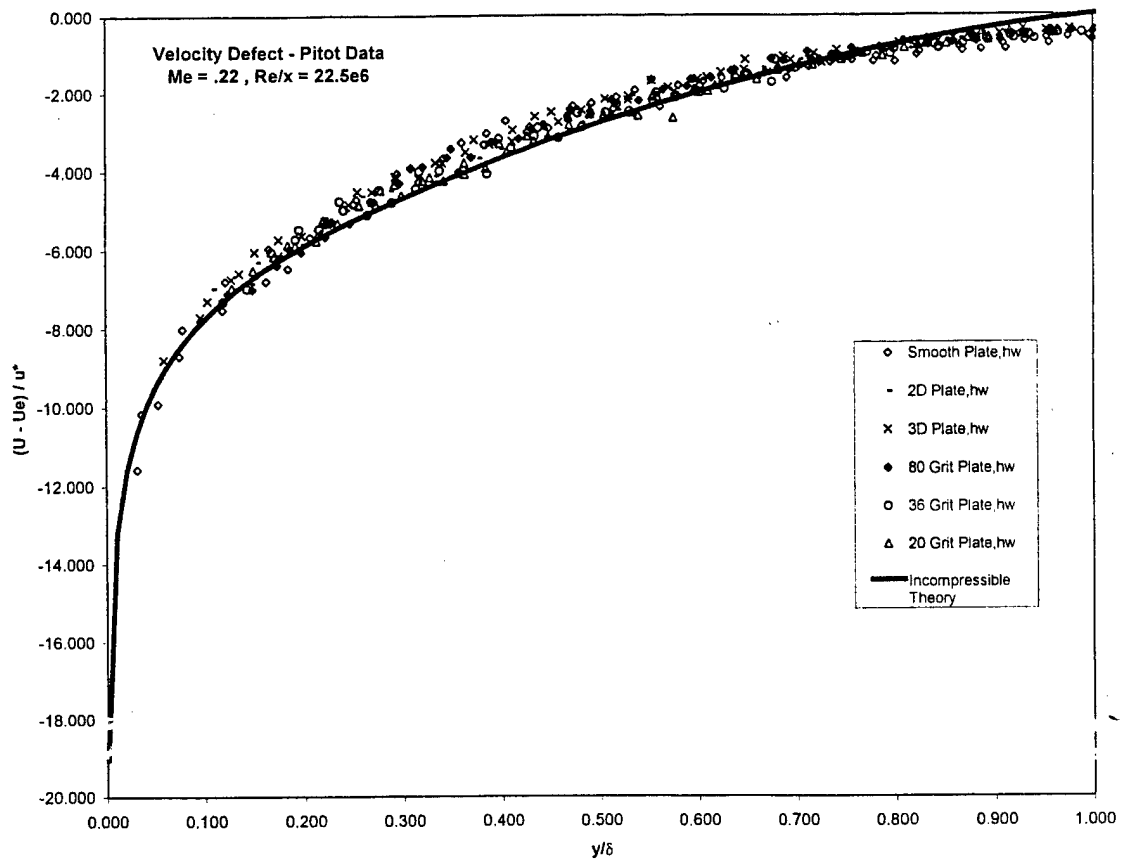
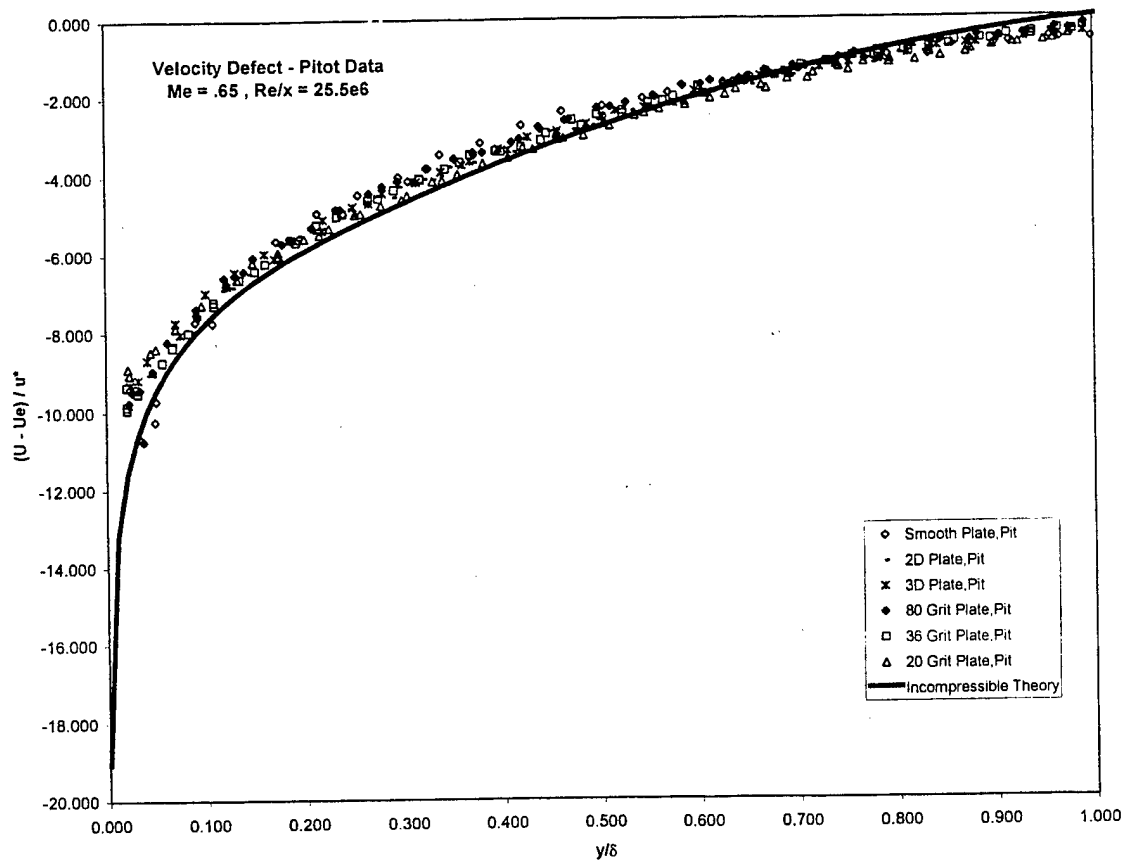


Fig. 24 Example Skin Friction Gage Traces (20 Grit Plate, $M = 0.22$)

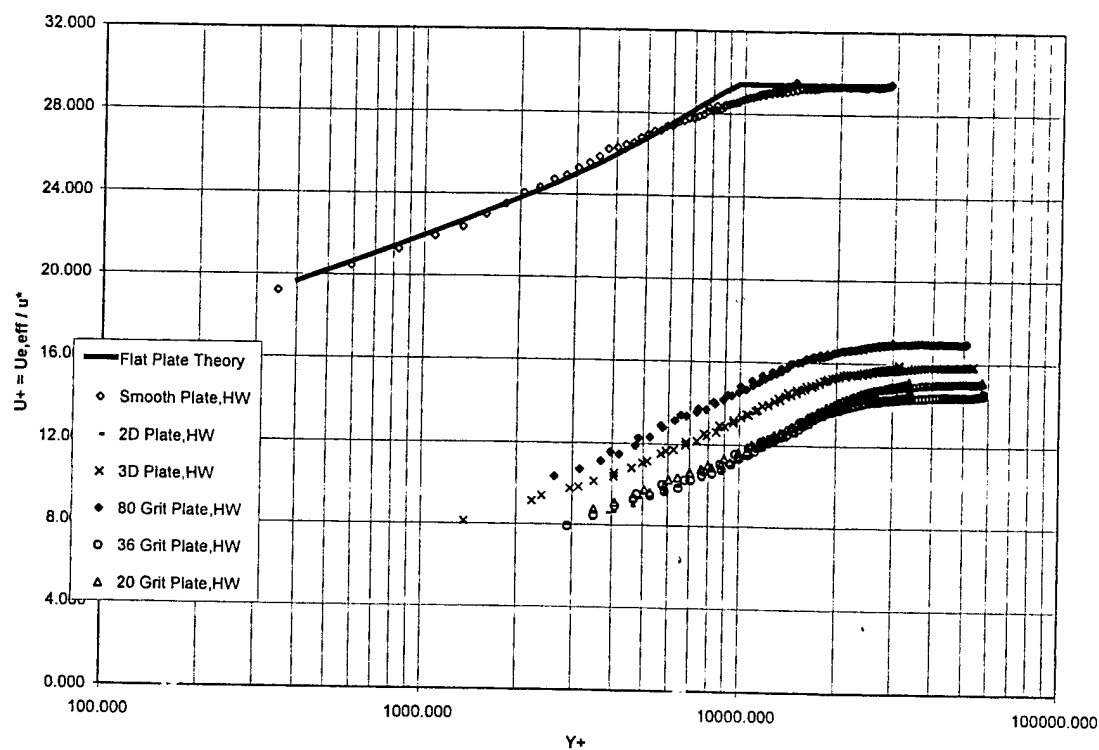


(a) $M = 0.22$

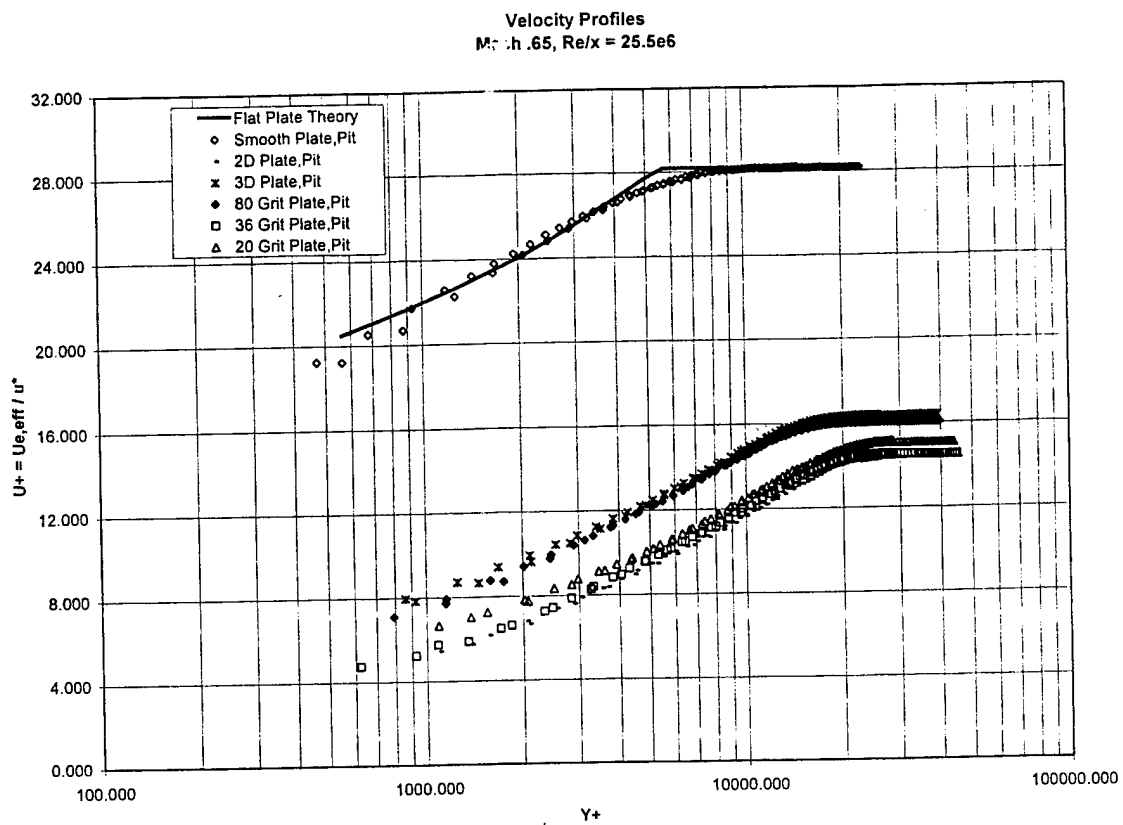


(b) $M = 0.65$
Fig. 25 Defect Law Plots

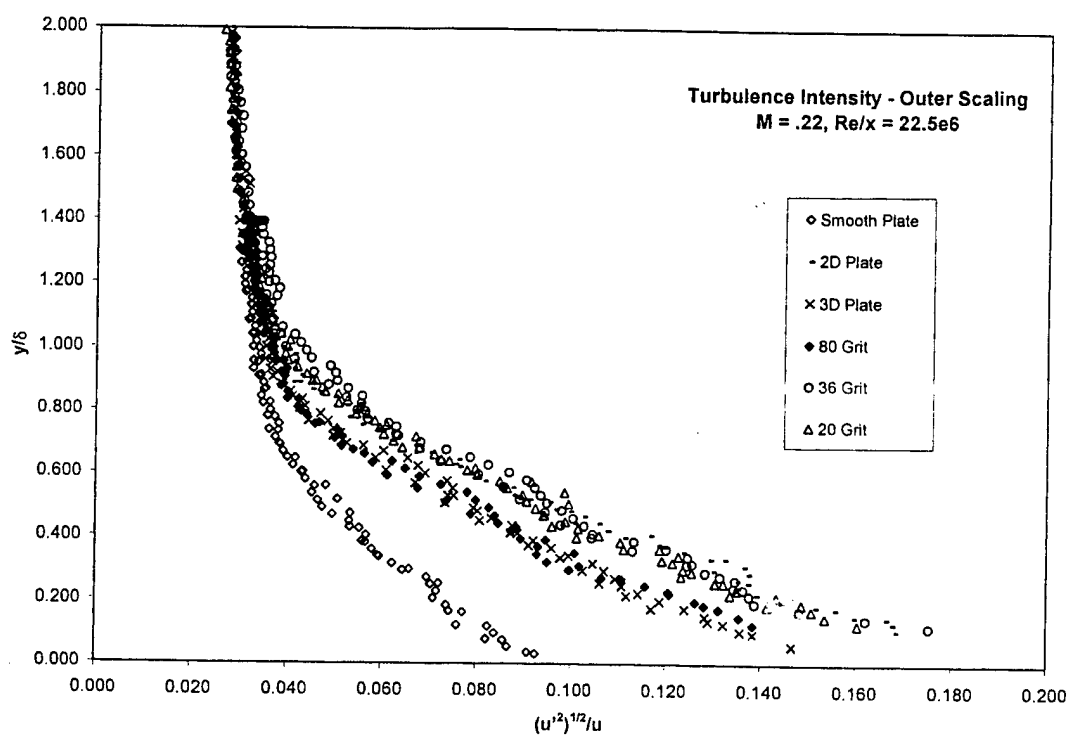
Law of the Wall - Hot Film
Mach .22, $Re/x = 22.5e6$



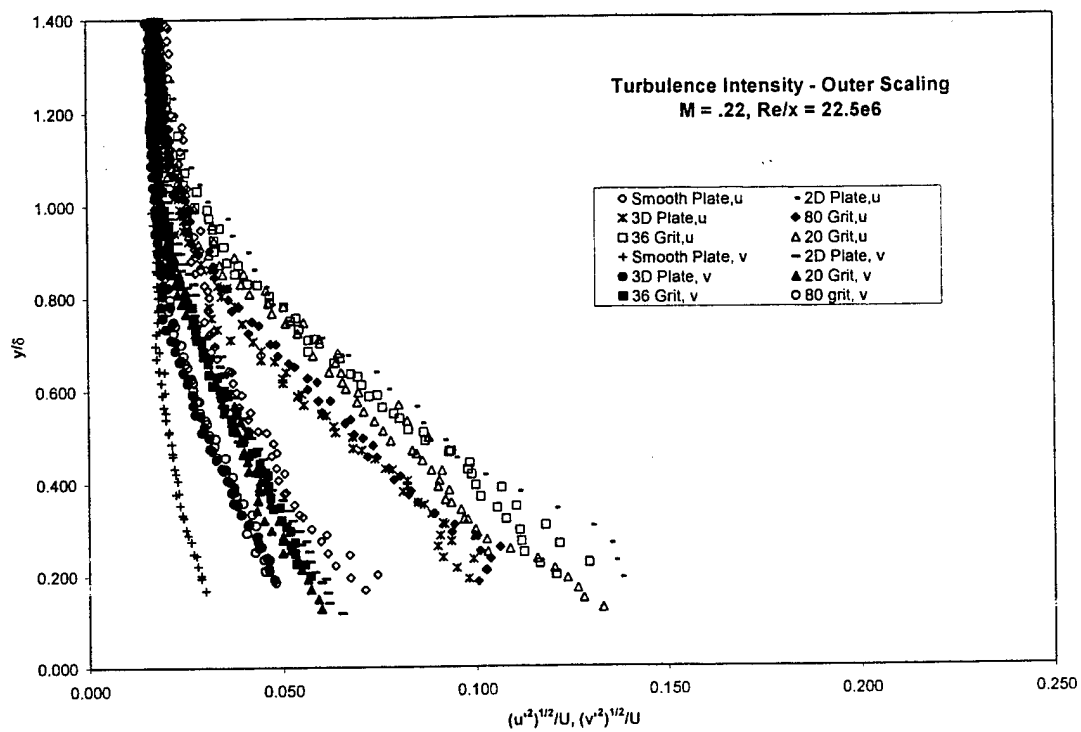
(a) $M = 0.22$



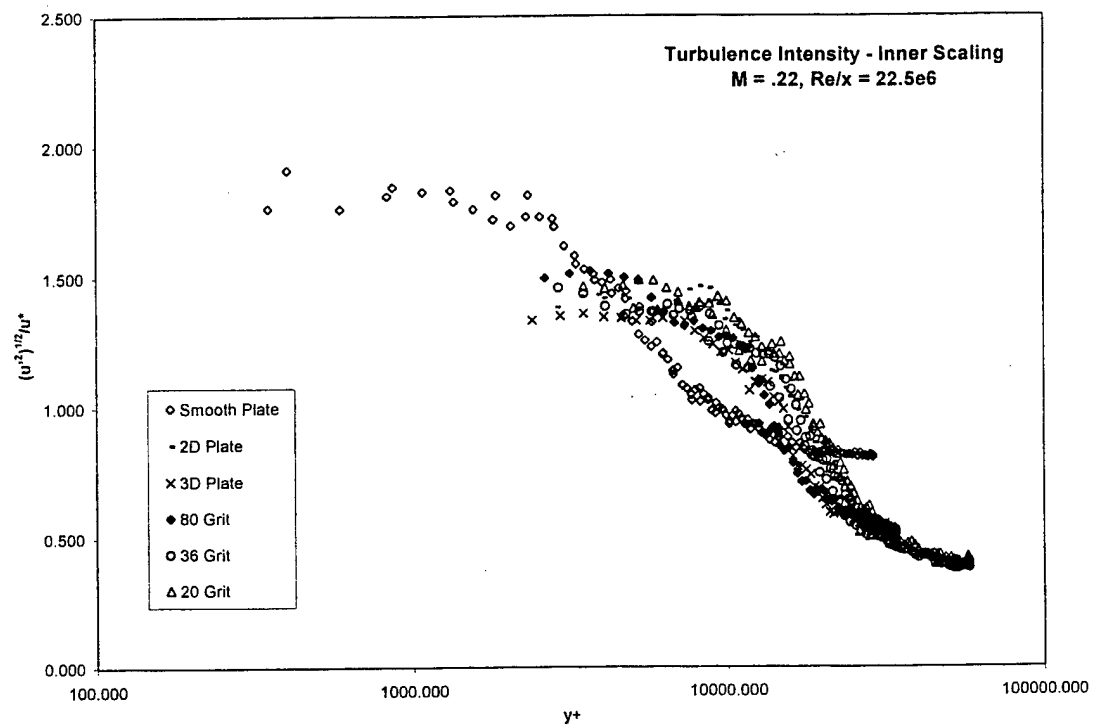
(b) $M = 0.65$
Fig. 26 Law of the Wall Plots



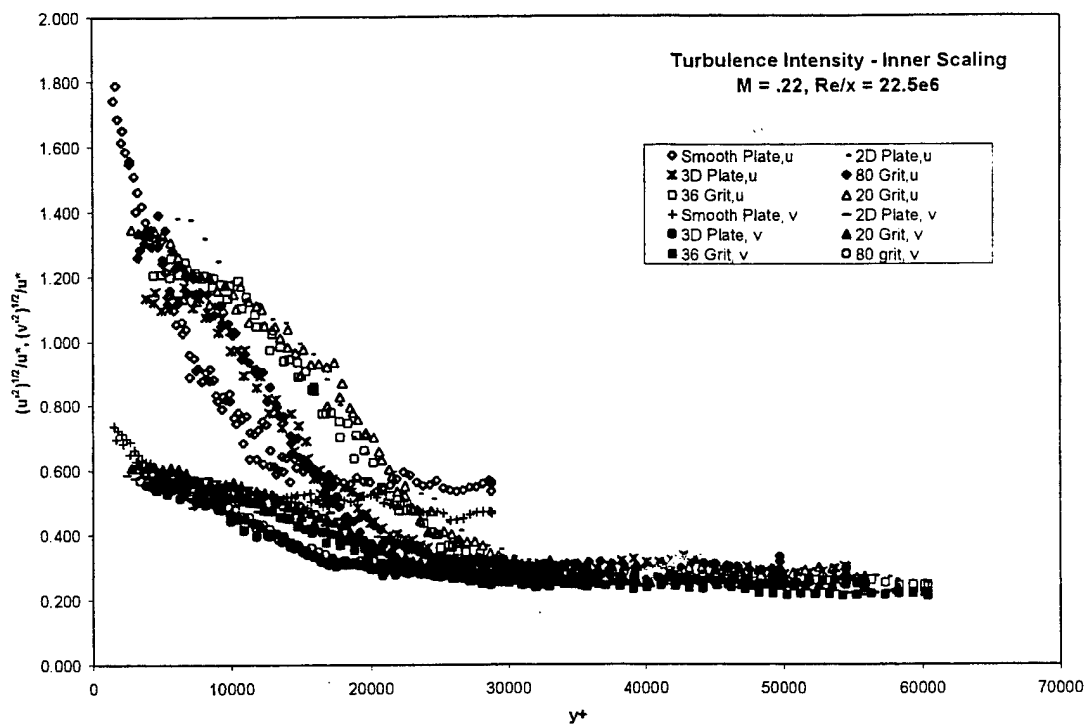
(a) Outer Variable Scaling (Normal-Film Probe)



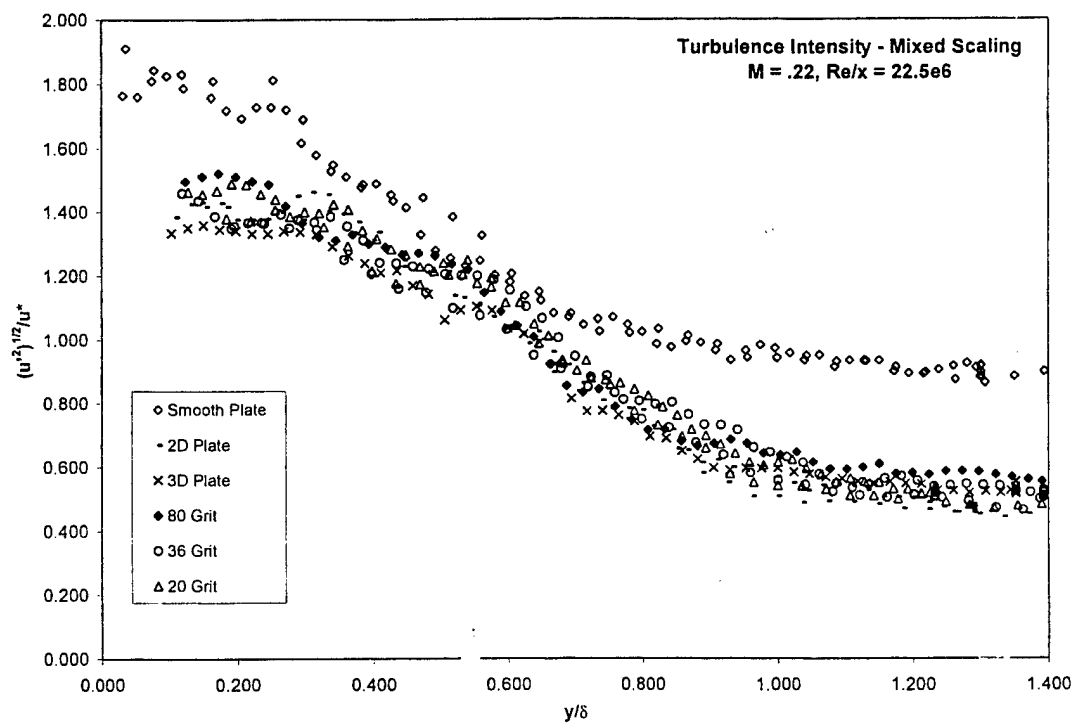
(b) Outer Variable Scaling (Cross-Film Probe)



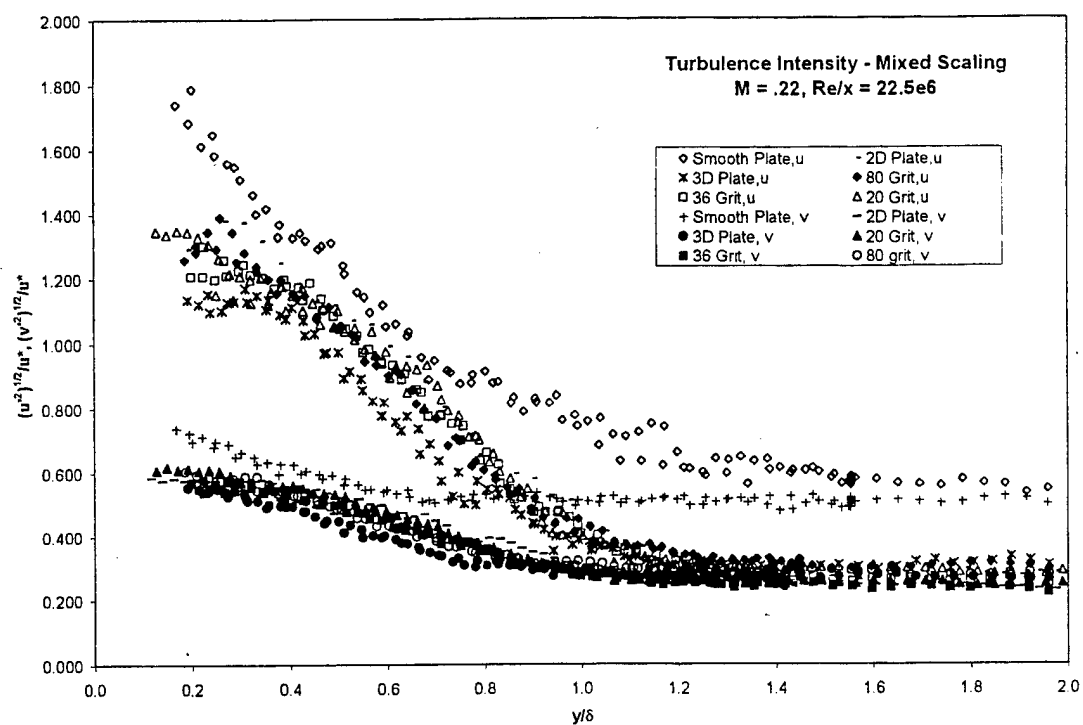
(c) Inner Variable Scaling (Normal-Film Probe)



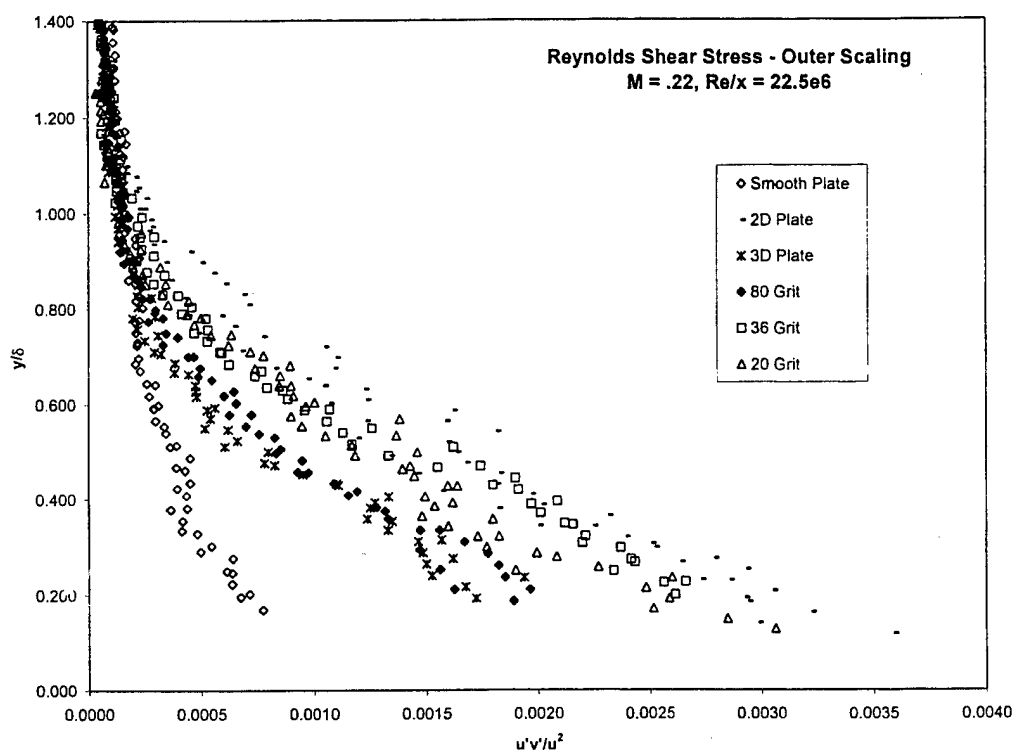
(d) Inner Variable Scaling (Cross-Film Probe)



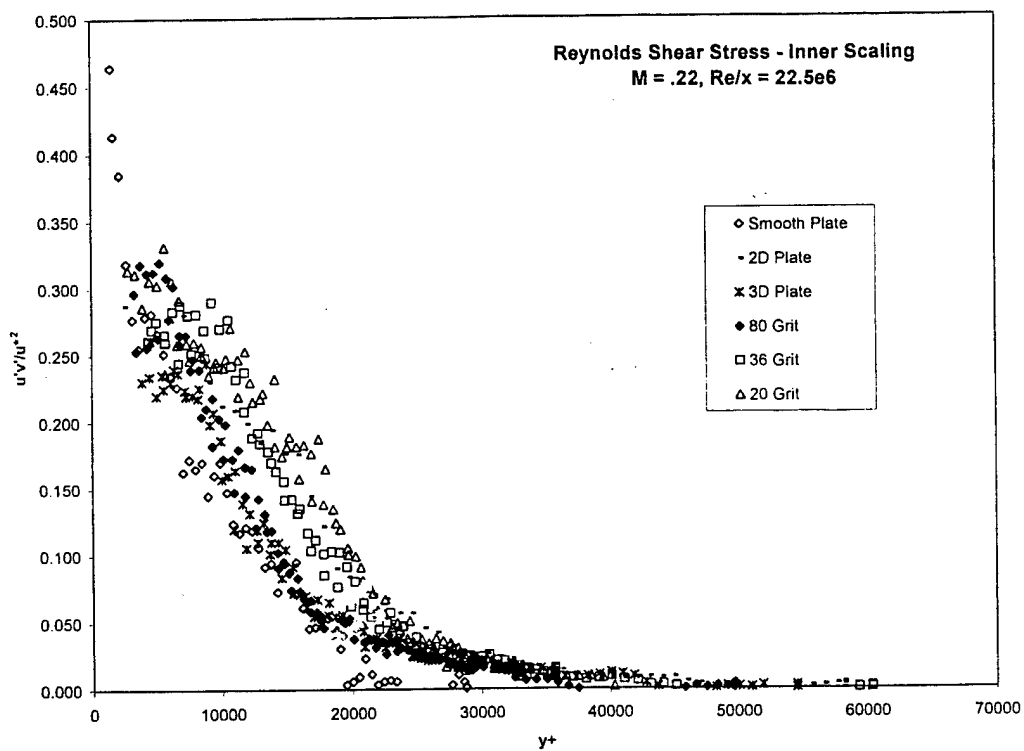
(e) Mixed Variable Scaling (Normal-Film Probe)



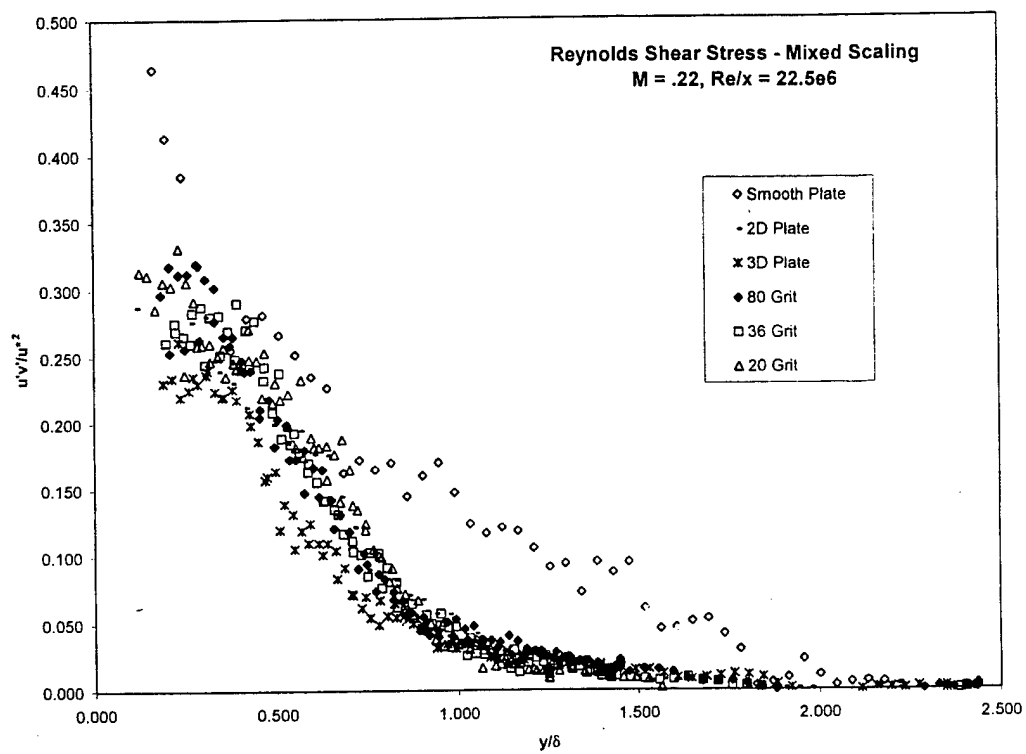
(f) Mixed Variable Scaling (Cross-Film Probe)
Fig. 27 Turbulence Intensity Results (M = 0.22)



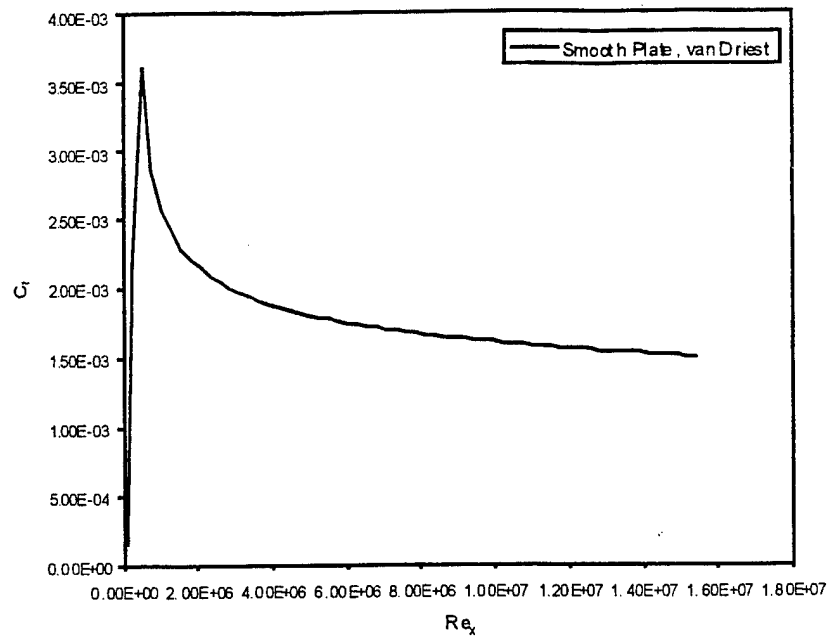
(a) Outer Variable Scaling



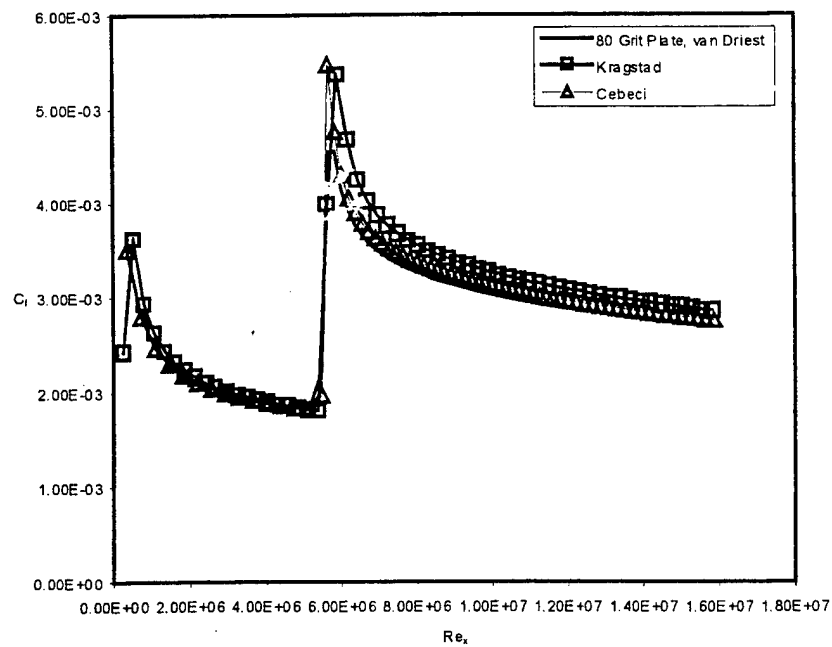
(b) Inner Variable Scaling



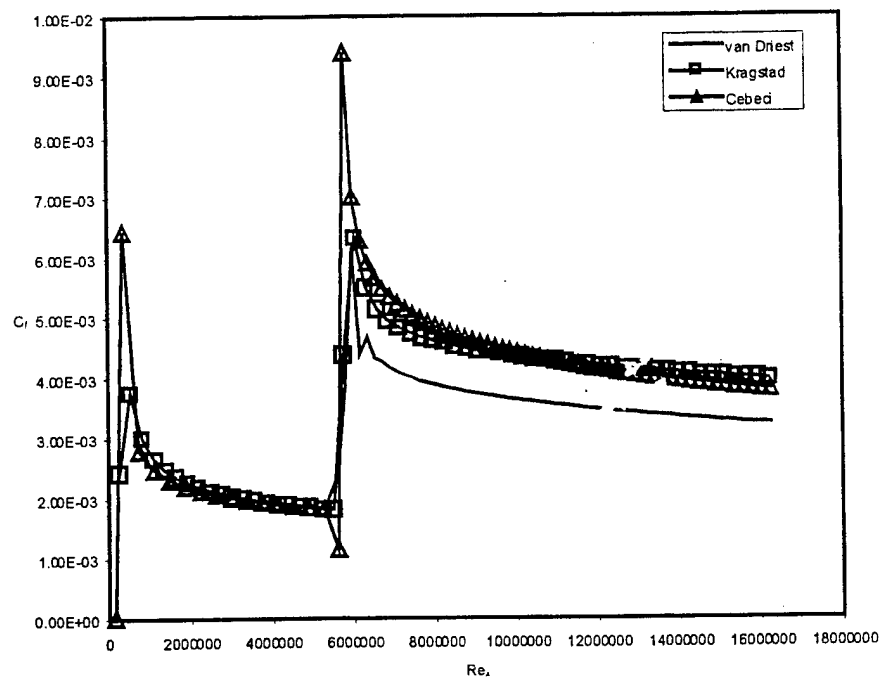
(c) Mixed Variable Scaling
Fig. 28 Reynolds Shear Stress Profiles (M = 0.22, Cross-Film Probe)



(a) Smooth Plate

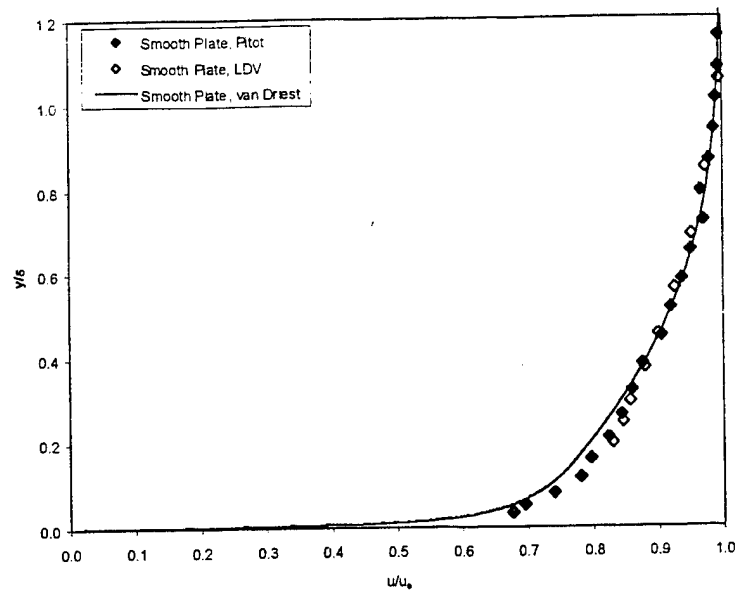


(b) 80 Grit Plate

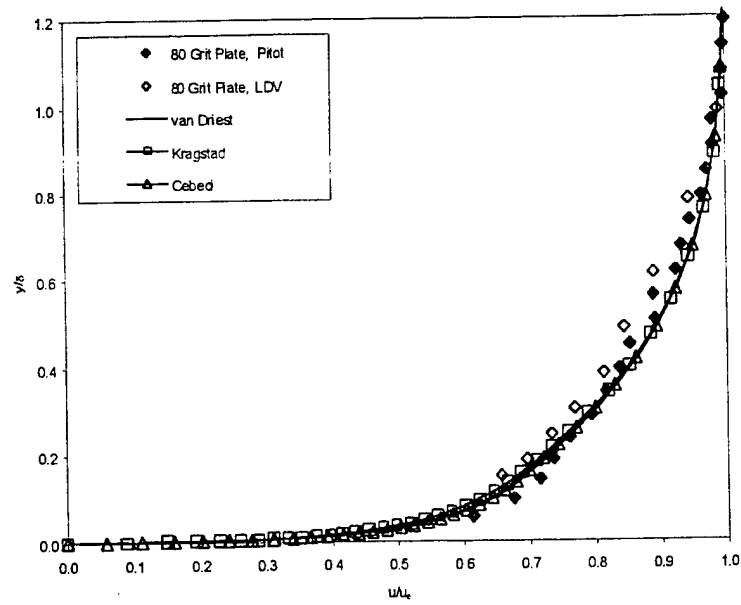


(c) 20 Grit

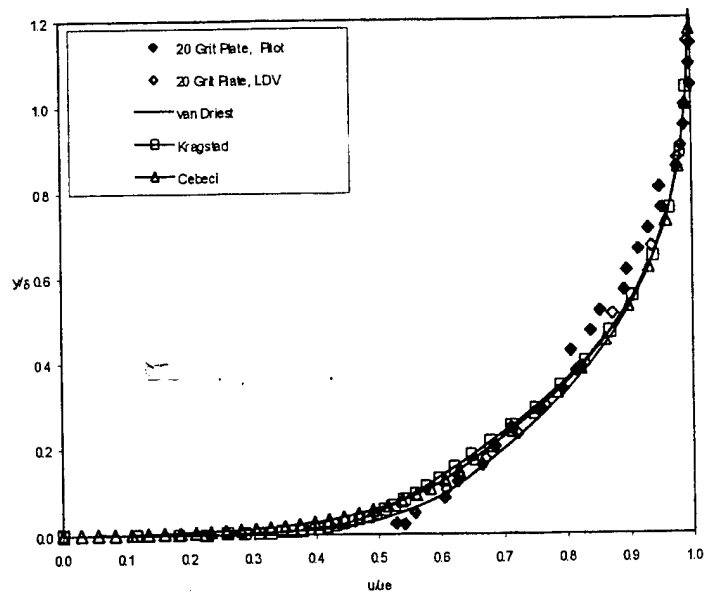
Fig. 29 Representative skin friction versus local Reynolds number based on x-location.



(a) Smooth Plate



(b) 80 Grit Plate



(c) 20 Grit Plate

Fig. 30 Representative velocity profiles, with comparison experimental data at Mach 2.8.

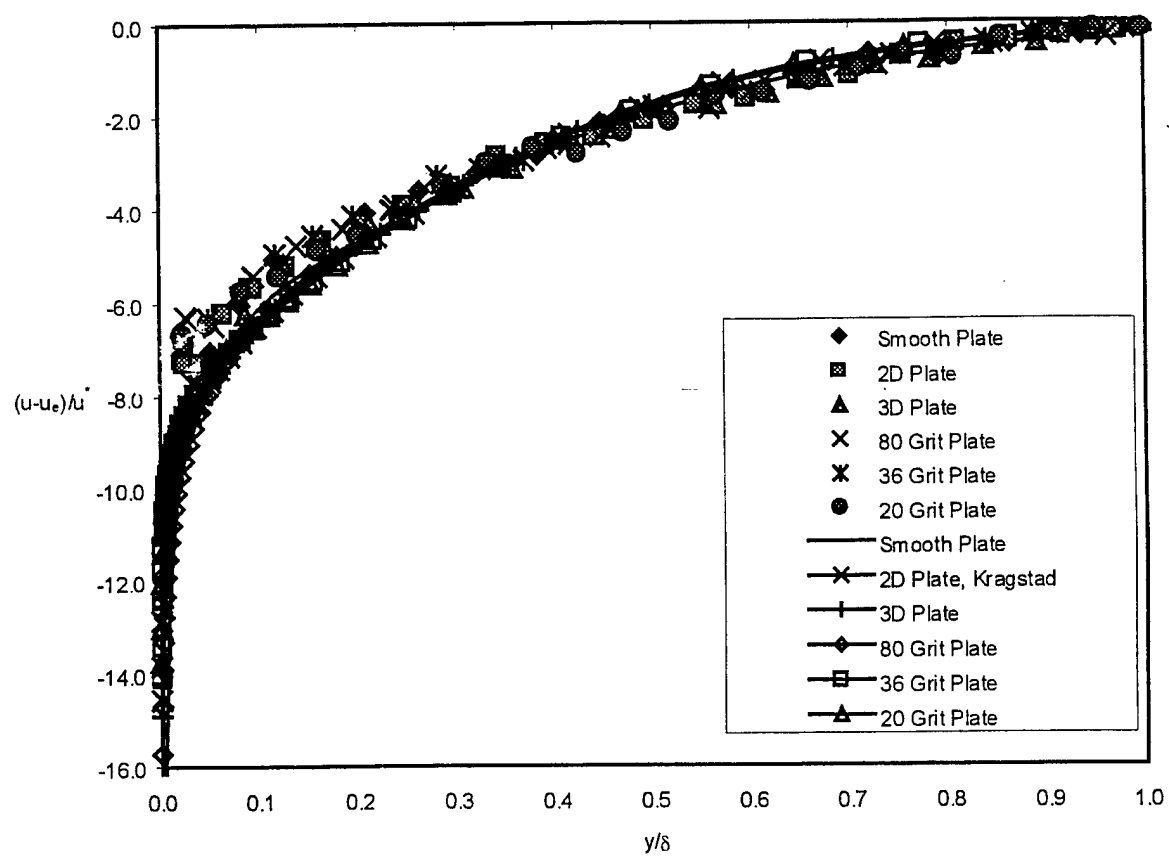
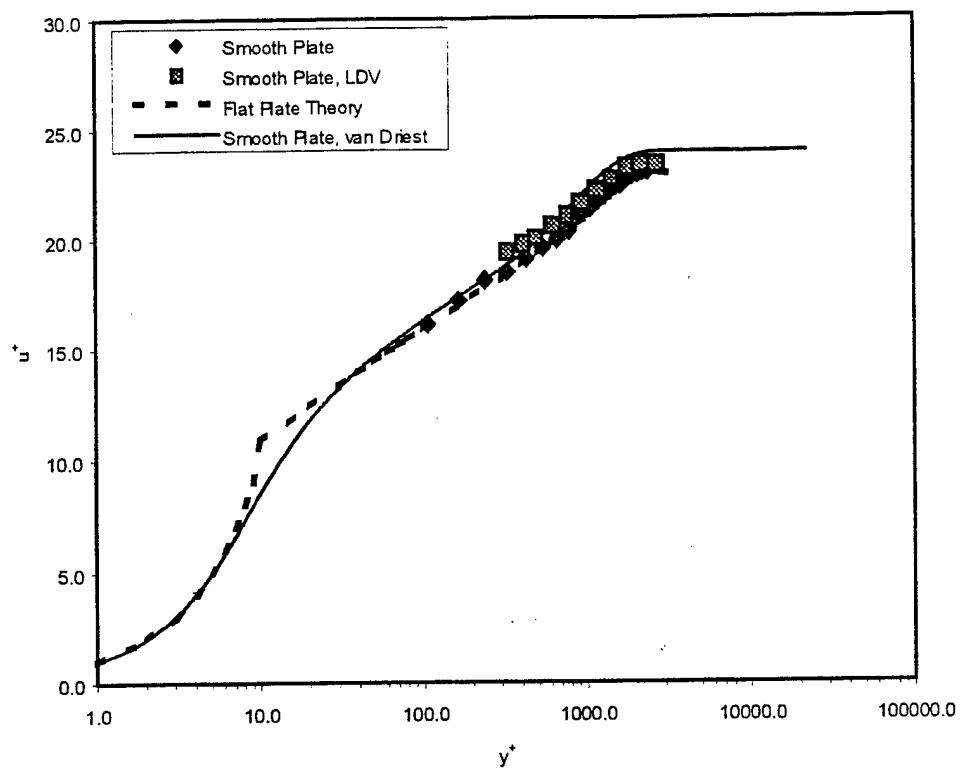
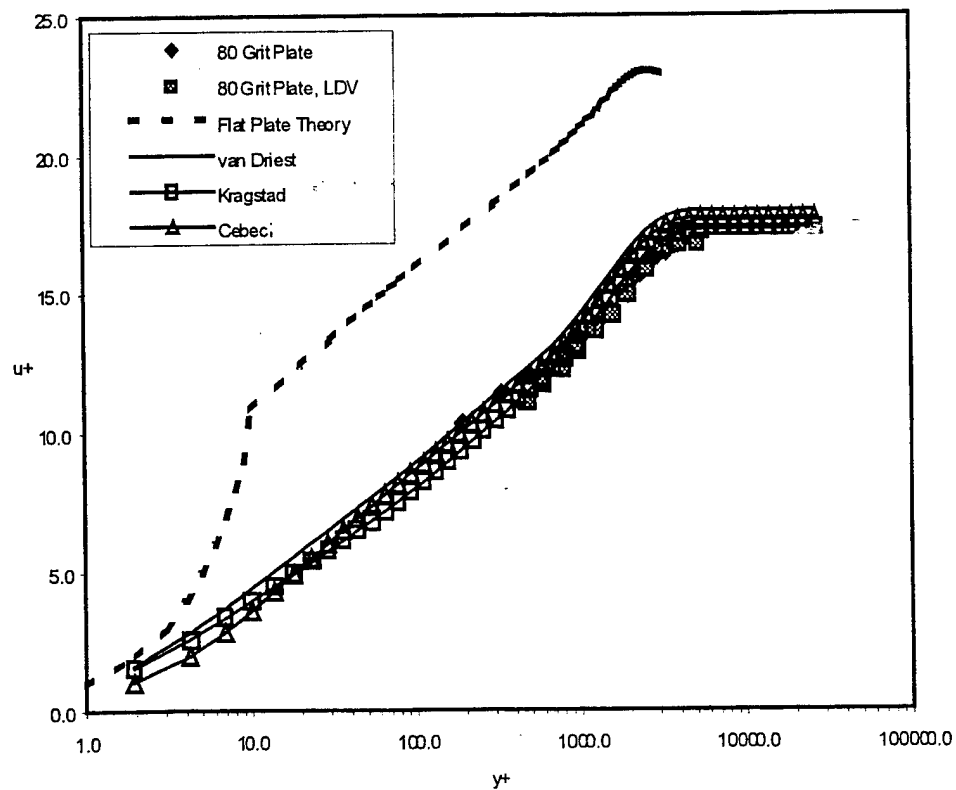


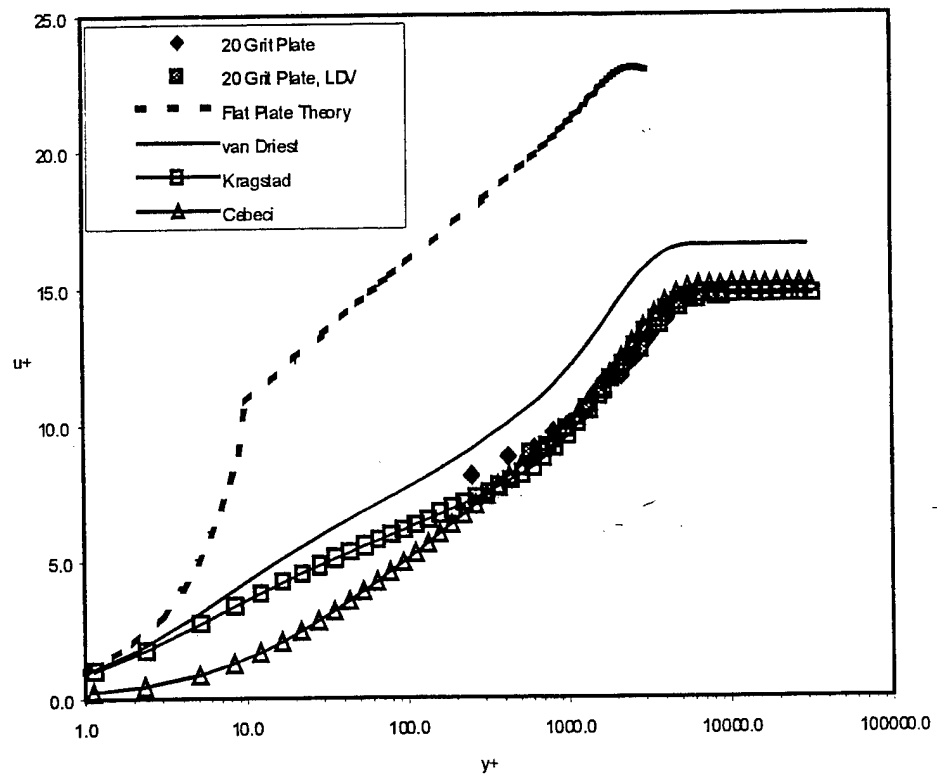
Fig. 31 Defect Law plot, with comparison to supersonic data.



(a) Smooth Plate

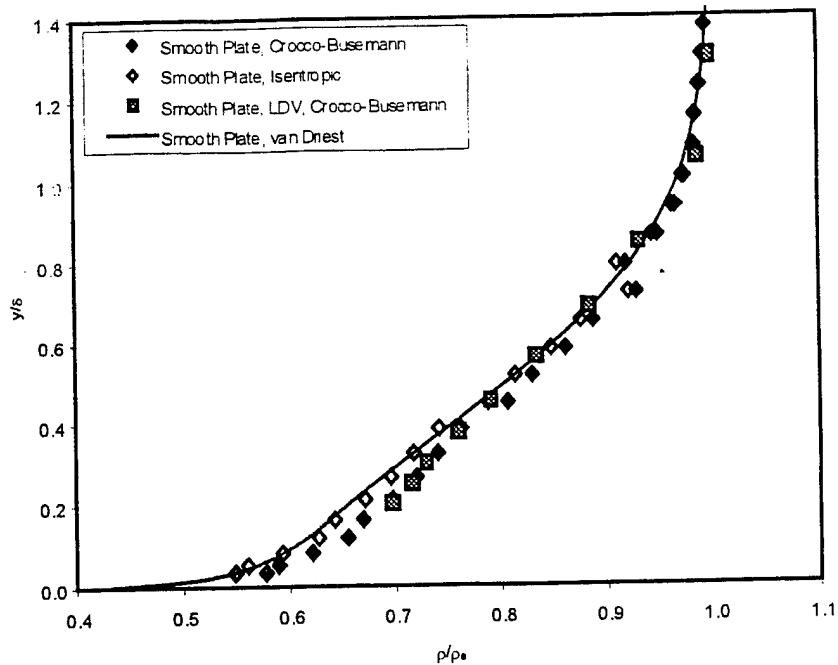


(b) 80 Grit Plate

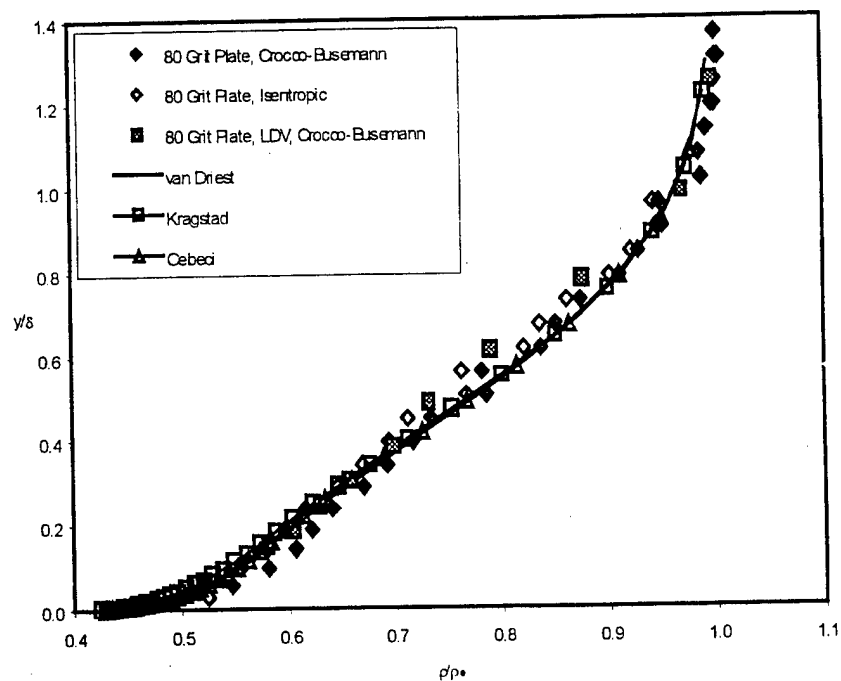


(c) 20 Grit Plate

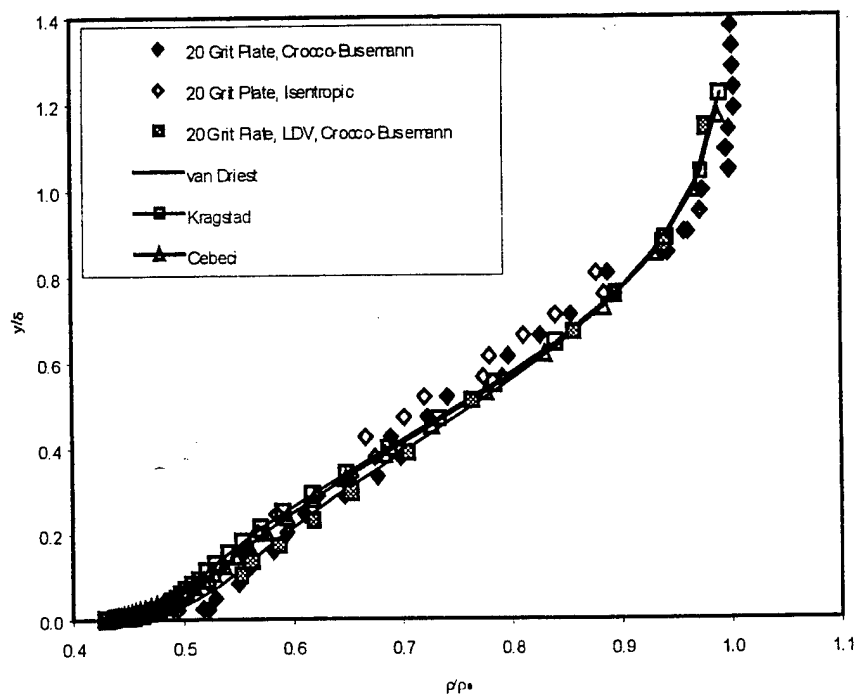
Fig. 32 Representative Law of the Wall plots, with comparison to supersonic data.



(a) Smooth Plate

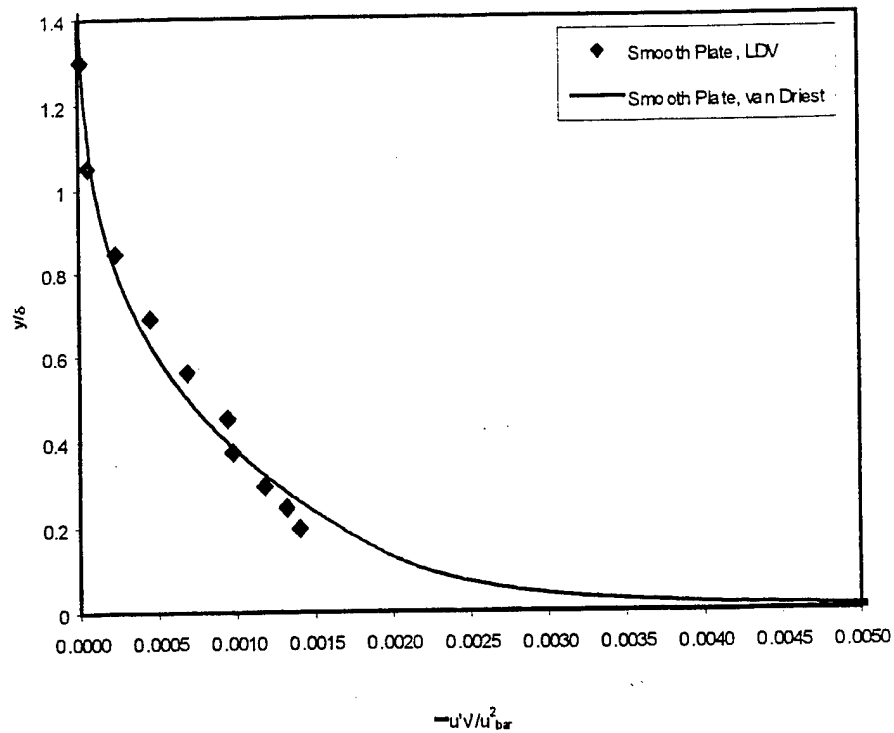


(b) 80 Grit Plate

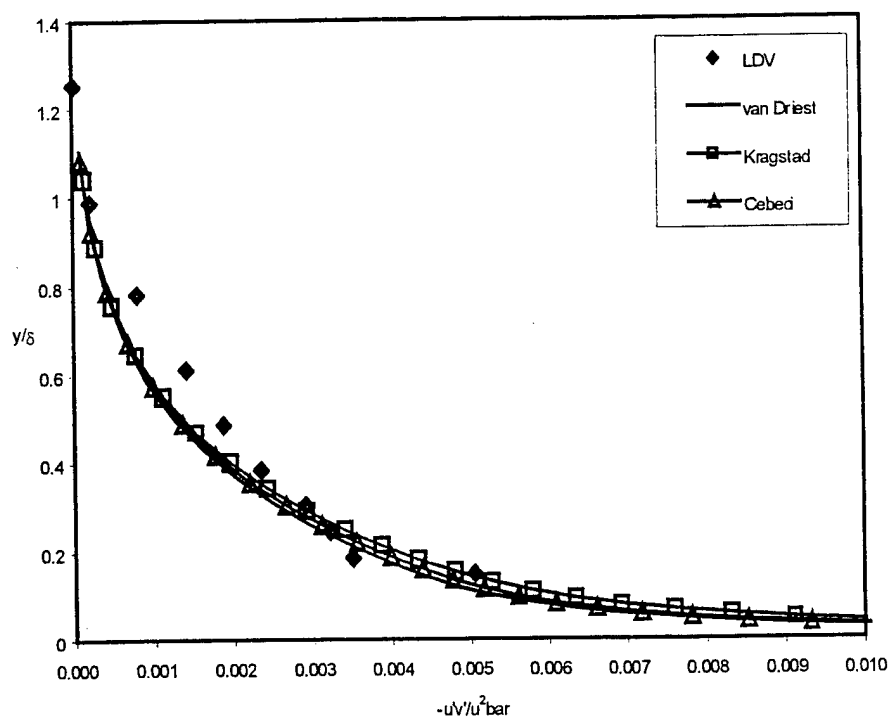


(c) 20 Grit Plate

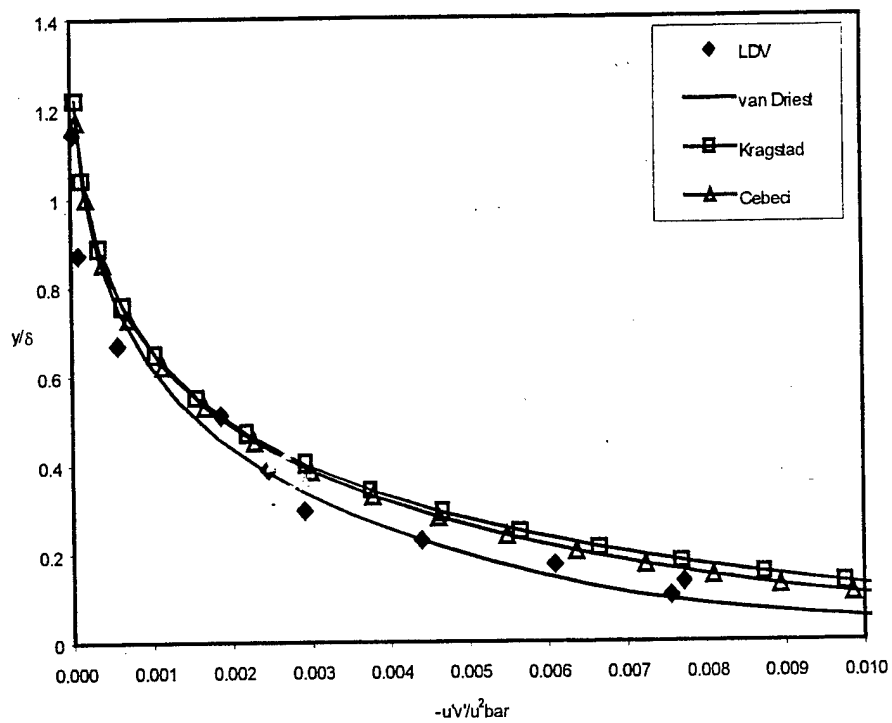
Fig. 33 Representative density plots, with comparison to supersonic data.



(a) Smooth Plate



(b) 80 Grit Plate



(c) 20 Grit Plate

Fig. 34 Representative turbulent shear stress plots, with comparison to experimental data.